POLITECNICO DI TORINO

Department of CONTROL AND COMPUTER ENGINEERING (DAUIN)

Master's Degree in Mechatronic Engineering

2019/2020

Final Thesis Project:

Combination of Infrared Thermography and Structure from Motion for detecting heat-related building's defects.

A case study and an algorithm for automated anomalies detection

Friday, October 23, 2020

Supervisors:

Prof. Filiberto Chiabrando

Prof. Marcello Chiaberge

Prof. Alessandro Sabato

Candidate:

Marco Puliti

Acknowledgements

Abstract

Structural health monitoring is a field of study that embeds several scientific areas that are combined to properly inspect structures and evaluate their integrity. In this scenario, nondestructive testing (NDT) has become an efficient and reliable inspection tool able to detect flaws and anomalies, as well as material properties. Its nature of non-harassing the object under analysis, led it to be used in a broad variety of applications. At the same time, developments in computer vision made possible to reconstruct three-dimensional models of structures starting from a suitable set of images. The aim of this research is to present a novel inspection technique that exploits both nondestructive testing and computer vision for detecting heat-related defects in structures and infrastructures. In practice, the related work concerns the combination of infrared thermography (IRT) and structure from motion (SfM) in order to detect flaws and anomalies in a laboratory-scaled structure. IRT is a well-known nondestructive technique used to highlight and detect regions within the structure with different thermal properties by measuring electromagnetic radiations in the infrared spectrum, whereas structure from motion is a photogrammetric technique that allows to reconstruct 3D models starting from a suitable set of images.

Not much work has been done towards this direction, therefore the aim of the study is to first, validate the theoretical reasonings of the presented technique, and then evaluate the obtainable accuracy of the results. For what concerns the experimental part, two different infrared thermography tests were performed; first using a hand-held thermal imager, then using an unmanned aerial vehicle (UAV) platform, embedding a dual-spectrum camera. The novelty introduced by the technique is the direct usage of thermal images to reconstruct three-dimensional digital models, so that the output is a 3D thermal map that can be interrogated for remote inspections. In both cases, the set of images acquired are suitably post-processed and adjusted in a way that the reconstruction is as accurate as possible. To this end, it is possible to perform quantitative and qualitative analysis of possible damages and anomalies remotely, exploiting the reconstruction rather than the actual structure.

In parallel with the aforementioned work, a computer vision algorithm for automatic damage detection was developed. First, temperature values are mapped in intensity pixels' values of each image, then a cascade of image processing techniques are exploited to automatically detect heat-related defects starting from thermal images. The aim is to identify the contours of damaged areas and separate them from sound parts of the image. Then, the detected contours are overlapped to the corresponding visible image, providing a straightforward result of the detection. The algorithm was tested both in a controlled environment application and in a real-world scenario, obtaining quite accurate results in both cases.

List of contents

Chapter I 14
1 General Introduction 14
Chapter II 18
2 Background 18
2.1 Defect's characterization in buildings 18
2.1.1 Moisture defects 21
2.1.2 Cracking 22
2.2 Nondestructive Testing 24
2.2.1 Sonic and Ultrasonic Testing 28
2.2.2 Visual Inspection 32
2.2.4 Acoustic Emission Testing (AET) 32
2.2.5 Electromagnetic Testing (ET) 34
2.2.6 Laser Based Testing 38
2.2.7 Ground Penetrating Radar (GPR) 43
2.2.8 Infrared radiation testing 44
2.3 UAV Photogrammetry 54
2.4 Computer Vision & Structure from Motion 61
Chapter III 80
3. Methodology 80
3.1 Case study for experimental testing 80
3.2 Equipment and NDT technique 82
3.3 Algorithm for automated damage detection 86
Chapter IV 92
4. Results 92
4.1 Experimental results using hand-held thermal imager 92
4.2 Experimental results using UAV platform and thermal imager 101
4.3 Automatic damage detection of defected areas 107
Chapter V 113
5. Conclusions 113
References 116

List of tables

Table 2.1 Different building's components lifetime 18
Table 2.2 Classification of visible crack damage 22
Table 2.3 Contact & Non-contact NDT methods 27
Table 2.4 NDT methods 28
Table 2.5 Heat-providing possible sources 52
Table 2.6 Image coverage 58
Table 3.1 Quadcopter technical specifications 84
Table 3.2 Algorithm pseudo-code 91
Table 4.1 NW reconstruction's parameters 95
Table 4.2 SW reconstruction's parameters 97
Table 4.3 Comparison between physical and measured dimensions of defects 99
Table 4.4 SW reconstruction's relevant parameters 104
Table 4.5 Comparison between measured and physical defect's dimensions 105
Table 4.6 Visible reconstruction's relevant parameters 106

List of Figures

Figure 1.1 Qualitative heat assessment 14
Figure 2.1 Damp-related defects 21
Figure 2.2 Different types of cracks depending on direction of propagation 23
Figure 2.3 Trend of real and ideal PoD curves 24
Figure 2.4 PoD statistical estimation for signal response data 26
Figure 2.5 Ultrasonic testing schematic 29
Figure 2.6 Transmission modes: (a) direct; (b) semidirect; (c) indirect 29
Figure 2.7 Velocity distribution in sonic tomography testing 30
Figure 2.8 Impact-echo testing 31
Figure 2.9 Frequency response functions obtained with an impact-echo test 31
Figure 2.10 Schematic of AE testing and basic instrumentation 33
Figure 2.11 Waveform time signal of an AE testing 33
Figure 2.12 Magnetic yoke for magnetic particle testing 34
Figure 2.13 Principle of operation of magnetic field leakage testing 35
Figure 2.14 Magnetic particle testing using fluorescent particles 35
Figure 2.15 Principle of operation of eddy current testing 36
Figure 2.16 Eddy current testing of pipelines 36
Figure 2.17 Principle of operation of remote field testing 37
Figure 2.18 Schematic of magnetic flux leakage testing 37
Figure 2.19 Constructive and destructive interference 38
Figure 2.20 Fringes patterns 38
Figure 2.21 Schematic of laser-based test 39
Figure 2.22 Shearographic test schematic 40
Figure 2.23 Shearogram of a metal element 40
Figure 2.24 Holographic testing results 41
Figure 2.25 Electronic Speckle Pattern Interferometry 41
Figure 2.26 Schematic of an interferometric profilometer 42
Figure 2.27 Profilometry test 42
Figure 2.28 Basic configuration of a Ground Penetrating Radar 43
Figure 2.29 Reflected radio waves spectrum 43
Figure 2.30 Electromagnetic radiation spectrum 44
Figure 2.31 Thermophysical model of a thermal sensor 47
Figure 2.32 Thermocouple schematic 48
Figure 2.33 Bolometer schematic 49
Figure 2.34 Structure of a microbolometer 49
Figure 2.35 Time and frequency domain results of active thermography 51
Figure 2.36 Pulse thermography on an aluminum body with cavities at various depths 53
Figure 2.37 Lock-in thermography testing 53
Figure 2.38 Example of photogrammetric survey 54
Figure 2.39 Example of camera model. Red ray representing collinearity model 55
Figure 2.40 Difference between image space and object space 56
Figure 2.41 Flight path planning 59

Figure 2.42 Common optical illusions 61
Figure 2.43 3D-2D transformations 61
Figure 2.44 Projection techniques 62
Figure 2.45 3D scene image plane transformation 63
Figure 2.46 Different types of lens distortions 64
Figure 2.47 Process of image formation 64
Figure 2.48 Thin lens model 64
Figure 2.49 Image formation pipeline in a digital camera 65
Figure 2.50 Matting example where the image in the center is used to facilitate the algorithm 66
Figure 2.51 Matting and compositing result 66
Figure 2.52 Histogram equalization 67
Figure 2.53 Different padding modes 68
Figure 2.54 Laplacian of Gaussian filter application 69
Figure 2.55 Sobel operator 69
Figure 2.56 Median filter application 70
Figure 2.57 Different of Gaussian functions in different octaves 71
Figure 2.58 Stages of keypoints selection 72
Figure 2.59 Image description characterization 73
Figure 2.60 Canny method application 74
Figure 2.61 Triangulation schematic 75
Figure 2.62 Epipolar constraints 76
Figure 2.63 Simplified workflow of Structure from Motion 77
Figure 3.1 House structure used for testing 80
Figure 3.2 Fabricated defects in the case study house 81
Figure 3.3 FLIR ONE Pro thermal imager 82
Figure 3.4 Different results obtainable from FLIR ONE Pro imager 83
Figure 3.5 Photogrammetric acquisition trajectory 83
Figure 3.6 DJI MATRICE 200 V2 with ZENMUSE XT2 imager 84
Figure 3.7 IRT testing 85
Figure 3.8 Graphical process of temperature values extraction 87
Figure 3.9 LIW operator 87
Figure 3.10 Intermediate result after Otsu's thresholding method 89
Figure 3.11 Canny method result 90
Figure 4.1 Example of MSX images 92
Figure 4.2 Cropped MSX images 93
Figure 4.3 Estimated cameras' locations and 3D point reconstructions 94
Figure 4.4 3D point reconstruction 94
Figure 4.5 Difference between tie points and 3D points 95
Figure 4.6 3D points cloud generation 96
Figure 4.7 Three-dimensional model reconstruction 96
Figure 4.8 3D model triangular meshes 96
Figure 4.9 3D points cloud generation 97
Figure 4.10 Three-dimensional model reconstruction 98
Figure 4.11 Scaling constraint application 99
Figure 4.12 Estimated camera's locations 100
Figure 4.13 3D points cloud in the visible spectrum 100

Figure 4.14 Three-dimensional reconstruction in the visible spectrum 101
Figure 4.15 Estimated camera's locations 102
Figure 4.16 3D points cloud 102
Figure 4.17 3D reconstruction 103
Figure 4.18 Digital reconstruction using a different color's palette 103
Figure 4.19 3D points cloud 104
Figure 4.20 Triangular meshes 104
Figure 4.21 Digital 3D reconstruction 105
Figure 4.22 Estimated camera's locations and links between matched images 106
Figure 4.23 3D points cloud 107
Figure 4.24 Digital three-dimensional reconstruction 107
Figure 4.25 Temperature results 108
Figure 4.26 Outcome after grey-scaling temperature values 108
Figure 4.27 Examples of LIW operator applications 109
Figure 4.28 Examples of Otsu method applications 109
Figure 4.29 Canny method application 110
Figure 4.30 Algorithm results from thermal images of the first test 110
Figure 4.31 Algorithm results from thermal images of the second test 110
Figure 4.32 Algorithm results from thermal images of a real bridge 111

Part I

First Part

Chapter I

1 General Introduction

According to the Energy Information Administration (EIA), energy consumed in the building's sector in the United States (U.S.) accounts for 20.1% of the total delivered energy consumed worldwide [1] and between 40-48% of the U.S. CO2 emissions [2]. On the other hand, constructions in Europe accounts for 21% of the total energy consumed [1] and they are characterized by an average annual specific consumption of 180 kWh/m^2, according to a survey of the European commission [3]. Therefore, advancing novel techniques for increasing energy efficiency in buildings and assessing their energy resilience is fundamental to preserve structure's reliability. Design, and material standards are continuously evolving to make buildings construction more eco-friendly [4], [5]. For instance, Schuetze et al. illustrate a case study in South Korea about a zero-emission building (ZEB) project as a milestone in new active design measures, achieving a 94% ZEB's degree [6]. Zanni et al. present a case study of heating plant retrofitting in a heritage public school [7], whereas Yang et al. illustrates an adaptive model to understand how human comfort and perception affect energy consumption in buildings [8].

While these examples target newly constructed buildings, aging defects drastically reduce the overall energy performance of already existing constructions; therefore, accurate structural and energetic assessments are required to improve the efficiency of those systems. Heat loss can be attributed to building defects such as draughts through doors and windows, water and moisture infiltrations, and poor walls insulation. As summarized in Figure 1, the main sources of heat losses in residential buildings are walls and roofs accounting respectively for 35% and 25% of total heat loss [9].

Figure 1.1. Qualitative heat assessment

An accurate analysis of the envelope is necessary to proper quantify the presence of defects in buildings that can lead to reduced energy performance. In fact, a periodical assessment of the structure prevents the growth and spread of flaws that might lead to more efficient buildings where all the possible sources of energy loss are contained. In general, a proper inspection of the construction allows to prevent severe damages in the future, guaranteeing a proper maintenance and lowering possible downtimes coming from failures.

According to Lojda, different parts of a construction have different estimate lifetimes [i.e., roof-coverings (40-80 years), windows and doors (50-80 years), heating system (20-50 years)] [10]. Thus, defects are likely related to malfunctioning or failure in those components whose life cycle is shorter than others. In fact, those parts are more stressed and exposed to wear and tear than others. Therefore, structural monitoring can guarantee adequate health assessment of buildings in those parts that are more likely to fail. Apart from poor maintenance, there are many other factors that contribute to heat loss such as climatic condition, building location, design process, type of building, material quality, soil impact [11].

The combination of structural flaws and environment factors can lead to different types of defects such as cracks, peeling paint, rising dampness, materials decay, insect or fungi attacks, roof defect, joints erosion and unstable foundation [12], [13]. An important part of heat loss in buildings is due to sub-surface defects. In general, they are dangerous for the structure since they are missed in a visual inspection and, if neglected, can lead to severe problems. Therefore, developing novel methods to assess heat loss through the construction's envelope can help evaluate possible causes of waste and act to reduce energy consumption. Novel and autonomous inspection techniques that can expedite the assessment of the targeted structures are sought to reduce downtime and increase the system's energy efficiency. Defects such as those listed above often cannot be detected using visual inspection, creating a growing need for non-destructive testing (NDT) techniques that are capable of scanning large areas of the building to identify flaws presence. NDT methods have proven to be versatile methods for the characterization of defects, enhancing structural safety while decreasing the overall costs, in several engineering domains [14]–[16]. A lot of work has been done in the past years to develop nondestructive methods able to properly assess structure's conditions, exploiting different scientific areas. Gholizadeh in [17] presents the macro areas of NDT, trying to define a method to decide which is the best technique to implement depending on the purpose of the application. Among all, when it comes to heat losses and sub-surface anomalies, infrared thermography (IRT) is an effective methodology to perform an identification of them, since it enables to extract thermal maps of the object being tested, quickly detecting faulty regions characterized by different temperature compared to sound areas.

Along with nondestructive testing methodologies, photogrammetry and computer vision have become known to be reliable tools to further enhance the inspection and assessment of structures. In fact, cameras are used in several NDT techniques to have a better visualization of the results as well as post-process data obtained with testing. In the field of Structural Health Monitoring (SHM), a quite novel technique that is gaining a lot of interest is Structure from Motion (SfM). It is a photogrammetric technique relying on images' datasets to reconstruct digital models able to achieve very high accuracy. It allows to remotely inspect structures, aiding inspectors to identify both qualitative and quantitatively structural conditions. Moreover, it became important since it is possible to inspect parts of the structure that are practically inaccessible but that can be affected by structural problems. Often, SfM is combined with unmanned aerial vehicles (UAVs) platforms to perform inspections of large areas, or in harsh conditions, to guarantee reliable and accurate digital reconstructions of large infrastructures.

The research described in this thesis aims at advancing an inspection tool for monitoring the conditions of building envelopes and energy infrastructure systems over time. Optical and IR scans are used to detect early flaws and inform preventive maintenance on building envelope. Three-dimensional (3D) points cloud reconstruction will serve to build a 3D model of the targeted infrastructure and as a tool for inspecting and quantifying the targeted system's conditions remotely. The UAV-IR points cloud technique may increase the efficiency of energy systems through visual data-analytics that are easy to interpret. The proposed approach will find application for energy audits, damages quantification, energy losses assessment, and planning remediation activities on targeted systems. The combination of IR scans from an Unmanned Aerial Vehicle (UAV) platform are combined with a points cloud reconstruction technique to generate highly detailed 3D digital models and assess structural conditions as well as physical attributes of different structures. The digital reconstruction can

be also interrogated for quantitative evaluations. The objective of this work is to merge IRT and Structure from Motion (SfM) to develop 3D thermal reconstructions, starting from images taken using both a hand-held camera and an unmanned aerial platform. The 3D reconstruction is then used to detect defects in the envelope in an automatic way. So far, a lot of work has been done towards the reconstruction of models starting from visible images and then overlap the digital model with thermal images [18]–[20] to understand where heat related defects might be. Instead, not so much work has been performed to understand how to reconstruct 3D models directly starting from a set of infrared images [21].

Provided that, the work methodology proposed in this research is to directly reconstruct 3D models starting from thermal images such that the overall reconstruction is a thermal map of the building. This is a more difficult procedure since the resolution of thermal images is in general lower than that of images in the visible spectrum. So far, not much work has been published towards this direction, but the results are promising [21], [22]. The first test aimed to understand the feasibility of the technique proposed whereas the second one was focused on the detection of flaws related to heat losses both in a quantitative and qualitative way through the envelope. The case study is a laboratory-scaled building with different fabricated defects, in order to emulate a real-case scenario. The first attempt was performed by means of a hand-held camera embedding both a visible and an infrared sensor, while the second one was carried out by means of a UAV platform with a detachable imager as payload, with higher resolution than the first one. Furthermore, the possibility to work with a digital reconstruction of the building, allows the evaluation of possible anomalies directly from the model. This allows to conduct inspections in remote, further enhancing the portability of the technique.

The proposed autonomous inspection techniques using IR scanning can be used to map and assess physical attributes of buildings and energy infrastructure. 3D aerial scans can quantify energy losses, monitor damages, and track changes in the envelope of the structure to improve its efficiency and reliability. Moreover, the method proposed in this research can ensure the resiliency of the infrastructure by evaluating the status of the system [23]. Thus, new approaches for monitoring and databasing energy systems can help to decrease the risk of significant service disruptions and allow a timely response to emergencies while reducing costs [24]. The last part of the proposed work is related to an algorithm for automatic flaws detection starting from thermal images. The possibility to automize the process of detection is of key importance to avoid possible human errors and guarantee reliable results. Image processing and computer vision algorithms were used to develop a program in Python suite, allowing a full customization of the results. The specific objectives of this thesis are to: (1) advance the accuracy of points cloud reconstruction from IR images, (2) develop a mapping method using thermal sensors for heat loss inspections and autonomous perception to enhance decision-making speed and quality, (3) develop a tool to automatically detect anomalies in the building's envelope. The related work is divided in the following sections; chapter 2 concerns the state of the art in the main scientific areas involved in the developed technique, namely defects' characterization, nondestructive testing methodologies, photogrammetry and computer vision, chapter 3 relates to the methodology used to carry out experiments; chapter 4 involves the characterization of the results obtained from the tests, whereas the last chapter is dedicated to discussions about the results obtained, along with possible further steps and conclusion.

Chapter II

2 Background

The following chapter is intended to provide a general background of the main scientific areas involved in the project. The first section concerns the characterization of defects in structures and infrastructures focusing on building's damages whereas the second section aims to provide a general understanding about nondestructive evaluation techniques, highlighting infrared thermography (IRT), core of the proposed research. Then, section III provides a general overview about Photogrammetry and Computer Vision, specifically Structure from Motion (SfM) and image processing techniques.

2.1 Defect's characterization in buildings

Every structure or infrastructure is characterized by a life cycle. It is defined as the period from the idea creation up to its disposal. The usual construction phases are design, implementation, usage and disposal. During this period, they undergo several different environmental conditions and more in general external factors that can contribute to the generation and growth of defects and damages. Moreover, each individual part of a construction has a different lifetime, defined as the time in which these components perform their functions and guarantee a certain level of service. Provided that, it is likely possible to associate the presence of flaws to those components whose lifespan is shorter than other since they might deteriorate in a fast way. For instance, in the case of buildings, long-life elements could be basics, vertical bearing structures and stair construction, whereas insulation layers, floors and surface finishing of walls (i.e. plasters, tiles and paints) are in general more subjected to deterioration [10]. Therefore, structural health monitoring and maintenance are of key importance to maintain suitable working conditions in constructions. According to the British Standards Code of Practice, a defect is a deterioration of building features and services to unsatisfactory quality levels of the requirement of users. They are present regardless the age of the construction since there are many factors that can contribute to their formation. For instance, improper maintenance and wrong construction design are common factors related to possible anomalies for old and new constructions respectively. Defects can be also characterized as nonconformity of a component with a standard or specified characteristic. They may lead to a shortfall in performance that resolves into improper functioning of the structure and, in severe cases, can lead to failure. Table 2.1 summarizes the most relevant parts of a building and their lifespans.

Table 2.1 Different building's components lifetime (source: De-cree.441 / 2013 Coll., § 21)

Types of construction or equipment	Estimated life in years
Basics	150-200
Vertical constructions	80-200
Doors and windows	50-80
Plumbing constructions	30-80
Heating	20-50

By looking at different building's components in Table 2.1, it is possible to understand that the probability of encountering an anomaly is higher in those components whose life cycle is shorter than others. This is mainly because their deterioration phase starts before other components; therefore, they are often the subject of renewal and reconstruction. It is also worth to notice that long-life components' maintenance is in general high demanding in terms of expertise, time and financial resources since defects in these parts can be very dangerous for the overall structure. In both cases, an accurate analysis of the envelope is necessary to proper quantify the presence of defects that can lead to reduced performance both from the energetic and structural point of view. In fact, a periodical assessment of the structure prevents the growth and spreading of defects and damages, aiming to achieve adequate health conditions. In general, the presence of flaws in a building can lead to a variety of problems. Among all, the most relevant are structural problems, thermal problems, moisture problems and noise problems.

The main function of a building is to protect the occupants from external weather conditions. To do that, the construction must be structurally sound, so that to guarantee an intact envelope. Structural failure is the result of over-stressing the structure, that is the imposition of loads in excess of the capacity of the structural components. The ultimate stage of failure is of course collapse, most serious result of a structural problem. The main causes of structural problems are incorrect design or construction and unsuitable materials. Another possible cause of structural problems is the movement of the structure itself. In theory, a building is designed to be rigid and inflexible but in practice, a considerable amount of movements occurs. The most common cause is the change in temperature and moisture content that results in expansions and contractions. Such movements are not so serious if all the structure moves simultaneously whereas differential movements can resolve in serious problems. This occurs if the reaction to temperature and moisture change is different in structural components or materials. These types of movements are in general not so dangerous for the structure if properly considered in the design phase. Settlement and subsidence are other two significant causes of movement in buildings. The former is a natural process involving compaction of the supporting soil under the load of a building. It is always present, and it is not too dangerous, provided that it is uniform over the entire supported area of the building. On the other hand, subsidence is settlement that may result from factors other than simple compression of the supporting ground. For instance, dramatic subsidence could be caused by tunneling operation underneath the building as well as erosion due to water movement.

For what concerns thermal problems, it is possible to focus the attention in the envelope of the building. In fact, proper materials guarantee thermal insulation of the building, that is providing resistance to transfer of heat from inside and vice versa. The presence of draughts or gaps in the envelope reduces the overall insulation of the envelope, as well as lack or reduction in the insulation materials. The parameter to quantify thermal problems and heat losses is the thermal transmittance, that is the rate of heat's transfer thorough matter. Other important parameters to quantify heat problems are the thermal conductivity, ability of a material to conduct heat and its reciprocal, the thermal resistance, that is the ability of a material to resist the heat flow. Another common cause of thermal problems is ventilation heat loss, that is related to the energy waste in heating, ventilation and air conditioning (HVAC) systems. This can be quantified by means of a unit called air change per hour (ach), that is a measure of the air volume added to or removed from a space divided by the volume of the space.

The third category of problems in common buildings is related to moisture presence. Although a significant moisture content is normal in all porous structural materials, an excessive content can cause several problems such as condensation, water accumulation, dampness, resulting in a saturation of the material with respect to moisture. Fluctuations in moisture content can have a considerable effect upon the density of the material. This can result in dimensional changes that cause structural movements. An example of this behavior can be seen in wood components where the presence of excessive moisture can cause changes in shape and size. Moisture presence is strongly related to environmental conditions, in fact air carries a certain percentage of moisture depending on weather conditions. To measure the temperature and relative humidity content, various instruments are available. Hygrometers measure relative humidity directly, often using the change in length of a

strip of paper, whereas temperature methods can be used to determine the "dry" and "wet" temperature. The latter is in general lower than the former since water evaporation from a wet material causes cooling. These two temperatures can be used to measure the relative humidity in the air and can be considered the same when relative humidity is 100%, thus the material or ambient is saturated. Temperature and humidity are parameters indicating the conditions of the air inside the building, so that the HVAC system can work properly to maintain suitable comfort's conditions, avoiding thermal problems.

The last category of building's problems concerns those that are related to acoustic noise. Noise problems are sounds originating from different sources, both elsewhere the accommodation or within it, which interfere and cause irritation. Sound involves atmospheric pressure oscillations, the frequency of the oscillations giving the pitch of the sound and the amplitude giving the intensity of loudness. A common indicator of the quality of a room is the interference, phenomenon in which two or more acoustic waves superimpose to generate a wave with greater, lower or equal intensity value with respect of the original ones. In general, the degree of interference is expressed by the reverberation time, defined as the time needed for the complete decay of an acoustic wave and its reflections. In general, the lower this time, the better the conditions of a room. Reverberation depends directly on the volume of the unit tested and indirectly on the sound absorption of the surfaces or the area of each surface multiplied by its absorption coefficient. Therefore, an accurate analysis of the envelope materials is needed to guarantee noise reduction and insulation as much as possible.

Before characterizing different types of defects in the building's sector, it is worth to investigate possible factors and sources that contribute to worsen construction's conditions. Many studies have been done to understand possible factors behind the presence of defects in buildings. Talib et al in [25] reported that the main factors affecting building's defects are lack of building's maintenance, overlooked site condition, defective material, poor quality control, lack of training, ageing of building, environmental conditions and moisture problems. Furthermore, Ahzahar et al in [26] specify that building's defects and failure are influenced by climate conditions, building location, construction's material, type of building and functional changes, design's fault and lack of supervision. An interesting work was conducted by Yacob et al in [11], trying to rank all the possible factors causing defects' presence. A total of 300 school buildings were analyzed in order to identify the most important factors causing defects according to an index called relative importance index (RII). The study identified that the relevant factors contributing to building's defects are lack of supervision, maintenance and poor-quality materials.

The first important division in the characterization of defects is in structural and non-structural. The first category is the most important one since it's related to structural element whose collapse would lead to a failure of the whole structure. In fact, structural elements such as earth retaining walls or foundation are responsible for bearing most of the load of the structure therefore, anomalies in these elements must be periodically monitored to avoid serious problems. They are mainly cracking that can be caused by a variety of factors. Among all, the relevant ones are unsuitable soil, poor constructions techniques, unsuitable damp protection and over-stressing. In general, cracks decrease the ability of a structural element to resist the stress that is carrying, causing serious problems if not treated. On the other hand, non-structural defects are mainly related to part of the structure that are not fundamental for the overall functioning of the construction. For instance, all the possible problems related to plaster works or brick work fall in this category. They are in general less dangerous than the structural ones since it is rarely possible that they lead to structural failure.

Building's defects can also be categorized into patent and latent defects. The former category is characterized by visible, identifiable defects, such as wall's cracks, sagging gutters or missing tiles. In most of the cases they don't require an expert inspection to be identified whereas latent defects are hidden and cannot be detected by someone who does not have a critical eye. For instance, rising damp, rusted internal pipes and faulty heating or electric systems fall in this category. The following sections try to describe the most relevant defects and damages in the building's sectors.

2.1.1 Moisture defects

Moisture defects can affect both structural and nonstructural components of buildings. In general, they are related to an excessive moisture and water content in the structure and can lead to a variety of damages. For what concerns walls, floors and ceilings, dampness is a very dangerous problem. It can be caused by a variety of factors and the result is a water infiltration that leads to a worsening of structural properties. It can also lead to very different problems such as rotting, corrosion of iron or steel materials, leaking, condensation, decaying and breaking up of mortar joints. This category of defects can be divided in two main groups, rising and penetrating dampness. The former is generated by ground water or floodwater when damp proof materials are not or wrongly placed at the base of the buildings. It spreads from ground level by means of capillaries action, spreading into the component involved. Instead, penetrating dampness is associated to moisture penetration through the lateral facades of a building, usually related to leaks, pipework damage, blocked drains or leaky gutters. Dampness in buildings can be generated by a variety of causes such as:

- **construction process:** mixing water to form mixtures can lead to dampness problems if the proportions are not properly respected. The result is a worsening of the component's properties due to retaining moisture that shows up;

- **weather precipitations:** rain and snow for instance can be driven by the wind and penetrate joints causing water retaining. This creates serious problems in the structural integrity of the component. Also, gutter overflow can be the cause of dampness in walls;

- **condensation:** humidity of the air can lead to water content absorption of walls and surfaces, resulting in dampness problems. This phenomenon is common in high humid environments such as tropical areas;

- **leaks:** they can come from different systems such as plumbing, ventilation or heating system. If not treated, those leaks can spread and generate serious problems;

Figure 2.1 shows some examples of damp problems in common building's parts.

Figure 2.1 Damp-related defects

Another relevant defect coming from moisture problems is peeling paint. It usually occurs in correspondence of building's facades, usually plastered columns and walls, that are exposed to weather conditions and dampness. In general, this defect is the result of moisture penetration and the result of poor surface preparation. For instance, it can happen when plastered or skimmed walls or ceilings are not given enough time to dry before start painting them. On the other hand, also a quick drying after painting, for instance by heating the painted surface, can cause peeling.

Mold growth is another type of defect falling in the category of moisture problems. It can be found either indoor or outdoor and can cause serious problems to human health if not properly treated. Mold is a type of fungi and there are many different categories that can affect building's parts. Mold becomes a problem when combined with water damages or high humidity environments. In fact, the reproduction is based on the generation of tiny spores that are released in the air and can settle in surfaces. When they land in damp spots, they can easily begin spreading, ruining whatever they are growing on in order to survive. This results in a gradual destruction of the material involved causing building's problems. For further analysis on building's problems related to moisture, interesting readers can refer to the work of Othman et al in [12], where a complete description is given and also a case study about hospital buildings is provided.

2.1.2 Cracking

Cracking is one the most important problems in buildings. According to the ISO 6157, a crack is defined as clean fracture passing through or across the grain boundaries and may follow inclusions of foreign elements. The most relevant causes of cracks are ground movement caused for instance by clay shrinkage or land slip; foundation failure due to decay of materials; decay of building fabric; faulty or damaged drains or tree roots growth. They can basically be characterized by their dimensions and direction of propagation. Table 2.2 classify cracks based on their dimensions.

Table 2.2 Classification of visible crack damage (source: Defect in Building, 2003)

Category of damage	Degree of damage	Description	Approximate crack width [mm]
0	Negligible	Hairline cracks, no action required.	Up to 0.1
1	Very slight	Fine cracks, easily treatable.	Up to 1
2	Slight	Crack easily filled, non-necessarily visible externally.	Up to 5
3	Moderate	Cracks which require some opening.	5 to 15
4	Severe	Extensive damage which requires replacing sections.	15 to 25
5	Very severe	Structural damage which requires a major repair, extraordinary maintenance.	>25

As it is possible to notice, the dimension of the crack is a key parameter for maintenance. If not properly treated, cracks can lead to severe damages and in some cases to structural failure. The other characterization is related to the direction. In fact, it is possible to list three different types of cracks depending on the direction in which they propagate.

- **horizontal cracks:** may indicate that an element such as a wall is failing and this may present a safety concern, they require immediate attention;

- **vertical cracks:** may indicate that structural components such as bricks or blocks have failed due to significant stress in the building's structure; instead, if the crack started near a junction, it indicates that the cause is likely due to foundation settlement after construction;

- **stair steps cracks:** the continuous pattern usually follows the brick line or the stone block and can be seen in unfinished basements due to the result of soil settling beneath the center of the wall.

To summarize, different factors are related to cracks' formation. In general, they are the most common defect in buildings, therefore an accurate analysis is required to avoid severe problems. A detailed investigation must be carried out to identify the causes which must be resolved or rectified before the cracks are repaired. Figure 2.1 shows examples of different types of cracks.

Figure 2.2 Different types of cracks depending on direction of propagation

Other possible defects in buildings can be insect or termite attacks that are in general related to timber structures or components and can easily represent a threat for the entire structure if not taken seriously. Another one is timber decay, possibly due to water infiltration, rooting or just aging. Other possible defects are defective plastering, or roof defects, unstable foundation, hazardous substances such as asbestos, poor insulation or faulty systems such as fittings, plumbing, drainage, heating systems. For a more accurate analysis of building defects and causes related to them, interested readers can refer to the book [27] that carefully explains all the relevant problems in the building sector.

2.2 Nondestructive Testing

Few decades ago, the assessment of the properties of a material was performed by means of standardized tests on prepared test pieces. Although, a lot of information can be extracted by these types of methods, they often carry the destruction of the material as drawback. In addition, the characterization of specimen' properties does not necessarily give a clear understanding of the complex-shaped component that the test piece is trying to simulate. The need for more reliable and satisfactory data, led nondestructive testing to expand towards many different areas.

Nondestructive testing (NDT) concerns a wide group of techniques used in the engineering and scientific areas to evaluate properties of systems, materials and components and identify possible anomalies. During the last decades, these types of methods gained a lot of interest simply because their nature is to avoid any damage at the structure involved. In fact, tests are most of the time contact less, therefore the structure is not affected by the test being carried out. This is an important step forward in the measurements and testing fields since it is possible to extrapolate characteristics and specifications of a material or component without affecting the structure involved. NDT also allows to save both financial and time resources, guaranteeing an adequate characterization and inspection of a structure, improving both the quality control and maintenance phases of a product. The main objectives basically are to extrapolate properties of materials, as well as detect flaws and anomalies in the structure under analysis. A wide variety of NDT techniques play major roles in testing properties of composite materials [17]. The applications of such methods may include aerospace [28], military and defense [29], manufacturing [30], concrete and masonry structures [15] and nuclear industry [31].

In the field of structural health monitoring, another important part of NDT study concerns the degree of reliability of the method, i.e. understanding what is the smallest detectable discontinuity or the larger non detectable flaw. Nowadays, the most used method to determine the sensitivity of an NDT technique is through the characterization of probability of detection (PoD) curves. A PoD curve estimates the ability of detection regarding a given threshold discontinuity size. Ideally speaking, discontinuities smaller than the estimated critical size would be labelled with 0, meaning zero probability of detection, whereas every defect above this threshold is given 100% probability of detection. This is an ideal behavior since in practice, it is not possible to have such sharp change in the detection. The real PoD is basically an approximation of the ideal one, considering the probability of having false positives or false negatives, that can easily corrupt all the results of the detection. In general, those curves representing the actual trend of the probability of detection are constructed empirically. Figure 2.3 clarify the difference between real and ideal PoD.

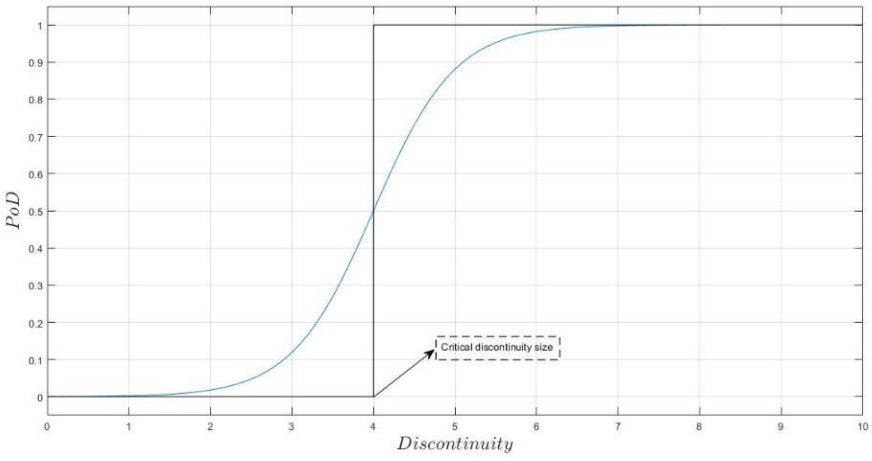

Figure 2.3 Trend of real (blue) and ideal (black) PoD curves

To assess the quality of the measurement and the test performed, a commonly used method is the Round Robin Testing (RRT) where independent inspectors perform a nondestructive examination of the same structure, to identify the same defects, usually fabricated to allow a better outcome of the results. The purposes of this test are to determine the reproducibility of the method, verify a new method and provide basis for possible certificates about the material or component being tested. For each inspection, an estimated PoD curve is drawn, and different curves are compared to understand the reliability of the test. A model for such purpose was proposed in the 1^{ST} European-American Workshop of reliability [32], recognizing three main functions connected to the reliability of a nondestructive technique: human factor, intrinsic capacity of the system and characteristics of specific applications. To quantify the reliability of a technique when applied to a specific defect, the function to consider is:

$$Re = f(IC) - g(PA) - h(HF) \tag{2.1}$$

where, R_e is the total reliability of the system, $f(IC)$ is function of the intrinsic capacity of the NDT system, $g(PA)$ is function of the parameters applied (i.e. surface finishing, access, etc.) and $h(HF)$ is function of the human factor (i.e. experience, skills, training, etc.). In this scenario, automatic inspection will provide higher probability of detection because part of these factors is not considered as for instance the human factors. Moreover, to guarantee an adequate result, a large set of data is necessary, meaning that the test must be repeated several times, trying to guarantee the same testing conditions.

Sometimes, it is not possible to perform the same test several times since it is in general difficult to fabricate a high number of test pieces with identical fabricated defects. In this scenario, there are statistical models to estimate the PoD curves, depending on the type of test been carried out. If the purpose is just to determine if a flaw is detected or not, it is possible to talk about "*hit/miss*" data, that are discrete data; whereas, if more information are needed, the reference is to "â" data, meaning that the signal is perceived as proportional to the flaw size, indicated with the parameter "a". The two categories of data require a different probabilistic model to produce the PoD function. The details about the theoretical analysis are beyond the aim of this section, more information can be found in [33]. Among different statistical distributions, the most acceptable for hit/miss data is the *log-logistic distribution* that can be written as:

$$PoD(a) = \frac{e^{\frac{\pi}{\sqrt{3}}\left(\frac{\ln a - \mu}{\sigma}\right)}}{1 + e^{\frac{\pi}{\sqrt{3}}\left(\frac{\ln a - \mu}{\sigma}\right)}}, \tag{2.2}$$

where a is the defect dimension and, μ and σ are the average and the standard deviation of the set of data, respectively. Equation 2.2 can be rewritten as follows:

$$PoD(a) = \frac{e^{(\alpha + \beta \ln a)}}{1 + e^{(\alpha + \beta \ln a)}} \tag{2.3}$$

By means of some mathematical manipulation, it is possible to say that:

$$\ln\left(\frac{PoD(a)}{1 - PoD(a)}\right) = \alpha + \beta \ln a \tag{2.4}$$

where $\mu = -\frac{\alpha}{\beta}$ and $\sigma = \frac{\pi}{\beta\sqrt{3}}$. Thus, it has been demonstrated that the logarithm of the probability of detection is proportional to the logarithm of the defect size, indicated with the parameter a.

On the other hand, for signal response data, much more information is carried by the signal than in *hit/miss* data. In fact, the PoD function is derived from the correlation of "â" and "a" data. In the study of Berens in [34], it has been observed that there is an approximate linear relationship between the logarithms of the two data. This is usually expressed as:

$$\ln(\hat{a}) = \alpha_1 + \beta_1 \ln a + \gamma \tag{2.5}$$

where γ is an error term and it is normally distributed with zero norm and constant standard deviation. Equation 2.5 represents the normal distribution of $\ln(\hat{a})$ centered at $\mu(a)$ and deviation σ_γ^2, where

$$\mu(a) = \alpha_1 + \beta_1 \ln a \tag{2.6}$$

The $PoD(a)$ function for the NDT response signal ($\ln(\hat{a})$) can be represented as follows:

$$PoD(a) = Probability(\ln(\hat{a}) > \ln(\hat{a}_{th})) \tag{2.7}$$

where $\ln(\hat{a}_{th})$ is the limit of defect's evaluation. In other words, it is the area included between the probability density function of $\ln(\hat{a})$ and above the flaw threshold $\ln(\hat{a}_{th})$. Figure 2.4 graphically explains the concept.

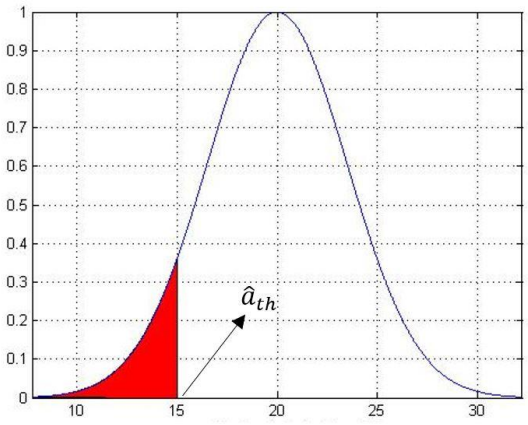

Figure 2.4. PoD statistical estimation for signal response data

Other statistical methods can be used for this type of analysis, but it is beyond the scope of this section to investigate them. For further details about the two presented methods of PoD curves estimation or for different statistical methods, interesting readers can refer to [35] which provides a very accurate analysis about PoD curves and their applications.

The first important characterization of NDT methods is between contact and non-contact techniques. In fact, sometimes the need to have a surface of contact between component and instrumentation is of vital information to guarantee reliable results in the inspection. On the other hand, there are tests in which the medium between instrument and component doesn't really matter and the contact between them is not relevant. Classic NDT methods such as traditional ultrasonic testing, eddy current testing, magnetic testing, electromagnetic

testing, and penetrant testing are contact tests whereas radiographic testing, thermography, shearography and visual inspection do not require a physical contact between sensor and tested structure. In general, all the optical methods can be considered contact-less nondestructive tests and do not require any medium between material and sensors. Therefore, air is the preferable one. Table 2.3 shows the most relevant NDT techniques, dividing them depending on the contact nature of the test.

Table 2.3 Contact & Non-Contact NDT Methods

Contact Methods	**Non-Contact Methods**
Traditional Ultrasonic Testing	Through transmission Ultrasonic
Eddy current testing	Radiography testing
Magnetic Testing	Thermography
Electromagnetic Testing	Infrared Testing
Penetrating testing	Holography
Liquid penetrant Testing	Visual Inspection

NDT methods have become an established set of tests to evaluate structural health conditions. In fact, they can be either used to evaluate materials properties that before where characterized with destructive tests such as tensile tests or hardening tests, and at the same time they are able to assess the condition of the structure under analysis, identifying both quantitatively and qualitatively possible anomalies and defects. This is of key importance when it comes to quality control, maintenance, prevent failures and quickly inspect a structure. In general, these types of tests do not guarantee an overall assessment of the structure, but they focalize in specific parts where the flaw is likely to be present. Moreover, it is worth to notice that each method is suitable for a specific investigation; hence, a proper inspection's characterization needs to be properly considered. It is often advisable to undertake a feasibility analysis on the structure to assess the suitability of the selected NDT method for the investigation of structural problems. McCann et al. in [15] broke down a sequence of steps to properly set up an inspection of a structure. The phases are listed below:

- *phase 1*: visual inspection;
- *phase 2*: analysis of loading carrying capacity;
- *phase 3*: review needed for further investigation;
- *phase 4:* "desk study", research on the origin of the structure, who designed and built it and any other possible information;
- *phase 5*: cost effectively choose the most suitable strategy for further investigation;
- *phase 6*: implement the investigation technique.

As you can notice, a proper planning of the investigation is necessary both to guarantee a satisfactory outcome in the measurements and to save time and financial resources in the inspection. In fact, a proper inspection allows to detect possible anomalies in shorter time, guaranteeing adequate health conditions of the

structure and reducing downtime in the maintenance phase. Before entering in detail about the principles of operation of different NDT methods, Table 2.4 summarizes the most relevant NDT methods along with advantages and disadvantages.

Table 2.4 NDT methods

Inspection method	Parameter measured	Advantage	Disadvantage	Cost
Visual	Surface condition	Quick; modest skills required.	Superficial	Low
Proof load test	Load carrying capacity	Definitive.	Slow and possibly dangerous	Very high
Vibration testing	Mode shapes	Gives some indirect measure of current condition.	Difficulty to quantify data	High
Impact testing	Mode shapes	Gives some indirect measure of current condition.	Difficulty to quantify data	Moderate
Ultrasonic	Wave velocity through structure	Relatively quick.	No information on major elements	Moderate
Sonics	Wave velocity	Useful information on major elements.	Requires skills to interpret data	Moderately high
Conductivity	Relative conductivity	Quick;	Limited depth penetration of 1.5 m	Low
Radar	Electromagnetic wave velocity	Quick, can give good penetration.	Require skills to understand data	Moderately high
Thermography	Infrared energy	Quick; reliable.	Poor image resolution	Moderate

Provided this general overview in NDT methods, the following sections are related to basic principles of non-destructive testing methods, describing the most common techniques used for detecting anomalies or characterizing materials in structures and infrastructures. Much interest is related to infrared thermography, used in the proposed work.

2.2.1 Sonic and Ultrasonic Testing

Sonic and Ultrasonic testing is a family of nondestructive methodologies based on the propagation of high frequency sound waves, typically between 0.5 and 50 MHz, in objects or materials, in order to detect internal flaws or to characterize material's properties. High frequency waves (HFWs) are generated by an emitter that is usually a transducer and pass through the material. By keeping track of the propagation of HFWs and possible reflections, it is possible to interpret geometric properties and inspect the material for flaws and other anomalies. Output signals are acquired by a receiver that is connected to an acquisition system or a display device, facilitating the interpretation of the results. The most relevant type of sonic or ultrasonic methods require the contact between surface and transducers. This is usually performed by means of a proper medium of transmission. In fact, ultrasonic/sonic energy is quite attenuate by air and cannot be transmitted in the same amount on every medium. Therefore, a couplant between the surface of the material and the sensor is required. Generally, in this type of testing, the most common coupling mediums are liquids such as oil, gel, water or grease to enhance

energy's transfer to the tested specimen. If the wave locates a discontinuity in its path, it creates a reflective wave from the flaw's surface, going back to the surface of emission; then it is turned into an electrical signal and it is displayed on the device used for interpretation of the results. The amplitude of the energy and the return time indicate the shape and location of the flaw in the work piece. However, if it does not encounter a defect, it goes through the structure without obstacles. This possibility allows to measure objects' depths and relevant dimensions of the structure involved in the testing. The first relevant division within the category is in pulse-echo and through transmission methods. The former concerns the measurement of the wave energy either using the same transducer as emitter and receiver or by positioning the two onto the same surface. On the other hand, through transmission ultrasound (TTU) is a method where transmitter and receiver are located into different surfaces and the result is a signal proportional to the energy transmitted through the material or structure involved in the testing. The relevant advantages of these techniques are speed of scan, sensibility to both surface and sub-surface discontinuities, good resolution and flaw detection capabilities. Instead, the disadvantages are difficulty to set up the test, necessity for an accessible surface to transmit ultrasonic/sonic energy, extensive skills and training and the need of test samples to ensure adequate testing. Ultrasonic and sonic testing have been used in a different variety of fields due to their versatility and reliability. Interesting applications of ultrasonic techniques can be found in the automotive industry to inspect adhesive bonds between thin metal sheets [36] or welded joints [37]; Aerospace industry uses it to inspect the condition of carbon fiber reinforcement plastics/polymers [38], [39]; maritime industry uses them for quality control after manual welding in order to find voids, defects and inclusions [40]: Moreover, by exploiting Lamb waves, it is possible to inspect larger areas of structures, such as pipelines and surfaces, since these longitudinal guided waves are able to propagate for long dimensions guaranteeing an adequate Signal to Noise Ratio (SNR) [41], [42]. Figure 2.5 highlights the general set-up of an ultrasonic/sonic test.

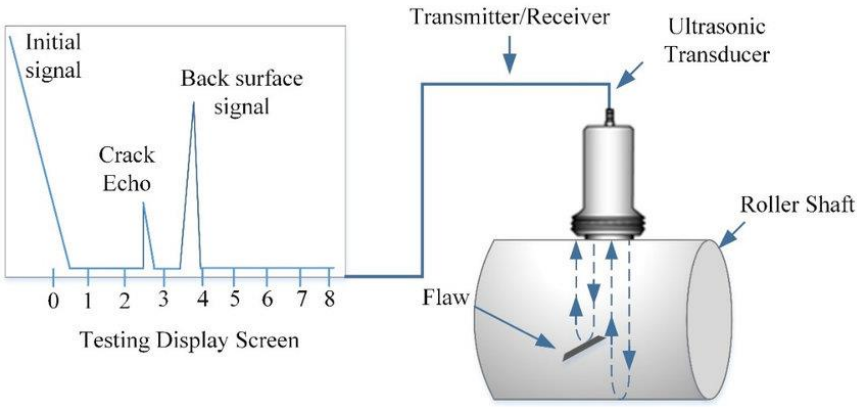

Figure 2.5 Ultrasonic Testing schematic

As it is possible to notice in Figure 2.5, the presence of a flaw affects the signal acquired by the receiver. By knowing the propagation velocity of the wave, it is possible to locate the flaws in the material. Ultrasonic/sonic testing can be further categorized considering the position of transmitter and receiver. Figure 2.6 characterizes three different testing modes.

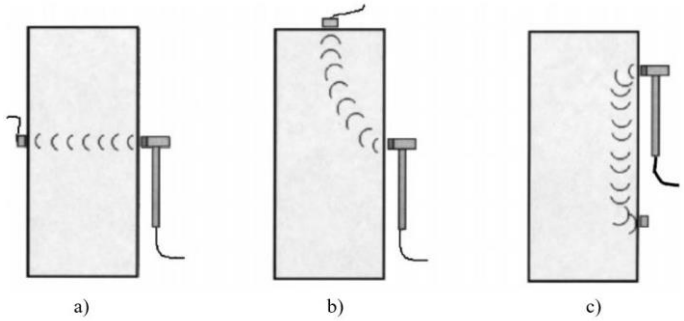

Figure 2.6 Transmission modes: (a) direct; (b) semidirect; (c) indirect.

In direct mode, the signal acquired is the direct wave and no reflections are considered. This mode is useful to locate flaws within the structure and it is a point-to-point test. The resulting wave velocity is an average of the local velocity along the path and it is not possible to establish the position or the extent of any possible anomaly. The other two tests regard the acquisition of emitted waves' reflections. They are often used for tomographic surveys. In general, direct modes are easy to implement and to arrange since the main concern is the arrival time of the first wave, whereas in indirect modes the results consider complex wave frequencies and reflections. Anyway, the fundamental concept behind each different type of testing is the detection of flaws. This is possible since sonic/ultrasonic waves cannot transmit through air gaps, therefore a propagating wave must find a path around a flaw like a void or a crack, attenuating its energy and increasing the transmit time of the signal, enabling the detection. An example of indirect transmission methods is sonic tomography. In this case, there are several reflections of the emitted waves, creating a dense net of ray paths. Each ray represents a different travel time between sonic source and receiver; thus, it is possible to reconstruct a velocity distribution across the structure, as it is possible to see in Figure 2.7. The identification of local variations in velocity can be correlated to weakness spots or flaws within the structure. Figure 2.7 shows an example of velocity map, highlighting iso-velocity zones.

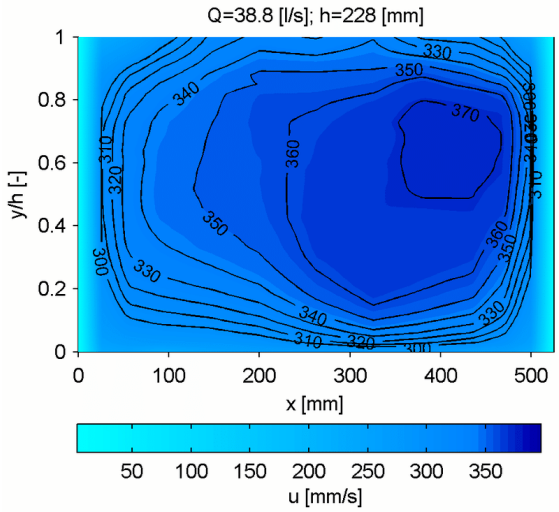

Figure 2.7 Velocity distribution in sonic tomography testing

It is possible to notice the presence of iso-velocity curves representing different velocity distributions, by which different regions where it is likely possible to encounter flaws and anomalies can be identified. For a further understanding towards this direction, interested readers can refer to the work of Schomberg et al. in [43]. A recent development of sonic/ultrasonic methods is known as impact-echo testing. The impact-echo system, also called pulse-echo system, is based on the use of impact-generated stress waves that propagate through the material and are reflected by internal flaws and external surfaces. It was originally developed to measure concrete thickness and integrity of surfaces. It is a method able to determine location and extent of defects such as cracks, delamination, voids or honeycombing shape. Moreover, it can also provide measurements of thickness if no internal anomalies are detected. If properly used, impact-echo testing achieves unparalleled success in locating flaws and anomalies in a variety of applications such as pavements [44], bridges [45], buildings [46], tunnels [47], and many other structures. It is a point-by-point method, meaning that the measurement is performed in one targeted area of the surface and no information about the rest of the surface is available. It is based on the use of transient stress waves generated by elastic impact. A graphical explanation of the method is shown in Figure 2.8. A short mechanical impact, usually produced by using an instrumented hammer, is used to generate stress waves that propagate into the structure and aim to be reflected by possible flaws or the external surface. Adjacent to the point of the impact, a transducer is used to record any possible wave reflection by measuring surface displacements. The relevant difference with the previous mentioned ultrasonic techniques is that emitter and receiver are located on the same surface, thus direct method.

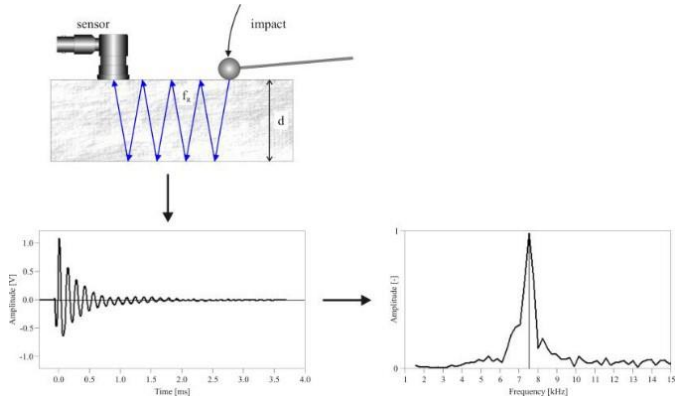

Figure 2.8 Impact-echo testing

The resulting displacements versus time signals are transformed in the frequency domain, usually by means of fast Fourier transform (FFT). A set of frequency response functions (FRFs) are then calculated and possible reflections or echoes of the compressional waves' energy are indicated with resonance frequency peaks. These peaks correspond to thickness or anomalies' location within the structure. By knowing the velocity of propagation of the compressional waves, constant within the material, and the frequency at which the resonance peak is achieved, it is possible to quantify the distance between the receiver and the detected anomaly. If the material is sound, this measure will correspond to the depth of the structure being tested. Figure 2.9 shows possible results of an impact-echo test.

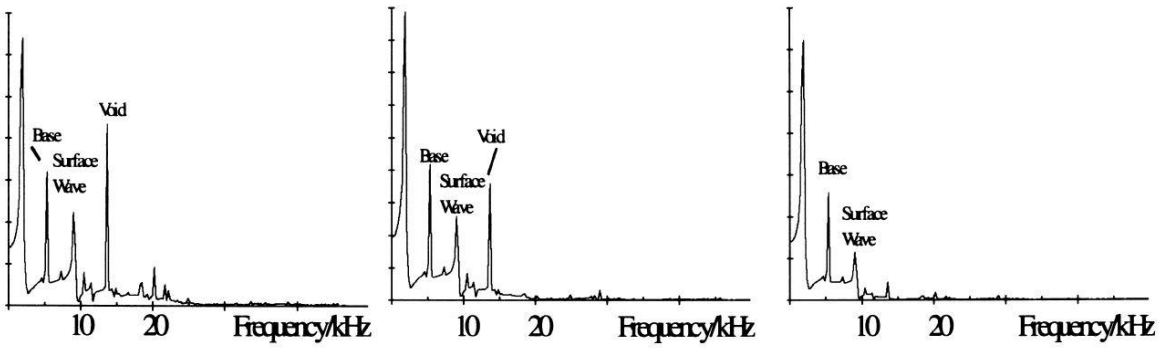

Figure 2.9 Frequency response functions obtained with an impact-echo test.

As it is possible to notice the interpretation of the FRFs is not very easy therefore, an accurate analysis of the results along with adequate expertise is needed. Impact-echo testing of bridges has largely been focused upon identifying voids in ducts in post-tensioned concrete bridges. Finite element (FE) analyses of a laboratory experiment at the University of Edinburgh showed that defects can be identified provided that a sufficiently high frequency is guaranteed [48]. However, in practice it is often not that straightforward. The ambiguity between theoretical and actual behavior is due to different reasons:

- three-dimensional dispersion of the impact-echo wave through the material due to presence of aggregate and other irregularities;
- possible reduction in frequency of the impact-echo signal due to crumbling of the material surface resulting in longer time and then lower frequency;
- possible lack of sensibility of the transducer.

In general, to obtain reliable results it is necessary to maximize the amount of experimental data and acquisition in each test, ensuring a good coverage of the path or the area under analysis. Moreover, an accurate analysis of the results is important to understand if data exhibit a good deal of wave scattering, resulting in variation of the energy transmitted and the transit time. For a more accurate analysis of ultrasonic and sonic testing techniques, interesting readers should refer to [49].

2.2.2 Visual Inspection

Visual Testing (VT) is the basic and most common NDT methodology. By means of a trained, unaided eye it is possible to evaluate in first approximation possible damages and defects in structures, allowing to save both time and financial resources with respect to most complex nondestructive methods. It is in general the first test carried out and it is often used to understand which type of test is suitable for different applications. VT is not so effective in detection of anomalies but in any case, it is easy and quick to perform. In almost all industries it is used as initial testing approach and the environment of the test is crucial to achieve satisfactory results. It can either be performed in person or remotely, exploiting several different tools as for instance, augmented reality or virtual reality. VT can be also be performed with cameras, allowing in general a more accurate analysis of the material tested. Among all, 3D digital image correlation is a well-known nondestructive methodology to assess the presence of superficial defects and more in general to understand the behavior of a structure. More details about this technique are outside the topics of this research, therefore interested readers can refer to the work of McCormick et al. in [50]. Other application of visual testing can be performed with special equipment such as hand-held lenses, measuring magnifiers, microscopes, etc. VT is used in a variety of different applications, as for instance in aerospace industry to inspect hardly accessible areas of the fuselage [51], or in those applications where the purpose is to detect surface flaws such as porosity, corrosion, ruptures or cracks. In some cases, it also possible to detect sub-surface defects if the structure is transparent or semi-transparent [42]. In any case, VT does not provide accurate detection's outcomes when compared with other methods, therefore it should be used as initial methodology to assess superficial conditions of structures and to decide which NDT method used for a more meaningful analysis.

2.2.4 Acoustic Emission Testing (AET)

Acoustic Emission Testing (AET) is an NDT method that is based on the generation of waves produced by a sudden redistribution of stress in the material. It is a passive method, which means that the detection of a flaw depends on the energy emitted by the flaw source itself. When a structure is subjected to an external stimulus (change of pressure, load or temperature), the material responds by releasing energy in the form of stress waves, which propagate in the material and therefore can be recorded with proper sensors. The radiation of elastic stress waves occurs when a flaw initiates or propagates and lead to acoustic emissions that cause mechanical disturbance. Causes of acoustic emissions can be either natural, such as earthquakes or rock bursts, or from the material itself, by means of growth of cracks, slip and dislocation movements, melting or phase transformations in metals. The origin of acoustic emission is divided into macroscopic and microscopic origin. The former refers to circumstances where a large part of the structure is contributing to the acoustic emission. Examples of this behavior can be yielding, crack growth, corrosion for metals, fiber breakage and matrix debonding for composites. On the other hand, microscopic origin concerns smaller anomalies sources compared with the previous category, in terms of volume or area. Examples of this might be phase transformation of materials, microcracks and dislocation movement. Most of the time, mechanical disturbance manifests itself by means of surface

displacements or vibrations that are converted into an electrical signal by an AE transducer. Figure 2.10 highlights the schematic of an AE testing.

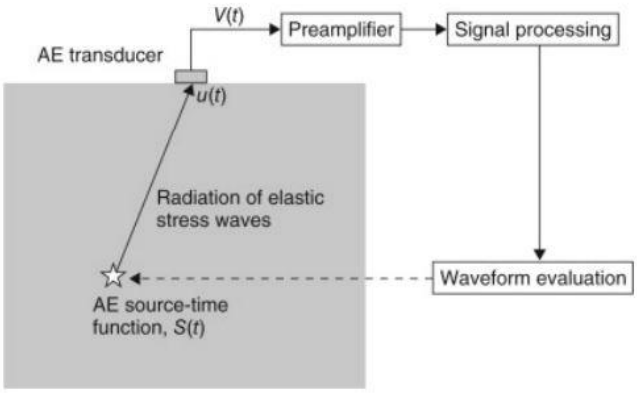

Figure 2.10 Schematic of AE testing and basic instrumentation

AET equipment generally is constituted by a sensor, preamplifier, filter and amplifier, along with measurement, display, and storage equipment. AET is different than other NDT techniques in two major ways:

- instead of exciting the object under inspection, the purpose of AET is to measure the energy released by the object naturally. Provided that, AET can be often performed on structures while they are operating since the load provides an adequate amount of excitation able to stimulate defects and trigger acoustic emissions;

- AET deals with dynamic processes, therefore only active features are highlighted during the examination. Thus, it is possible to define developing and stagnant defects.

More in general, if the load isn't high enough, possible anomalies can go undetected. In fact, frequency and amplitude of the recorded signal depend on the origin and type of flaw source. AET provides a reliable tool to detect qualitatively flaws. Unfortunately, a quantitative analysis of defects is not possible, therefore this technique is usually followed by ultrasonic testing to quantitatively evaluate the anomalies detected. Figure 2.11 represents an AE signal response, along with the most relevant parameters for detecting anomalies.

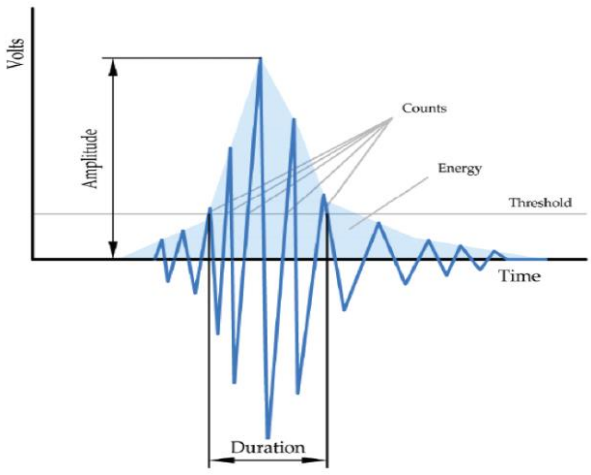

Figure 2.11 Waveform time signal of an AE testing

This type of testing is used in different industrial applications. Topolar et al. in [52] used AET to monitor cement composites; it is used in testing industrial equipment such as centrifugal pumps [53]; in testing electrical

components such as superconductors [54] or in testing carbon fiber composites delamination [55]. Also in the building's sector, it is a technique widely used for classify anomalies in reinforced concrete beams [56].

2.2.5 Electromagnetic Testing (ET)

This category of nondestructive testing exploits the fundamental electromagnetic laws to detect superficial and sub-surface defects. Generally speaking, it is the process of inducing electric currents or magnetic fields or both into the object being tested and obtaining as an outcome an electromagnetic response, different depending on the type of test carried out. These methods are used to detect or measure fractures, corrosion, faults or other damages related to conductive materials. The result of the test is the analysis of specific magnetic properties and geometries of the structure under inspection, along with possible anomalies. Within the category, it is possible to distinguish different types of methods that basically differ from a physical point of view, even though the outcome is always the same. Among all, the most relevant ET techniques are Eddy Current Testing (ECT), Remote Field Testing (RFT), Magnetic Flux Leakage testing (MFL), Magnetic Particle Testing (MPT) and Near Field Testing (NFT). MPT is a nondestructive testing used to detect surface or sub-surface defects and discontinuities. It can be used in those materials that can be magnetized, namely ferromagnetic metals. In fact, ferromagnetic materials such as iron, nickel and cobalt and some of their alloys, are strongly attracted by magnetic couplings. The equipment used in this method is a magnetic yoke, used in order to recreate a magnetic field in the component under investigation. Figure 2.12 represents the instrument.

Figure 2.12 Magnetic yoke for magnetic particle testing

Other possible sources of magnetization can be permanent magnets or coils inducing current that interacting with ferromagnetic materials produce a magnetic field. The piece can be either magnetized by direct or indirect magnetization. The former appears when an electric current is passed through the material and its ferromagnetic characteristics create a magnetic field while indirect magnetization is the result of the application of a magnetic field from an external source like in the case of a magnetic yoke. The presence of discontinuities or defects is manifested as a magnetic flux leakage since air cannot support as much magnetic field per unit volume as metals.

Therefore, by identifying the location of the leakage, it is possible to identify flaws and anomalies. By knowing the current flow direction induced in the component, it is possible to identify the direction of the magnetic lines, perpendicular to the current direction, going from north to south pole. At this point, it is sufficient to apply ferrous particles to the surface of the component and see their behavior to understand if damages are present. In fact, when there is flux leakage, an additional north and south poles will be created on the boundaries of a discontinuity, enabling the ferromagnetic particles to gather around the anomaly. This attraction allows to clearly identify the location of the anomaly. Figure 2.13 highlights the principle of work of a magnetic yoke along with the characterization of the magnetic field in correspondence of a flaw.

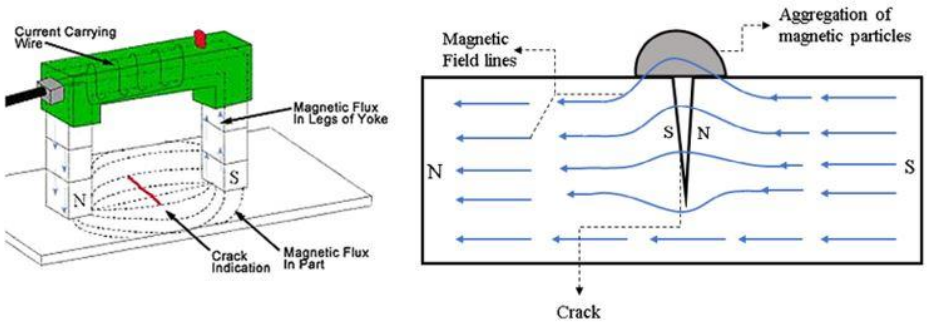

Figure 2.13 Principle of operation of magnetic field leakage testing

The particles applied to the structure being tested can be either dry or wet, using liquids as kerosene or similar petroleum distillate to create the mixture to spread on the surface under examination. To provide better contrast with the object and enhance the sensitivity of the result, particles are usually coated. Basically, there are two different types of coating, color contrast and fluorescent. The former is just a matter of what color suits better the application based on the color of the object tested. Fluorescent particles are effective in dark backgrounds since they emit light when surrounded by a black light. Magnetic particles testing is a powerful and reliable technique to detect both surface and near sub-surface defects. Moreover, some inspections formats are extremely portable and low cost, guaranteeing a rapid inspection with immediate results. MPT is largely used in those parts which have irregular shapes since they don't care about the geometry of the object being tested. However, the methodology carries also some drawbacks. First, the specimen must be ferromagnetic, narrowing the inspection to just a class of structures; then, painting stratus thicker than 0.1 mm should be removed prior to the inspection to guarantee adequate results. Moreover, post cleaning and post demagnetization is often necessary as well as alignment between magnetic flux and defect should be guaranteed. The results of an MPT using fluorescent particles is shown in Figure 2.14.

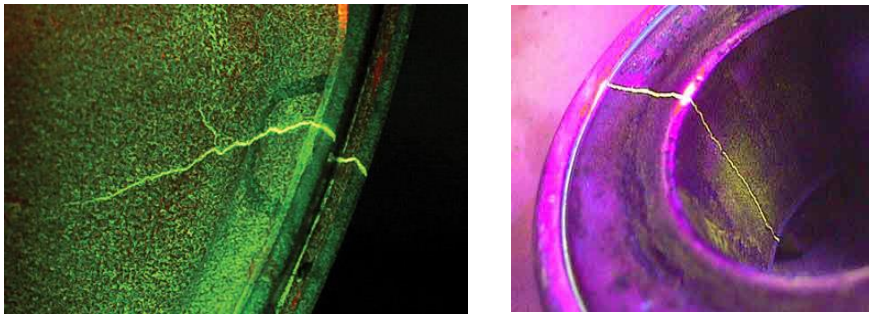

Figure 2.14 Magnetic particles testing using fluorescent particles

As you can see from Figure 2.14, the presence of particles allows to detect flaws in ferromagnetic components, otherwise non-detectable with a visual inspection. Relevant applications of the technique concerns the automotive industry [57], as well as the inspection of materials at a microscopical levels [58]. Another relevant electromagnetic testing is Eddy Current Testing (ECT). It can be applied to conductive materials only and it bases its working principle on the generation of eddy currents in the material under analysis. In fact, the probe used for testing is basically a coil of conductive material that is excited with an alternate current. The interaction between the conductive material of the coil and the current produces a magnetic field around the probe. When the coil approaches the object under analysis, currents are induced into the material, called eddy currents since they flow in opposite direction with respect to the ones produced by the coil. Variations in the magnetic permeability, electrical conductivity or the presence of defects generate an eddy current's change in terms of amplitude and phase. Moreover, eddy currents flowing in a conductive material create a magnetic field. Since the direction of the current is opposite to the direction of the current in the coil, also the magnetic field induced will have opposite direction with respect to the one generated by the set of coils. By measuring the impedance changes in the coil, directly related to changes in the overall magnetic field, it is possible to evaluate the presence of

anomalies in the material under analysis. Figure 2.15 summarizes the working principle of a generic eddy current testing.

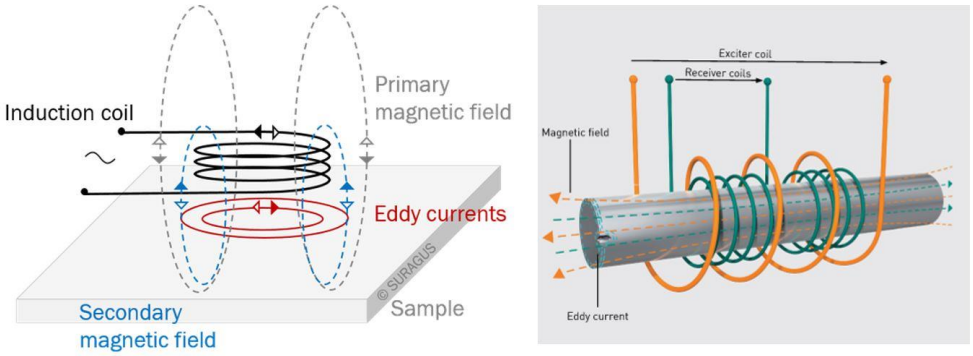

Figure 2.15 Principle of operation of eddy currents testing

ECT is often used to detect superficial or near-surface defects, since its probability of detection strongly decreases as the anomaly's location is far from surface. A common parameter used to understand at which depth it is likely possible to detect an anomaly is the Standard Depth of Penetration (SDP) δ, defined as the depth at which the eddy current density has decreased of 37% with respect to the surface density value. It is usually advisable to conduct tests within 1δ, to ensure proper and reliable results. On the other hand, there are cases in which the test can be conducted at different SDPs, as for instance when the aim is to determine the material's conductivity, for which the SDP value is 3δ. The two more relevant applications of ECT are surface and pipeline inspections. In general, the former can be performed both in ferromagnetic and non-ferromagnetic materials. On the other hand, tubing inspection is mainly related to non-ferromagnetic materials and the test is often considered the conventional eddy current testing. Figure 2.16 represents an example of result of an EC testing.

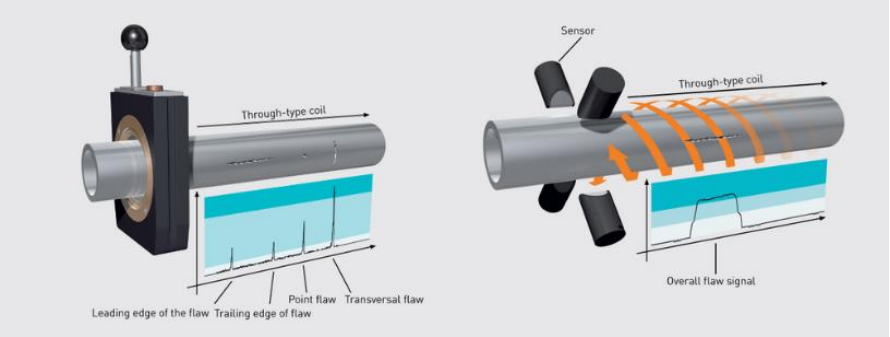

Figure 2.16 Eddy current testing of pipelines

The advantages of this type of NDT methods are sensitivity to surface defects, detection through several layers and surface coatings, if any. Moreover, the test is portable and can be fully automated, guaranteeing accurate conductivity measurements. On the other hand, it is susceptible to magnetic permeability changes and requires a signal interpretation. Furthermore, it is not able to detect defects parallel to the surface and it is not suitable for inspecting large areas or complex geometries. For a more detailed analysis of this technique, interested readers can refer to [59], where ECT is compared with another type of electromagnetic test. ECT is used in different applications, such as weld inspections [60], pipelines and tubes [61] and for testing materials at microscopic level [62].

Another important type of testing falling in this category is Remote Field Testing (RFT), whose main application is in finding defects in steel pipes and tubes. The motivation behind this test is to compensate the difficulty of eddy current testing to inspect the full thickness of the tube wall due to strong skin effect in ferromagnetic materials. This difficulty can be overcome with RFT since it guarantees nearly equal sensitivities

of detection at both inner and outer surfaces of a ferromagnetic tube. On the other hand, when inspecting nonferromagnetic materials, RFT is in general less sensitive than eddy current testing. The basic principle of operation is the same as eddy current testing, using a probe to create a magnetic field and consequently eddy currents in the material under inspection. The difference is that exciter and receiver coils are placed inside the tube at a fixed axial distance. The presence of eddy currents and the nature of the material create an inducted magnetic field that opposes to the one generated by the probe. In general, the eddy current field is more spread out than the exciter field, therefore it extends farther along the longitudinal tube axis. Provided that, the receiving coil is placed at a distance where the magnetic field generated by eddy currents is the dominant one, so that by measuring the voltage induced in this coil it is possible to monitor changes in the magnetic field, directly related to eddy currents, that allows to identify possible anomalies in the test specimen. The location in which the receiver is placed is called remote zone, giving the name to the technique. In general, a suitable distance among emitter and receiver coils is two to three times the diameter dimension of the tube. Figure 2.17 summarizes the principle of operation of the test.

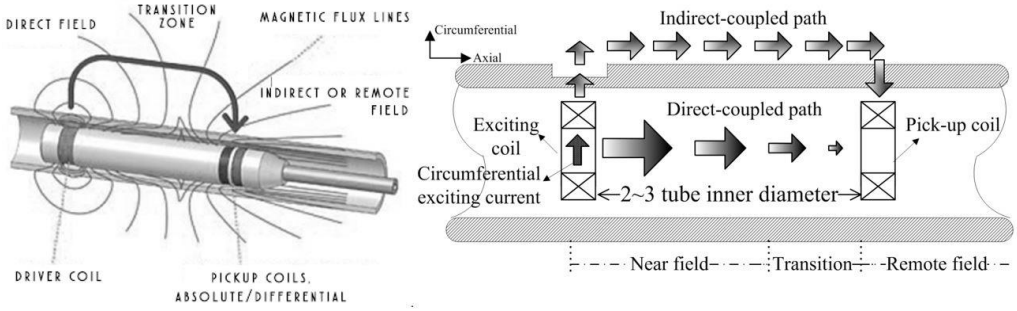

Figure 2.17 Principles of Remote Field Testing

Overall, the main difference between this method and eddy currents testing is the coil-to-coil distance, otherwise the principle of operation is the same. Therefore, RFT has the possibility to inspect large areas of a component, very useful when it comes to pipelines and tubes. The resulting signal is the voltage measured at the receiving coil of the instrument. Two different signals can be identified, voltage versus time and voltage versus phase angle. By looking at voltage variations both in time and phase, it is possible to correlate picks to anomalies' locations in the specimen being tested. A variation of this technique is called Near Field Testing (NFT) where the main difference is the position of the receiver coil. In fact, it is positioned in the so called near-field zone, i.e. the zone where there is a combination of the two magnetic fields involved in the test. Basically, the difference with RFT is that the receiver is placed closer to the transmitter coil and it is often used for aerial cooler carbon-steel tubing inspections.

The last technique relative to electromagnetic testing is Magnetic Flux Leakage (MFL). It is a fully magnetic method that is used to detect corrosion and pitting in steel components. The principle of operation is very simple, a magnet is used to magnetize the component under inspection and a magnetic detector is placed in between the magnet's poles. Figure 2.18 shows a schematic of the process.

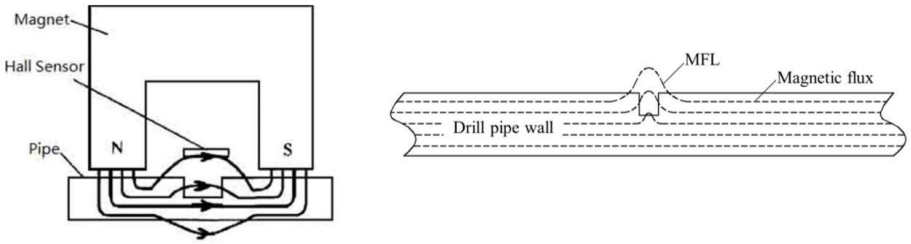

Figure 2.18 Schematic of Magnetic Flux Leakage testing

As it is possible to notice from Figure 2.18, whenever a defect is present in the magnetic flux path, there is a flux leakage since the magnetic permeability of air is lower compared with the one of steel, therefore a reduction of magnetic flux is present. By placing the detector between the poles, it is possible to measure the amount of magnetic loss in presence of an anomaly in the material. Usually, the sensor used as magnetic detector is a Hall effect sensor, that is able to measure the magnitude of a magnetic field. It provides a voltage as output proportional to the magnetic field measured. Generally speaking, the larger the change in the detected magnetic field, the larger the anomaly. A drawback of this method is that it is only able to identify the presence of a flaw but not its location. Often, an eddy current sensor is used to indicate the surface location of the anomaly or whether the defect is placed on the internal or external surface of the pipe under inspection. Its main application is in the pipeline industry, to check for cracks [63] or other anomalies [64].

2.2.6 Laser Based Testing

Another important branch of nondestructive testing is related to the usage of laser-based technologies to detect possible anomalies in structures or simply measure shapes, thickness or material's properties. Among all, the most widely recognized techniques based on this technology are Shearography, Holography, Profilometry and Laser Speckle methods. First, it is necessary to introduce a technique shared among all of them that is Interferometry. Basically, the aim is to produce interference between electromagnetic waves, and measure their amplitude and phase shifts. When two waves of same frequency combine, the resulting intensity pattern is determined by the phase difference among the waves. In fact, if two waves are in phase, it is possible to talk about constructive interference, meaning that the amplitude of the resulting wave is doubled; whereas, if the two are out of phase the effect is called destructive interference and the resulting amplitude is zero. To better understand the meaning of interference, Figure 2.19 shows two examples of interference.

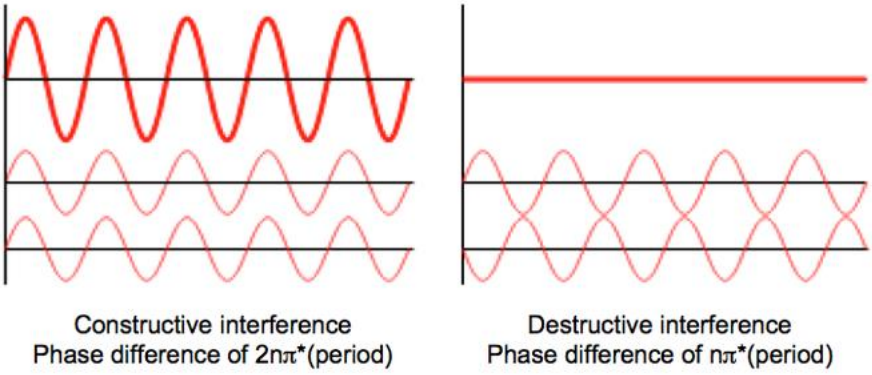

Figure 2.19 Constructive and destructive interference

These are the limit cases of the superimposition of waves; in the middle, several different types of interference can occur. The outcome of this superimposition is a pattern of frequency fringes, as it is possible to see in Figure 2.20.

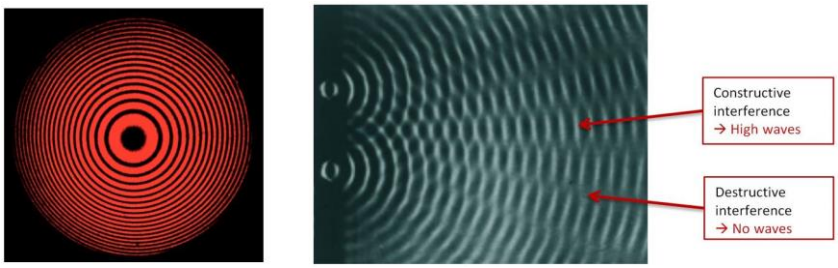

Figure 2.20 Fringes patterns

As it is possible to see in Figure 2.20 on the right, each black fringe corresponds to a situation of destructive interference. On the other hand, the image on the left shows a natural example of wave interference. To acquire fringe patterns, the generic equipment of the test is as follows:

- laser source, producing a coherent light (monochromatic);
- beam splitter, partially reflective mirror used to split into two identically beams the laser beam coming from the source;
- two fully reflective mirrors that receive the beam of light and reflect toward other directions depending on the type of test;
- detector, where the combined electromagnetic wave is directed by the beam splitter. The detector is a device able to display the frequency fringe pattern.

The schematic of the mentioned principle of working is reported in Figure 2.21.

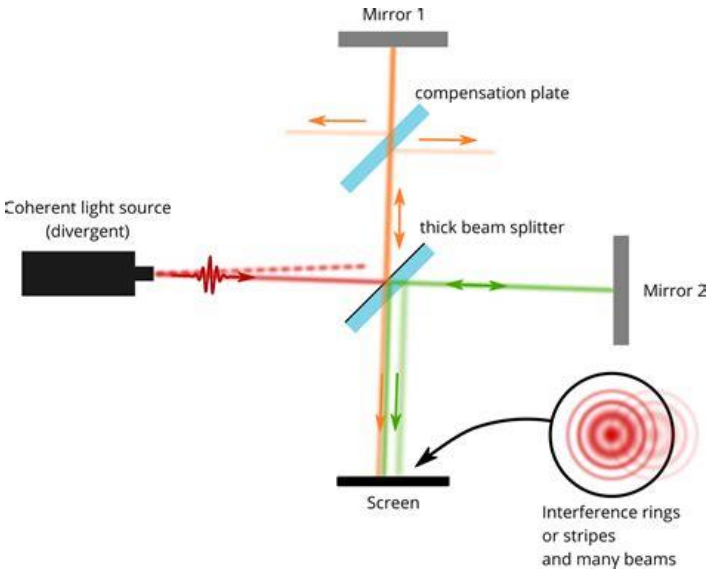

Figure 2.21 Schematic of a laser-based test

It is worth to mention that this is also the basic schematic for interferometry. Depending on the sensors and instrument used, it is possible to identify different techniques. Moreover, when testing materials and structures, one mirror becomes the reference for the test whereas the other one is the specimen under inspection. The difference in phase, therefore the interference between waves, is principally given by the different properties of the material tested. In fact, each material has a different reflective index that drastically change the wave reflected. The reflective index is a dimensionless number that describes how fast light travels through the material. It is defined as

$$n = \frac{c}{v}, \tag{2.8}$$

where c is the speed of light in vacuum and v is the phase velocity of light in the medium, the material analyzed. For instance, for water this index is 1.33 meaning that light travels almost 30% faster in vacuum than in water. Depending on the schematic used and the outcome, different methods are based on interferometry.

Shearography is a laser-based optical NDT method that uses coherent light to inspect surfaces. The main characteristic of a coherent light is that the phases of all electromagnetic waves at each point on a line normal to the direction of the beam are identical. This means that it is usually monochromatic. Shearography is an

interferometric inspection technique, where the electromagnetic waves are superimposed, causing the phenomenon of interference, which is used to extract information about the component under inspection. Generally speaking, the sample under test is "illuminated" using a laser so that a speckle pattern is formed and imaged on a CCD camera by means of a shearing device. The latter combines the speckle pattern obtained in the above process with an identical one laterally displaced in a coherent way. The aim of the shearing device is to divide the image so that two identical, but displaced, images are recorded by the CCD camera. This allows to look for changes in the image when passing from a loading to an unloading condition. Often, a beam expander is placed in between the laser source and the object to expand the diameter of the light beam generated. Usually, images are recorded before and after a loading condition and the combination of the images results in a fringe pattern. Figure 2.22 represents a possible schematic of a shearographic test.

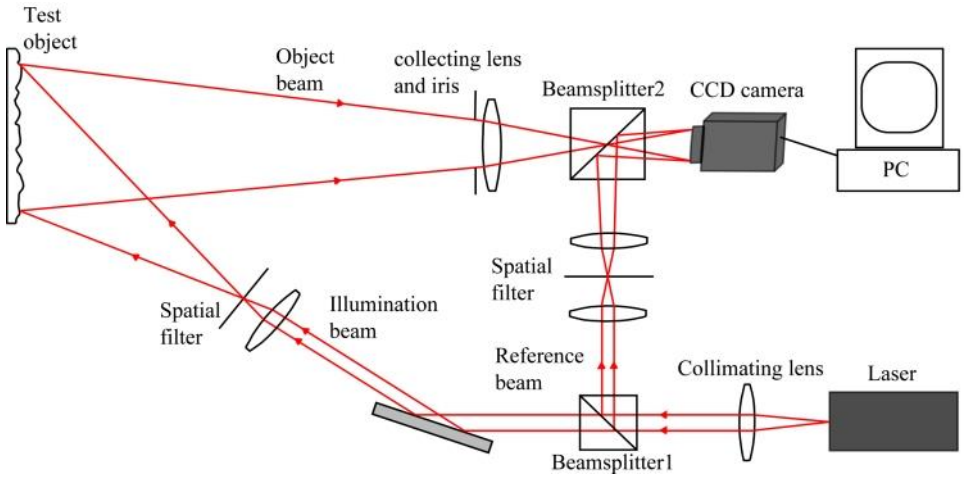

Figure 2.22 Shearographic test schematic

In general, the lateral displacement is called the shear of the image. The result of the test is a superposition of two images, called shearogram, which is an interferogram of an object wave and the sheared object wave used as reference wave. By comparing two different shearograms, in load and unload conditions, it is possible to define an interference fringe pattern that is directly related to the difference in deformation state. In the case of shearography, frequency fringes represent the slope of the deformation, whereas in other techniques the meaning could be different. In other terms, the phase of the fringe pattern contains information about the displacement derivative of the surface. This technique can be used to detect defects as well as to conduct structural analyses and fatigue testing inspections. An example of the results obtainable with this technique is shown in Figure 2.23.

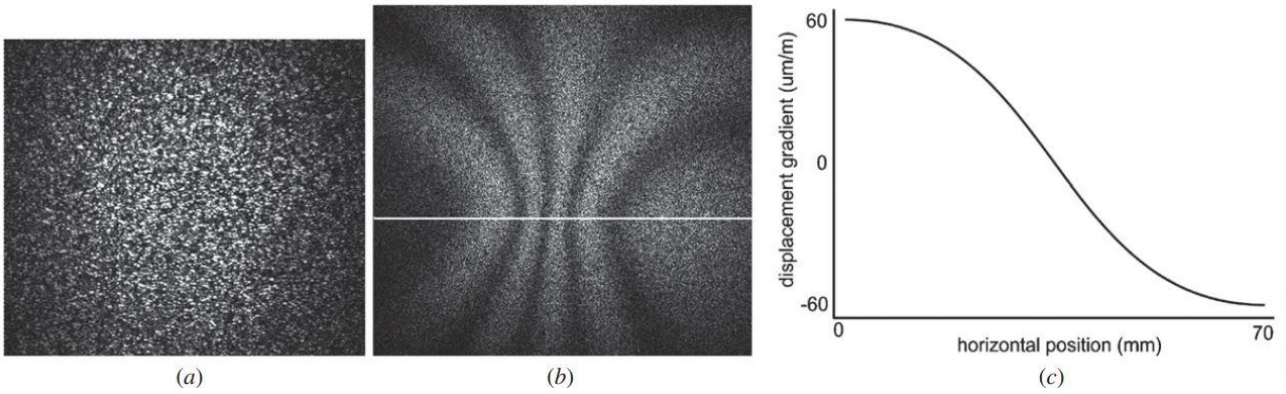

Figure 2.23 Shearogram of a metal element

Figure 2.23 a represents a typical speckle pattern, shearogram, coming from the combination of two different images, frontal and lateral. Instead, Figure 2.23 b shows a correlation fringe pattern obtained using an

out-of-plane sensitive shearography system, whereas Figure 2.23 c approximates the displacement gradient versus the horizontal position along the white section line of Figure 2.23 b. The reliability of shearography is related to the fact that the object under testing is used as reference. In fact, by comparing sheared image and normal image, the method is less sensitive to external noise and vibration. For more details about the mathematical principles behind shearography, interested readers can refer to the work of Francis et al. in [65], providing a very good review of the method. Shearography is used in a variety of industrial applications, such as the aerospace industry to test composites material of helicopters [66]; for inspecting wind turbines [67], in general to test metallic structures [68] or to extrapolate properties mechanical properties from beams in the construction industry [69].

Another important methodology related to laser technology is Holography. The basic principle of operation is the same as shearography, exploiting interferometry. It is an optical method whose aim is to record amplitude and phase of light reflected from an object as an interferometric pattern on a paper film. In practice, it reconstructs a full 3D image of the object. The component under analysis is subjected to different stressed states and the interferometric fringe pattern is compared with the unstressed state pattern. In fact, it is possible to define the contours of the deformation undergone by the specimen in between two recordings. When a material shows an anomaly, either superficial or sub-superficial, the pattern shows distortions with respect to the sound uniform pattern. Holography can be also used to measure vibration modes, mechanical stress and more in general the characteristics of the component under inspection. It is used to detect impact damages, corrosion, delamination, debonds and cracks. Compared to shearography, holography has the same set-up apart from the shearing element. The important difference between the two is that in shearography the fringe pattern is directly related to the displacement derivative of the surface, whereas in holography the fringe pattern is a direct measure of the deformation. An example of results obtainable with holographic testing are represented in Figure 2.24.

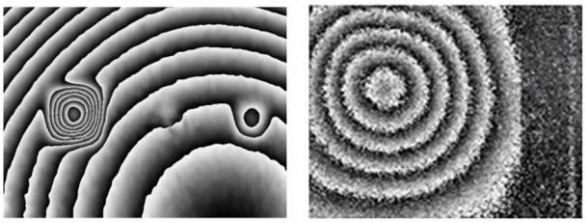

Figure 2.24 Holographic testing results

In practice, there's no difference between shearography and holography in the set-up, but the results obtained are related to different quantities. The advantage of this technique is that it can be used for any object, independently from shape and dimensions. A novel development of this technique is called Electronic Speckle Pattern Interferometry (ESPI) or also "TV holography". It exploits a video camera for image acquisition which is coupled with a computer image processing system. Basically, the correlation between speckle patterns, before and after the object has been deformed, is carried out using image processing techniques. The schematic of the methodology is a bit different when compared to basic interferometric holography and it is shown in Figure 2.25.

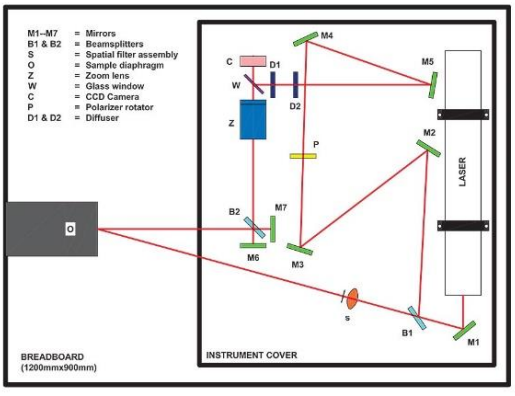

Figure 2.25 Electronic Speckle Pattern Interferometry

For further details about this methodology, interested readers can refer to [70], [71]. The last technique related to the application of laser beams as input source is called Profilometry. It is a technique used for surface inspections and profile measurements based on the triangulation principle. The purpose is to get the surface's morphology, step heights and surface's roughness. The technique can be performed using two different instruments, stylus or optical profilometer. The first one is not related to laser sources since a probe is just passed through the surface and roughness is measured by means of a control feedback loop able to maintain the probe around a known set point. Instead, an optical profilometer exploits a light source to achieve the same results, basing its nature on interferometry as well as the other two methods explained before. The basic schematic of the procedure is presented in Figure 2.26.

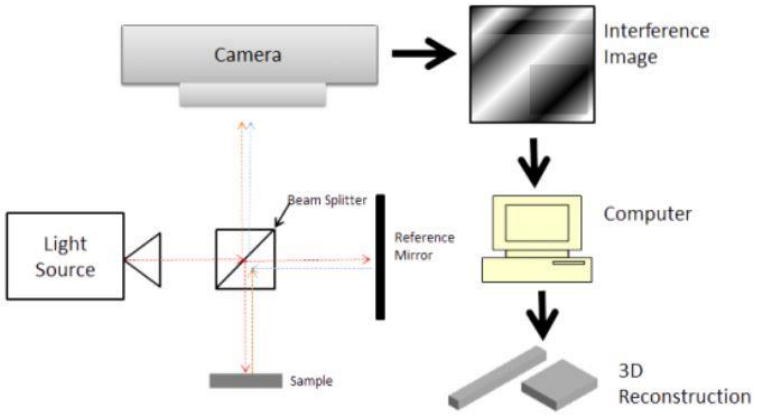

Figure 2.26 Schematic of an interferometric profilometer

The same principles of interferometry are applied for profilometry and the outcome is a 3D reconstruction of profiles and surfaces. Basically, to measure the shape of the surface, the object being tested is moved relative to the measurement system in a way that changes in the fringe pattern are directly related to the dimensions of the object and the properties of its surface. For further details about the mathematical reasoning about optical profilometry, interested readers can refer to the work of Giesko et al. in [72], where an adequate overview of the method is provided. An example of a profilometry test is shown in Figure 2.27.

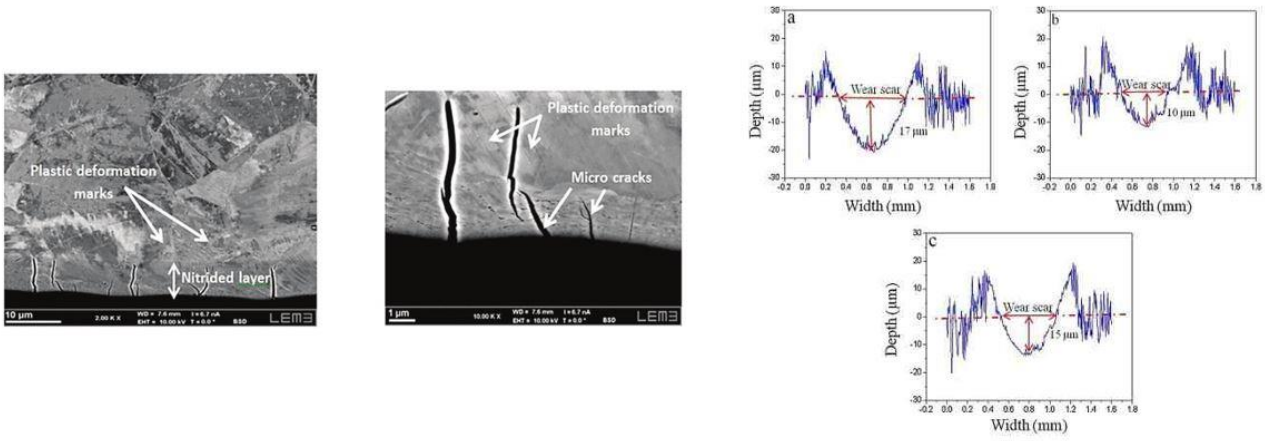

Figure 2.27 Profilometry test

Optical profilometry is used in a variety of industrial application as for example in the dental industry to characterize the surface of teeth [73], or in the characterization of MEMS and MOEMS systems [74]. Another application of this technique is in the construction's industry to measure surface roughness of different types of

concrete materials. For instance, Garbacz et al. in [75], conducted a study to characterize concrete's surface roughness and surface geometry using different profilometry tests.

2.2.7 Ground Penetrating Radar (GPR)

This NDT methodology relies on the usage of high frequency radio waves (10 MHz up to 2.6 GHz). It is a technique that uses radar pulses to image the subsurface. It can be applied in very different media, including rock [76], ice, water [77], pavements and concrete [78]. It is used to detect subsurface defects and anomalies, as well as changes in material properties, voids and cracks. Radio waves are electromagnetic (EM) waves characterized by relatively low frequency content and consequently large wavelengths (~1 mm). The behavior of them is influenced by different factors, such as magnetic permeability μ, electric conductivity σ and dielectric permittivity ε. The first two control the attenuation and partially the depth of penetration of the EM signal. In fact, highly conductive materials result in signal dissipation and loss. Other factors that affect the penetration and the resolution of the GPR method are the sensitivity of the antenna and its frequency as well as the settings of the control unit embedded in it. The basic GPR system is composed by a transmitter that is usually an antenna that emits electromagnetic energy towards the object being tested. Each time the radio waves encounter an object below surface or in general something with a different permittivity than the one of the medium being tested, part of the wave is either reflected, refracted or scattered towards the surface where a receiver antenna is there to record the signal. The amplitudes of the received echoes and the corresponding arrival times can then be used to determine the nature and location of the discontinuity. Figure 2.28 shows a sketch of the instruments used for a GPR test.

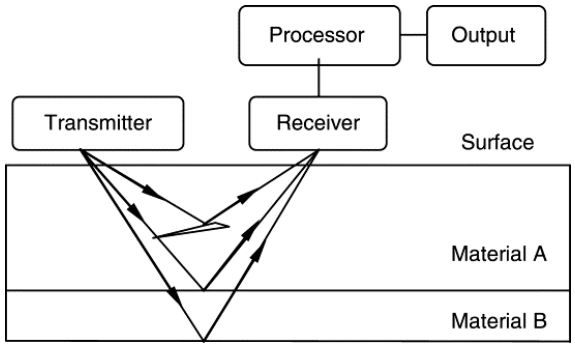

Figure 2.28 Basic configuration of a Ground Penetrating Radar

The main configuration of a GPR system is by using impulsive radar systems by which a very short pulse signal (~10^{-9} s), characterized by a central frequency, is transmitted towards the target component and the back-reflected signal is recorded using another antenna. A result of a GPR test is represented in Figure 2.29.

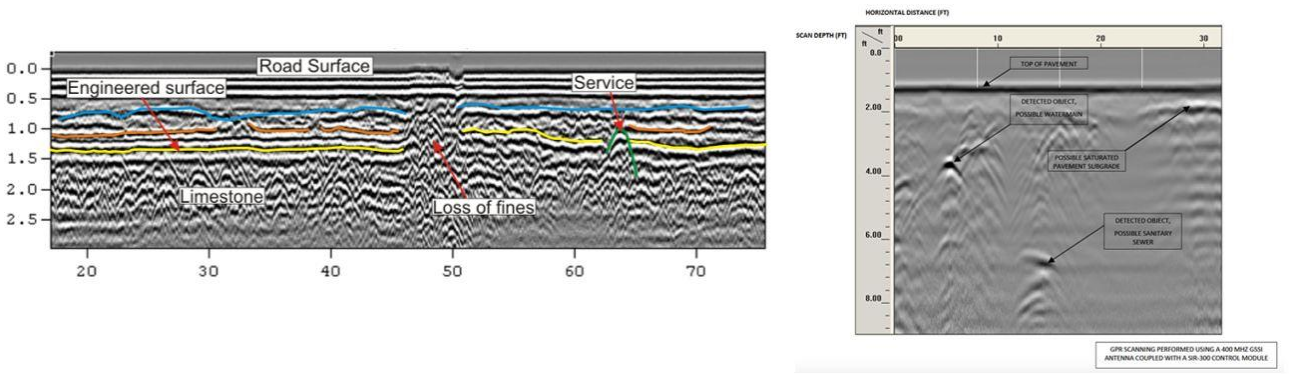

Figure 2.29 Reflected radio waves spectrum

As it is possible to notice, an expert is needed to understand the output signals of a GPR test. In any case, it is possible to characterize the properties of the material being tested by means of different electrical and magnetic properties, as well as it is possible to detect anomalies underneath the surface being tested since defects are in general characterized by different electromagnetic properties. For instance, a subsurface void is filled with air that has different electromagnetic properties compared with a solid material, therefore it is possible to see an anomaly in the radio wave reflected and received by the antenna. For further details about the technique, interested readers can refer to the work of Daniels in [79] or to [78]. Many applications exploit this technique, especially in geophysics. In fact, it is used in geoarchaeology [80], to measure properties of different types of soil [81]; it can be used for detection of leaks in distribution pipes [82] or for inspections of concrete structures [83].

2.2.8 Infrared radiation testing

This category of nondestructive testing exploits the measurement of infrared radiation to extract important characteristics of the material/component being tested along with the detection of anomalies within and onto the surface of the element. Before explaining the different techniques to test structures, it is worth to explain the theoretical basis behind the testing. The electromagnetic spectrum is composed by different types of waves, essentially characterized by different frequencies and therefore wavelengths. Following a crescent order in terms of frequency, it is possible to divide the spectrum in the following categories: radio waves and micro waves, spanning from very low frequencies up to about 150-200 GHz; infrared waves (200 GHz up to about 100 THz); visible waves (about 100 THz up to about 2PHz) and ionizing waves divided in X-rays and γ-rays, characterized by frequencies starting from 2PHz up to 300 EHz. The human eye can detect only the so called 'visible' waves, whose wavelength is roughly in between 0.39 and 0.77 µm. They are basically the result of indirect or better reflected radiation provided by a source of light, either artificial or natural. On the other hand, infrared radiations are non-visible radiations that typically fall in between 1 and 20 µm of wavelength, therefore their frequency is in general lower than that of visible radiations. They can be further divided in Far, Mid and Near infrared radiations, where near radiations are the ones closer to the visible spectrum. Figure 2.30 shows a chart of the electromagnetic spectrum.

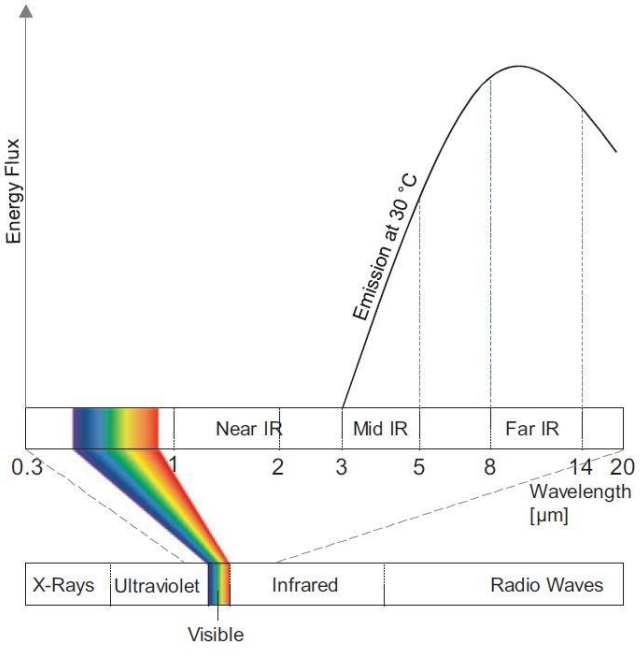

Figure 2.30 Electromagnetic radiation spectrum

The aim of the methodologies explained in this section is to measure the emitted infrared energy of objects and indirectly output the temperature of different parts of the objects. Each object whose temperature is above the absolute zero (0 K) emits radiations, mainly in the infrared spectral range. This radiant energy is transported in the form of electromagnetic waves and travels at the speed of light. The amount of radiant energy emitted depends on the temperature of the object being tested and the emission characteristics of the material. Therefore, each material is different when it comes to radiant energy absorption and not in all cases it is possible to guarantee reliable measurements. For instance, transparent materials such as semiconductors or reflective objects like mirrors are difficult to investigate and in most of the cases it is not possible with these techniques to measure their temperature. The theoretical description of the radiations emitted by a body is based on the so-called black body. The latter is an object which theoretically emits the maximum amount of energy possible at each wavelength and it is characterized by an isotropic behavior, therefore it is independent from the incidence angle of the measure taken. In other terms, its emissivity ε is equal to 1, the maximum value possible. This property is valid even if the object is absorbing energy, therefore a black body is a theoretical body that can absorb all incident electromagnetic radiation, independently from frequency and angle of incidence. The counterpart is the white body, that is characterized by an emissivity ε equal to 0 and the behavior is exactly opposite when it comes to absorption or emission of electromagnetic radiations. Both exist only in theory; therefore, each object is considered a 'grey' object, something in between the two. To understand how a body emits radiant energy, it is worth to start considering a black body. The amount of energy leaving a surface of a black body as radiant heat is described by the Planck's Law of Radiation:

$$L_{\lambda B} = \frac{2hc^2}{\lambda^5 \Omega_0} \frac{1}{e^{\frac{hc}{\lambda T k_B}} - 1}, \tag{2.9}$$

where c is the speed of light in vacuum (approximately 3e5 m/s), h is the Planck's constant, k_B is the Boltzmann's constant, Ω_0 is the unit solid angle in steradian and T is the absolute temperature of the object. The subscript b means that this formulation is valid for black bodies. To use the same formula for real bodies, it is sufficient to multiply Eq. 2.9 for the material emissivity ε_λ, depending on the wavelength. In general, the emissivity of an object is defined as the ratio of the radiant energy emitted by a surface to that emitted by a black body at the same temperature. In order to calculate the radiation flux, the spectral radiant exitance $M_{\lambda B}$ has to be introduced. It is a measure of the radiant flux emitted by a surface per unit area and its formulation is as follows:

$$M_{\lambda B} = \pi \Omega_0 L_{\lambda B}, \tag{2.10}$$

Grouping together constant values from Eq. 2.10 it is possible to obtain:

$$M_{\lambda B} = \frac{c_1}{\lambda^5} \frac{1}{e^{\frac{c_2}{\lambda T}} - 1}, \tag{2.11}$$

With the radiation constants

$$c_1 = 2\pi hc^2 = 3.742 * 10^{-16}\, W m^2 \tag{2.12}$$

And

$$c_2 = \frac{hc}{k_B} = 1.439 * 10^{-2}\, K\, m \tag{2.13}$$

To calculate the radiant exitance in a wavelength range, it is sufficient to integrated $M_{\lambda B}$, between two extrema λ_1 and λ_2, as follows:

$$M_B = \int_{\lambda_2}^{\lambda_1} M_{\lambda B}\, d\lambda \tag{2.14}$$

So far, only one close solution of the integral exits and it is called Stefan-Boltzmann Law:

$$M_B = \sigma T^4 \tag{2.15}$$

Where σ is the Stefan-Boltzmann constant, equal to

$$\sigma = \frac{2\pi^5 K_B^4}{15c^2h^3} = 5.67 * 10^{-8}\ \frac{W}{m^2K^4} \tag{2.16}$$

It is worth to notice that this law is valid for black bodies. To extend it to grey bodies, M_B must be multiplied for the emissivity of the material considered. The same behavior can be characterized if the object is absorbing radiations. In fact, it is possible to state that for black bodies the coefficient of emissivity is equal to the coefficient of absorption, α_λ. For real bodies, these coefficients essentially depend on the temperature, the surface structure and its characteristics, the wavelength of the radiation and the direction of the radiation, either emitted or absorbed. In order to properly characterize the measurements obtained through an infrared nondestructive method, it is worth to briefly summarize the basics of heat transfer, focusing the attention on what happens in correspondence of anomalies and defects. In general, it is possible to say that heat can be transferred in three ways: conduction, convection and radiation. The thermal flux density Q due to heat conduction between two points at different temperatures T_1 and T_2 is given by the Fourier's law:

$$Q = -\lambda \frac{\delta T}{\delta x} \tag{2.17}$$

Where δx is the differential displacement across the material. Instead, λ is the thermal conduction coefficient, expressed in W/mK. On the other hand, the heat exchange by convection, given by the mass movement of liquid or gas molecules is given by the Newton's law:

$$Q = \alpha_{CV}(T_s - T_{amb}) \tag{2.18}$$

Where T_s and T_{amb} are the temperatures of the object's surface and the ambient surrounding the element respectively and α_{CV} is the coefficient of convection heat exchange. Finally, the heat exchange for radiation between two bodies is expressed by the Stefan-Boltzmann law (Eq. 2.15), expressed as:

$$Q = \sigma \Gamma \varepsilon (T_2^4 - T_1^4) \tag{2.19}$$

Where σ is the Stefan-Boltzmann constant, Γ is a geometric factor and ε is the combination of emissivity of the bodies. When it comes to heat-related anomalies, it is possible to characterize the heat transfer between defects and sound areas considering a combination of conduction, convection and radiation heat exchange. Therefore, the heat transferred by the defect or anomaly is the sum of Eqs. 2.17, 2.18 and 2.19 divided by the thickness of the defect, called d:

$$\begin{aligned} Q_{cd} &= \lambda_d (T_2 - T_1)/d \text{ (conduction)}, \\ Q_{cv} &= \lambda_d^c (T_2 - T_1)/d \text{ (convection)}, \\ Q_{rd} &= \varepsilon\sigma (T_2^4 - T_1^4)/d \text{ (radiation)}, \end{aligned} \tag{2.20}$$

Depending on the type of defect, one source of heat transfer is more relevant than the others. For instance, if the defect thickness d exceeds 5-20 mm, as in honeycomb cells, a significant convection might appear. Provided that, it is possible to say that, a damaged area will be characterized by a higher heat exchange when compared with a sound one. This is to say that, a defect is a region with higher thermal conductivity, therefore, it will appear warmer than the background during the day and colder during the night. To proper characterized different infrared techniques, it is worth to characterize the sensors used for the detection and their characteristics. The detection of infrared radiation is based on two possible measurements; the radiant energy using thermal

sensors or by recording the photon flux by means of photon sensors. In any case, the output is an electrical signal in both cases. The sensitivity of the sensor is defined as the ratio between the output signal to the change in the input signal. In the case of thermal sensors:

$$R = \frac{\Delta U_s}{\Delta \Phi_0}, \tag{2.21}$$

Where $\Delta\Phi_0$ is the change in radiant flux, input signal of the sensor. Another important parameter of a sensor is the temperature or photon resolution. For thermal sensor, the resolution is described by the noise-equivalent temperature difference (NETD) as:

$$NETD = \frac{\Delta T}{\frac{\Delta U_s}{u_R}}, \tag{2.22}$$

Where u_R is the effective noise in the output signal. NETD is the temperature difference that generates a signal to noise ratio equal to one. To be clear, the signal to noise ratio (SNR) is the ratio between the signal power and the noise power, often expressed in Decibels. Another important parameter is the spectral resolution, i.e. the ability to detect certain wavelengths in the electromagnetic spectrum. For instance, photon sensors have a better spectral resolution in the near infrared part of the spectrum. In turns, the spatial resolution is defined as the smallest identifiable target that the detector can measure. A factor affecting this parameter is the dimension of the detector array. Considering thermal cameras, another important parameter to account for is the temporal resolution, i.e. the frequency of image refresh of the camera. For more details about these and other important parameters of a sensor for detecting infrared radiations, readers can refer to an interesting book about remote sensing, wrote by Jensen [84]. In this section, only thermal sensors will be treated since photon sensors are used in sectorized applications, therefore they are outside the scope of this research. In general, part of the radiation energy emitted by an object is acquired by a thermal sensor that through an absorption device, different depending on the type of sensor, is converted into temperature values or maps. This change in temperature ΔT causes a change in an electrical quantity, once again different depending on the type of sensor used. In fact, the change can be in resistance (bolometer), charge (pyroelectric sensor) or voltage and current (thermo-electrical sensor). The thermophysical model of an infrared sensor is represented in Figure 2.31 along with a schematic of the equivalent electric circuit.

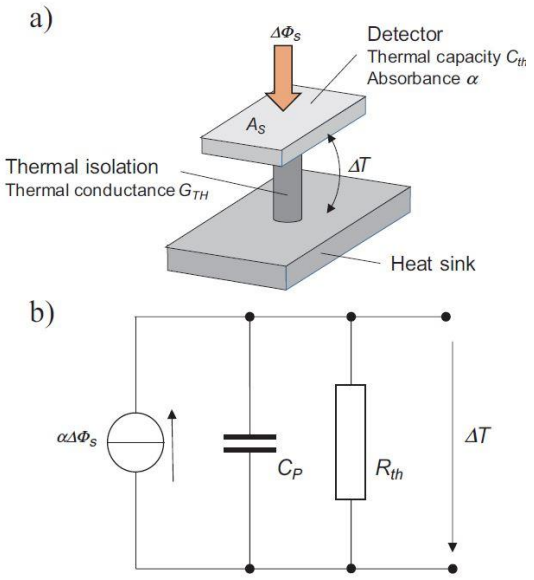

Figure 2.31 Thermophysical model of a thermal sensor

The sensor element is composed by an insulated plate with a certain heat capacity C_P and it's connected to the environment in several different ways, resulting in a conduction coefficient G_{th}. This equivalent and

simplified thermal model allows to calculate the change in temperature of the sensor for harmonic events, related to a certain frequency:

$$|\Delta T| = \frac{\alpha\tau}{G_{th}} \frac{|\Delta\Phi|}{\sqrt{1+\omega^2\tau_{th}^2}}, \tag{2.23}$$

Where the frequency ω represents the modulation frequency of the radiation flux and the thermal constant τ_{th} is given by the ratio among C_P and G_{th}. To achieve high resolution, i.e. greatest temperature difference in the sensor element, both heat capacity C_P and thickness of the element must be as small as possible whereas the thermal resistance, inverse of the conduction coefficient G_{th} must be as great as possible. The first sensor element worth mentioning is the thermocouple. It is based on the Seebeck effect in which a temperature difference in a circuit of conductive or semi conductive material generates a voltage potential. Figure 2.32 shows the schematic of the element.

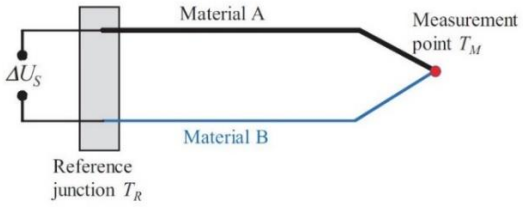

Figure 2.32 Thermocouple schematic

As it is possible to see, there are two different materials, characterized by different electrical properties, often defined as hot and cold junctions. Since the voltage generated by the Seebeck effect is relatively low, often thermocouples are wired in series to increase the voltage content at the output. Basically, the voltage difference ΔU_s is given by:

$$\Delta U_s = N\Delta\alpha_S\Delta T, \tag{2.24}$$

Where N is the number of thermocouples connected in series, $\Delta\alpha_S$ is the difference in Seebeck coefficient of the two different materials and ΔT is the temperature difference at the junction. As it is possible to notice from Eq. 2.24, there is direct proportionality between voltage and number of thermocouples connected in series, therefore the more the thermocouples the better. The second sensor element worth mentioning is the pyroelectric sensor, where the temperature difference is essentially converted in charge Q, whose derivative is the current flowing in the circuit. This type of sensors exploits the so-called pyroelectric effect by which certain materials generate temporary voltage when heated or cooled. Provided that, it is also possible to say that pyroelectric sensors are sensible to variable radiations only, therefore are not suitable for steady state thermal tests. The last type of sensor element worth mentioning is the bolometer. It is a sensor where the temperature difference is directly related to a change of resistance of the sensor's material. It is basically composed by an absorption element, essentially a thin layer of a metal, connected to a body of constant temperature called thermal reservoir. Each time the absorption element is hit by infrared radiation, its temperature changes, and a temperature difference is created with the thermal reservoir. The sensing element in this sensor is a thermistor, placed in between reservoir and absorber, such that the ΔT generates a difference in the resistance of the element. In general, the thermal time constant is given by the ratio of heat capacity of the absorber to the thermal conductance between the latter and the thermal reservoir. The schematics of a simplified bolometer are presented in Figure 2.33.

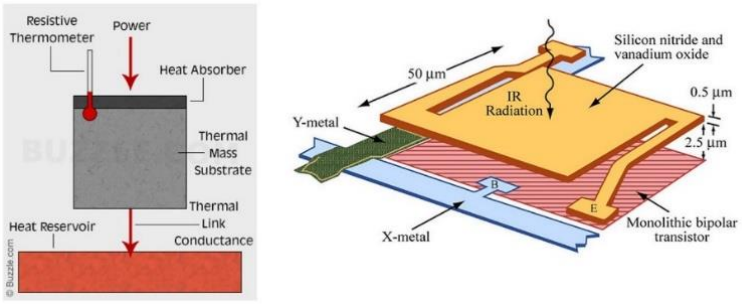

Figure 2.33 Bolometer schematic

For thermal cameras, it is possible to talk about microbolometers. In fact, they work with the same principle of bolometers, but their dimensions are very tiny compared with a classical device. An important advantage of them is that in general they don't require a cooling system. It consists of an array of pixels, each pixel composed by several layers. Between the absorber and the readout circuit, there is a reflector and an insulation layer. In fact, part of the radiation can pass through the absorber, therefore the presence of the reflector enables to redirect the infrared waves towards the absorber without compromising the results. In general, for each pixel the readout circuit is composed by a preamplifier, a multiplexer and the control electronics required for the pixel. In terms of results, the maximum image frequency is basically given by the thermal time constant of the components of the sensor. Figure 2.34 shows the pixel structure of a microbolometer.

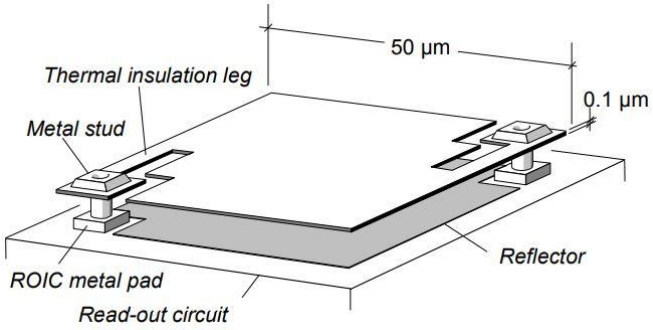

Figure 2.34 Structure of a microbolometer

For a deeper analysis of microbolometers and their possible applications in industry, interested readers should refer to [85], [86]. An important factor to account for is the accuracy of the measure obtained with a thermal sensor. In fact, there are several factors that contribute to distort the outcome of the test. First, it is worth to notice that the measured temperature is not actually the 'real' one, but it is called apparent temperature since the medium between the sensor and the surface inspected tends to alter the measurement. The accuracy of an infrared inspection depends on different parameters such as the emissivity of the object since its value is directly related to the probability of obtaining good results. Another source of uncertainties on the results is related to ambient conditions, so basically the ambient temperature and the possible presence of atmospheric particles. In fact, the environment surrounding the object being tested affects the radiant energy measured by the sensor. For instance, sun radiation for outdoor testing is one of the main reason of uncertainties in the sense that the material tends to absorb radiation energy coming from the sun's electromagnetic waves, altering its natural state. Therefore, often outdoor tests are performed during night to guarantee unbiased results. To tackle the problem of ambient temperature that may produce wrong measurements and drift, often IR equipment embeds an internal compensation system able to correct possible variations coming from external factors.

On the other hand, particles present in atmosphere can attenuate radiation as well as the presence of droplets and dust can cause scattering in the results. Wind effects can compromise results in the sense that high wind content enhances heat transfer as well as it could lead to convective heat losses that can reduce the surface temperature. The last important factors influencing the results of an infrared inspection are the distance of the

sensor from the object and the angle of acquisition. For instance, in the case of thermal cameras, the resolution of the thermogram acquirable decreases as the distance between camera and object increases. The reason behind this is very straight forward, each pixel of the camera is entitled to cover a spatial portion of the surface being tested. If the distance between them increases, the area that a pixel has to cover is larger than before, therefore the resolution of the image is decreased. This distance measure is often called Ground Sampling Distance (GSD).

Finally, the angle of vision of the IR sensor can affect the results. In fact, viewing an object from a very acute angle can generate distortion on the acquisition as well as the material may not be able to emit radiation in the same way in all the directions. It is advisable in this situation to always guarantee a right angle between the surface and the sensor, so that it is possible to acquire more information without distortion. The first important division in infrared testing is between spots measurement and full-field measurements. The former is suitable to detect and measure temperatures of significant and targeted points of a structure and they don't usually provide a lot of information about the conditions of the object being tested, whereas full-field measurements are a reliable and powerful way to assess the overall thermal condition of the element or surface inspected. Equipment useful for spot measurement are infrared thermometers and radiometers. The former exploits thermal radiation to measure the temperature in one point of the structure and usually they are aided by a laser to aim at points of interest with ease.

On the other hand, infrared radiometers measure the radiant flux of electromagnetic radiation without providing information about temperature. Although, knowing the specifications of the sensor, it is possible to indirectly calculated the temperature but in general it is not an automatized procedure. On the other hand, for full-field measurements of temperature, infrared thermography (IRT) is the macro area of interest. IRT is a non-contact, nondestructive technique to inspect structures in real-time and to detect possible surface or sub-surface anomalies. The sensor used for this type of application is a microbolometer, able to reconstruct a thermal image of the element being tested. This image is often called thermogram, showing a thermal map of the structure. It is calibrated to measure the emissivity power of objects. The IR radiation detection gives rise to an electrical response that is converted into visual display in which basically different colors' distributions represent different temperature values. As a rule of thumb, the warmer the object, the brighter it appears on a thermograph. Moreover, in most of the cases thermal cameras are hand-held, therefore dimensions and weight play an important role. Novel thermal imagers embed also a visible camera, usually triggered together with the thermal one, that enables a direct comparison between visible and infrared spectrum. IRT can either be used as a complementary tool for inspection, in order to provide a quick qualitative assessment of material's conditions or it can be used per se to inspect and perform a complete thermal inspection. In the past years, IRT became an important NDT technique because of its possibility to identify an anomaly before it could evolve into a serious problem, allowing to reduce the downtime in case of maintenance and assessment of structures. In general, thermography is affected by a lot of external factors since the incident radiant power absorbed by the sensor element is the sum of the emitted radiant power of the object, the transmitted radiant power of the medium and the reflected radiant power from possible other sources of radiation energy.

The first division in IRT is between active and passive thermography. Basically, in the former heat is directed into the test object in order to detect inhomogeneities and defects, whereas passive thermography is characterized by the measure of heat radiation of objects at their 'normal' temperature state, without including any heat source. Both have advantages and disadvantages; therefore, their usage mainly depends on the type of application. For instance, active thermography can lead to outliers in the results since if the heat is not homogeneously directed towards the source, there could be areas more affected by the radiation source. On the other hand, passive thermography can lead to inaccurate results if the external conditions of the test are not properly considered. For example, the inspection of large infrastructure during summer is not advisable since the presence of high sun radiations would probably distort the results. Going forward, it is worth to mention different active thermography techniques that differentiate each other on the type of input source provided to the object. The main object of heating or cooling an object is to mark the difference in local variations of thermal conductivity and heat capacity in order to isolate and enhance regions within the specimen that behave in a different way

with respect to sound areas. It is possible to have either internal or external heating sources. For the former, the most common ones are induction, microwave or ultrasonic stimulation whereas possible external sources are convection, conduction and radiation of heat towards the object being tested. The principal measurement set-up consists of:

- an energy source that heats the element either periodically, constantly or with a short pulse;
- a thermal imager which measures the surface temperature on a time-triggered basis;
- a control unit to synchronize the measurements;
- a computer to evaluate and post process the results obtained.

Another difference that it is worth mentioning in active thermography is between steady and transient tests. In the former, the test is performed once the temperature of different parts of the object has become constant, to guarantee the proper temperature difference between damaged and sound areas. On the other hand, tests where the heat source is periodically active or is active for a short period of time are called transient. In this case, the objective of the test is to identify temperature gradients of different parts either in the heating or cooling phase. It is possible to obtain results both in time and frequency domains about variations in temperature or temperature differences between different regions of the specimen under analysis. An example of results obtained with transient tests is presented in Figure 2.35.

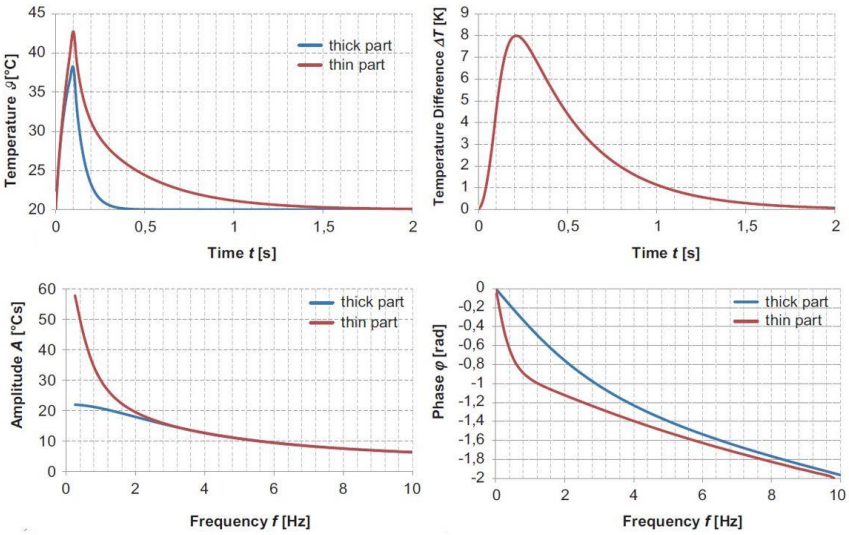

Figure 2.35 Time and frequency domain results of active thermography

Within active thermography, two fundamental applications can be mentioned: pulse thermography and lock-in thermography. In the former the specimen is subjected to a short energy pulse and temperature transients of different parts of the material are evaluated. When the results are expressed considering the frequency domain, often it is possible to talk about pulsed phase thermography. If the pulse last for a considerably long period of time, step thermography is the right name to refer to. On the other hand, lock-in thermography concerns the periodical supplement of thermal energy to the structure at a certain frequency f_{LI}, called lock-in frequency. The result is a series of input pulses, lasting half the period T related to the frequency. If the frequency is changed while executing the test, it is possible to talk about modulated thermography. Comparing it with pulse thermography, it is possible to say that the detection sensitivity is higher when compared with lock-in thermography, but the measuring duration is much longer. Therefore, pulse thermography is a quick test, with a relatively simple measurement setup whereas lock-in thermography is a complex method that requires proper

setup and time to achieve greater results. For what concerns the possible heat sources, Table 2.5 tries to summarize the most relevant ones, according to the position of the source, either external or internal.

Table 2.5 Heat-providing possible sources

External sources	Radiation	Flash and photolamps
		Infrared emitters Halogen lamps Lasers Microwaves Sun
	Convection	Hot or cold air blowers Dries
Internal sources	Thermal conduction	Heating plates Hot or cold water Resistance heating (electrically) Inductive heating Sonic or ultrasonic excitation Chemical reaction Thermoelastic effect Microwaves

For a further analysis about heating sources, interested readers can refer to [87], where the most important ones are explained and optimized for the type of inspection needed. In pulse thermography, the length of the pulse has a relevant impact on the results. In fact, its power spectrum is directly related to the distribution of energy provided to the specimen across the frequency spectrum. In general, a long pulse provides significant energy at low frequencies but very weak energy content at high frequencies, whereas a short pulse is in most of the cases able to energize even high frequencies. This is very important for this typology of tests, since thermal waves penetrating the object have the same frequency spectrum of the pulse emitted. The thermal diffusion length μ is the penetration depth of a thermal wave, for which the amplitude has declined of 1/e:

$$\mu = \sqrt{\frac{\alpha}{\pi f}}, \tag{2.25}$$

Where f is the frequency of the pulse and α is the thermal diffusivity, defined as:

$$\alpha = \frac{\lambda}{\rho C_P}, \tag{2.26}$$

In Eq. 2.26, λ is the thermal conductivity, ρ the density of the material and C_P the specific heat capacity. As it is possible to notice from Eq. 2.25, the depth of penetration decreases as the frequency of the pulse increases. The parameter to detect anomalies is the thermal effusivity, defined as

$$b = \sqrt{\rho \lambda C_P}, \tag{2.27}$$

In general, this parameter is different when comparing sound and damaged areas, since all the coefficients involved in Eq. 2.27 are different in correspondence of a defect. If the value b is lower than that of the surrounding material, the defect will appear as an area of increased temperature. The results are acquired as thermal images over a suitable period. By exploiting common image processing methods, it is possible to evaluate the temperature progression of an image point (pixel) over time. In this scenario, it is worth to briefly mention pulsed phase thermography. In fact, in this method the temperature progression is Fourier transformed, resulting on two plots,

amplitude and phase in the frequency domain. Moreover, by means of the latter it is possible to evaluate the progression over time of temperature changes as well as it basically represents a cross-section through the test specimen. An example of the possible results of this kind of inspection is provided in Figure 2.36.

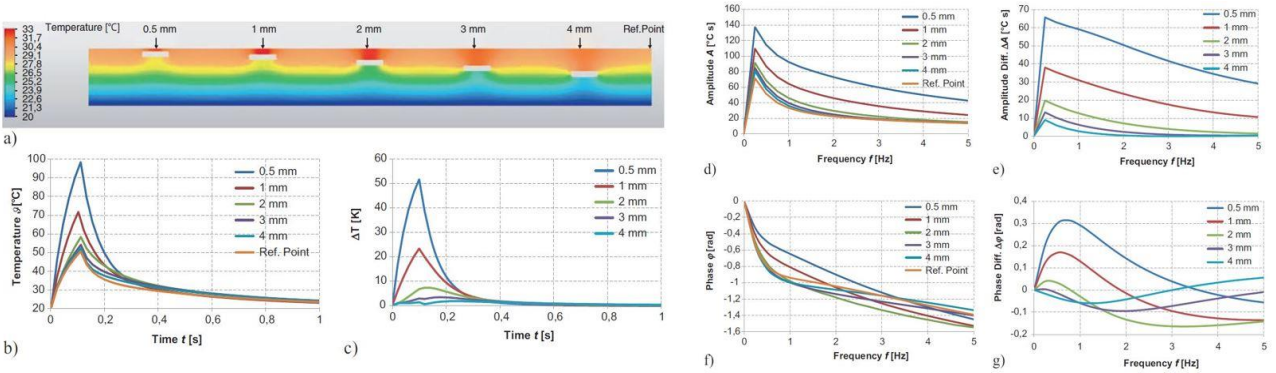

Figure 2.36 Pulse thermography on an aluminum body with cavities at various depths: (a) the temperature distribution 0.2 s after an energy pulse of 0.1 s; (b) the temperature curve at the marked points above the cavities; (c) the temperature differences to a reference point; (d) the amplitude response; (e) the amplitude difference to the reference point; (f) the phase response; (g) the phase difference to the reference point; parameter is the depth z.

On the other hand, if the heat source is provided by means of sinusoidal heat waves rather than pulses, it is possible to talk about lock-in thermography. The amplitude and phase of the object's temperature can be calculated considering four equidistant measuring points, $S_1, \dots, S_4$. The acquisition is performed at different time instants, namely $t_1, t_2 = t_1 + \frac{T}{4}, t_3 = t_1 + \frac{T}{2}, t_4 = t_1 + \frac{3T}{4}$. For a generic pixel n, the amplitude is given by:

$$A(n) = \sqrt{[S_1(n) - S_3(n)]^2 + [S_2(n) - S_4(n)]^2}, \tag{2.28}$$

And the phase by:

$$\varphi(n) = arctan\frac{[S_1(n) - S_3(n)]}{[S_2(n) - S_4(n)]}, \tag{2.29}$$

An example of the method explained so far is present in Figure 2.37.

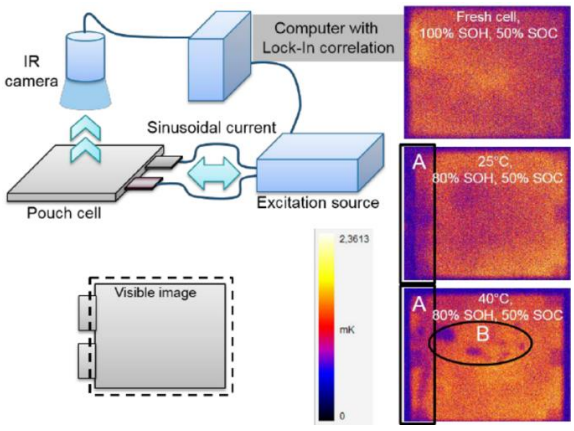

Figure 2.37 Lock-in thermography testing

For a general overview of infrared thermography in structural health monitoring, interested readers can refer to [88], that provides a summary of the methods and possible application of the technique. IRT is employed in a variety of fields including medicine [89], agriculture [90], maintenance (e.g. electrical equipment [91], building diagnostics [92], [93]) and NDT of engineering structures [94]–[96].

2.3 UAV Photogrammetry

Photogrammetry is a three-dimensional coordinate measuring technique able of making reliable measurements starting from photograms or digital photo imagery, used as medium for metrology, in order to locate features on the surface of objects or areas being examined. The outcome is the characterization of the coordinates of a particular point, surface or object in order to reconstruct 3D digital representations of the area under inspection. In the last years, this technique has become a reliable substitute to ground surveying activities, especially when large areas are involved. In fact, photogrammetry allows to conduct terrestrial scanning and topographic mapping in a fast way when compared with ground-like surveys, allowing to scan more rapidly large areas, often obtaining better results. The purpose of this technique can be ortho rectified imagery, digital terrain models or 3D points clouds that can be used for a broad variety of engineering tasks. The relevant advantages of this technique when compared with ground surveys are:

- it provides a permanent record of the area being tested as it appeared at the time the photographs were taken;
- mapping features and data can be extracted from stereo vision models;
- fastness when inspecting large areas, reducing the overall surveys' costs;
- photogrammetry can be successfully implemented in environments that are difficult to access from the ground;
- re-evaluation of data is very easy and straightforward and there is no need to reconduct the entire survey.

On the other hand, photogrammetry is not always the best inspection method to use. In fact, it does not perform well in those scenarios characterized by dark shadows, or dense vegetation or overhanging features. Moreover, weather conditions play an important role in the obtainable accuracy of the test. In fact, high windy and cloudy environments may hamper the performance of the mission, as well as sun conditions that can create long shadows or produce spots on the image. Figure 2.38 provides an example of possible outcome of a photogrammetric ortho rectified survey.

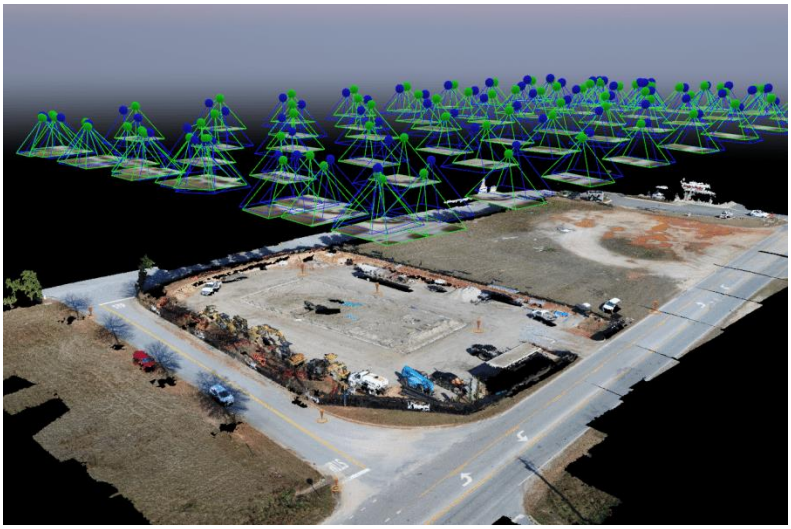

Figure 2.38 Example of photogrammetric survey

As it is possible to notice from Figure 2.38, by exploiting photogrammetric acquisition and by implementing stereo vision models and triangulation techniques, it is possible to reconstruct a digital 3D model of the scene under inspection. Prior to the definition of mission planning and flight path, it is important to remark which is the relationship between a point in the 2D plane of the image and the 3D point on the scene. This is the basis of photogrammetry, as well as it is the starting point for the bundle adjustment method that will be explained in the following section, in the context of structure from motion. The first fundamental thing to do is to reference the image plane and the scene space by means of suitable coordinate systems. Basically, there are two mathematical models to describe this relationship, the collinearity model and the 7-parameters transformation, that allow to relate coordinates in the sensor plane with coordinates in the 3D object space. In this section, the former model will be carefully explained whereas the latter will be introduced in the following section, in the context of computer vision.

First, it is important to understand how the interior orientation of a camera can be expressed in terms of coordinates. The purpose is to define a relationship between the photo-coordinate system and the measuring coordinate system. Indeed, it is not possible to directly measure photo-coordinates. The final outcome is the definition of some characteristic parameters, often called camera intrinsic parameters with which it is possible to define the calibration matrix, useful in the phase of calibration, before the actual acquisition phase. The mathematical model behind this part related to the internal orientation will be also tackled in the following section in order to give a certain consistency with the process of definition of images. Provided that, the remaining part is related to the exterior orientation, that is the relationship between image and object space. Basically, the aim is the definition of the camera's position in the 3D scene coordinate system. This is defined by the location of the image center in space, also called perspective center, and three angles, defining the attitude of the image. To better understand this concept, Figure 2.39 presents a schematic of the collinear model.

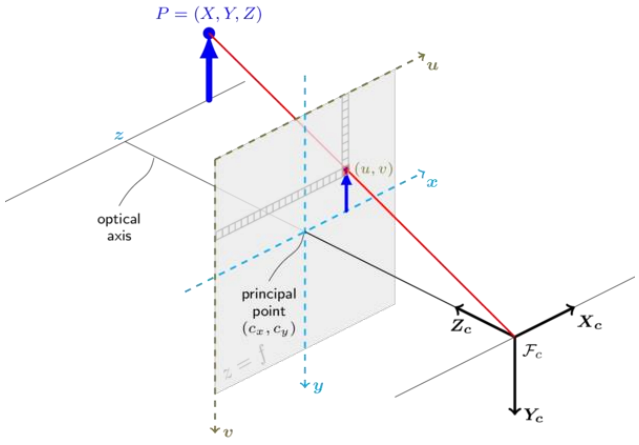

Figure 2.39 Example of camera model. Red ray representing collinearity model

In this regard, the collinearity model comes in handy since it expresses the condition that the object point $P_o = (x_p, y_p, z_p)$, the perspective center $C = (x_0, y_0, z_0)$ and the image point $P_i = (x, y)$ must lie on a straight line. The relationship is based on a fixed ratio, λ, that relates all the three set of coordinates and it is justified by the definition of collinearity. Namely, it is possible to write that

$$x - x_0 = -\lambda(x_0 - x_P), \tag{2.30}$$

$$y - y_0 = -\lambda(y_0 - y_P), \tag{2.31}$$

$$c = \lambda(z_P - z_0), \tag{2.32}$$

Provided that, it is possible to solve Eq. 2.32 in λ, to obtain a preliminary result of the collinearity model. By doing that, it yields to

$$x - x_0 = -c\frac{(x_P - x_0)}{(z_P - z_0)}, \tag{2.33}$$

$$y - y_0 = -c\frac{(y_P - y_0)}{(z_P - z_0)}, \tag{2.34}$$

It is worth to mention that Eqs. 2.30 to 2.32 are sufficient to calculate 3 out of 6 extrinsic parameters of the camera, the perspective center coordinates. This is possible if the coordinates of the 3D point P are known a priori. In general, this is achieved considering some ground control points (GCPs) in the scene, for which the location has been measured externally by means of ground control stations. If the exterior orientation is known, the relationship between an image vector P_i and the vector Q_o in the object space is given by

$$P_i = \frac{1}{\lambda}Q_o, \tag{2.35}$$

Where Q_o is given by the difference between the point vector of the perspective center, C and the object point P_o. At this point, it is worth to say that coordinates of the objects are given in the world reference frame, therefore it is necessary to transform them in order to be complaint with the coordinate system of the camera. To do that, a rotation matrix and a translation vector must be added. Although, the translation can be also neglected since its contribution vanishes when working with differences of coordinates, like in this case. For a better understanding about object space and image space, Figure 2.39 presents a schematic of the two reference systems.

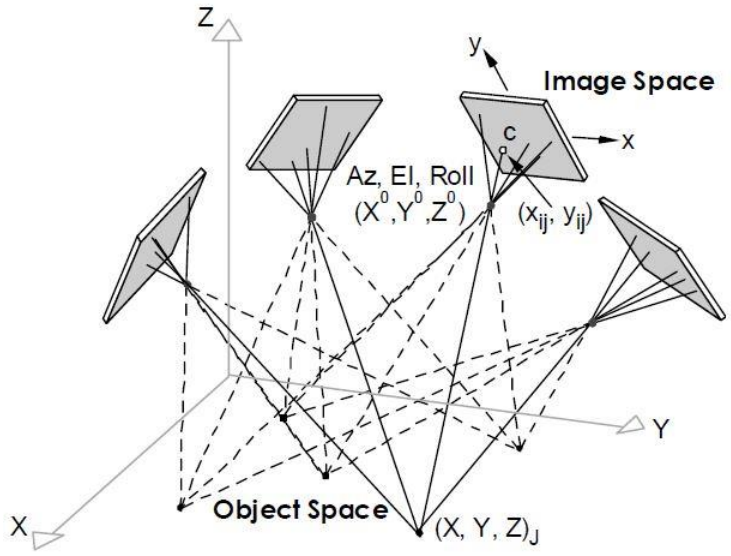

Figure 2.40 Difference between image space and object space

The last step for the definition of the collinearity equations is the addition of the rotational contributions given by the rotation matrix R. In a compact form, it is possible to obtain

$$P_i = \frac{1}{\lambda}\boldsymbol{R}Q_o = \frac{1}{\lambda}\boldsymbol{R}(P_o - C), \tag{2.36}$$

Eq 2.36 can be expressed by means of axial coordinates rather than vectors, therefore leading to

$$x = \frac{1}{\lambda}(x_P - x_0)r_{11} + (y_P - y_0)r_{12} + (z_P - z_0)r_{13}, \tag{2.37}$$

$$y = \frac{1}{\lambda}(x_P - x_0)r_{21} + (y_P - y_0)r_{22} + (z_P - z_0)r_{23}, \tag{2.38}$$

$$-c = \frac{1}{\lambda}(x_P - x_0)r_{31} + (y_P - y_0)r_{32} + (z_P - z_0)r_{33}, \tag{2.39}$$

Equivalent to Eqs. 2.30 to 2.32 not considering the rotation terms. As before, by dividing Eqs. 2.37 and 2.38 for the last equation it is possible to obtain the collinearity equations, that can be used to calculate the exterior orientation of the camera. Thus, it is possible to obtain

$$x = -c\frac{(x_P - x_0)r_{11} + (y_P - y_0)r_{12} + (z_P - z_0)r_{13}}{(x_P - x_0)r_{31} + (y_P - y_0)r_{32} + (z_P - z_0)r_{33}}, \tag{2.40}$$

$$y = -c\frac{(x_P - x_0)r_{21} + (y_P - y_0)r_{22} + (z_P - z_0)r_{23}}{(x_P - x_0)r_{31} + (y_P - y_0)r_{32} + (z_P - z_0)r_{33}}, \tag{2.41}$$

Namely, the six unknown parameters are x_0, y_0, z_0 and the three angles of the rotation matrix. It is worth to say that each object point adds two equations that can be useful to determine such parameters, but it also adds 3 unknowns, its coordinates. If the location is known a priori, such in GCPs, the problem admits a unique solution. If this is not the case, more than one photogram that relates to the same point is needed to compute the camera's extrinsic parameters.

Provided an overview about the fundamental principle behind photogrammetry, it is worth to present other relevant steps that defines a photogrammetric inspection. First, an adequate path and mission planning must be provided to guarantee reliable and accurate results. In this scenario, the platform to acquire digital photograms is an Unmanned aerial vehicle (UAV). According to UVS International, a UAV is a generic aircraft designed to operate with no human pilot onboard. In the past, manned systems were widely implemented in photogrammetry since the purpose of UAV was basically for military applications. Instead, in the last decades, the usage of UAV in the geomatic field has become pretty common. Depending on weight, size, range, endurance and flying altitude, UVS International defines three mains categories of unmanned aerial platforms:

- *tactical UAVs*, characterized by a mass range from few kilograms up to 1000 kg, there is no constraint on the size, the range from few km up to 500 km, a flight altitude from few hundred meters up to 5 km and an endurance that can span from some minutes to 2-3 days;

- *strategical UAVs*, that include long endurance stratospheric and exo-stratospheric systems which can fly higher than 20000 m and an endurance of 2-4 days on average;

- *special tasks UAVs*, such as lethal and decoys systems or combat autonomous vehicles.

All these three categories have in common the airframe that is in general composed by either rotary or fixed wings. Instead, the take-off methods are very different depending on the type of application considered, including autonomous mode, hand launched, bungee cord lunched, etc. Provided that, UAV photogrammetry opens to a wide variety of applications and introduces a low-cost alternative to manned aerial photogrammetry [97], [98]. The development of this technique can be attributed to the spread of cheap platforms combined with digital cameras as payload. Moreover, the presence of GNSS and IMU systems in the UAV, enables to navigate it with

high precision to the predefined acquisition points. GNSS stands for Global Navigation Satellite System and it provides autonomous geo-spatial positioning with global coverage. It has access to multiple satellites at the same time therefore it is able to always guarantee accuracy, redundancy and availability. On the other hand, an Inertial measurement unit (IMU) is an electronic device that usually embeds an accelerometer and a gyroscope, in order to measure the orientation of the body, the angular rate and the force. This is very helpful for control purposes since the knowledge of the attitude of the UAV can help control its path as well as guarantee stability in harsh weather conditions. According to the work of Remondino et al in [99], the typical fields in which UAVs and photogrammetry are employed are:

- *forestry and agriculture*: producers can take reliable decisions to save money and time, get quick and accurate record of damages or identify potential problems in the field. Assessments of woodlots, fires surveillance, species identification, volume computation as well as silviculture can also be accurately performed ([100]; [101]);

- *3D reconstruction*: unmanned aerial vehicles are a valuable source of image data for general 3D reconstruction purposes of engineering structures [102], [103];

- *traffic monitoring*: surveillance, travel time estimation, trajectories, lane occupancies and incidence response are the most required information ([104]; [105]).

Once introduced a description of photogrammetry, including the usage of different platforms and explaining the relevant applications of it, it is worth to briefly summaries the steps to set up a photogrammetric survey. Once identified the project and the purpose of the survey, flight planning or mission planning is the first step to consider. In this task, the purpose is to provide an adequate photo coverage to guarantee a satisfactory survey. First, the area of interest (AOI) must be identified, as well as the required ground sampling distance (GSD). In photogrammetry, GSD is the distance between two consecutive pixels' centers measured on the ground. It is a very important parameter since it identifies the spatial resolution of the digital reconstruction of the survey. In fact, the bigger this value, the lower will be the spatial resolution. Another factor influencing its value is the flight height, characterized by an inversely proportional relationship with the GSD. In general, there are calculators and software able to combine together all this information and provide the best trade-off between accuracy and computational effort of the reconstruction. Table 2.6 provides an adequate combination of the aforementioned parameters for different project types.

Table 2.6 Image coverage (source: Photogrammetric surveys [106])

Project type	Flight height [m]	Pixel resolution [cm/pixel]	Ground coverage along flight line	
			Length [m]	Width [m]
Urban projects (plains)	380	3.81	293	527
Urban projects (mountains)	457	4.57	351	632
Suburban projects	549	5.49	421	758
Rural projects (plains)	610	6.10	468	843
Rural projects (mountains)	732	7.32	562	1011
Systems	2156	21.56	1656	2981
High altitude city planning	2896	28.96	2224	4002

Once defined the purpose of the project and the relevant parameters for flight planning, an important step is the definition of the targets of the inspection. In fact, it is possible to use a different variety of software to acquire geolocations of those components and set-up an adequate flight path for the survey. The latter can either manual, where the pilot controls the UAV by using a remote controller or automatized, meaning that the UAV will follow a precise path given by a set of coordinates provided before the actual test. By means of a mission planning software it is possible to plan the flight considering different aspects such as terrain elevation, ground flight height, flight line trigger limit and exposure overlap. In practice, the targets' locations are also called waypoints, defining the path to follow. Once the flight path has been assigned, it is possible to import the data and specifications of it into the unmanned aerial platform. During flight, the UAV is observed with a control station which shows real-time data, such as battery status, attitude, speed, height and distances. In more recent applications it is also possible to have proximity sensors that prevent possible damages or incidents and stability devices to mitigate the effect of external factors.

The second important step for a successful photogrammetric survey is the evaluation of the external conditions, namely weather conditions. In fact, a good consideration of them allows to guarantee safety conditions when performing the test, without damaging the UAV platform and at the same time it allows to acquire better photograms that are not affected by possible distortions. For instance, the sun's direction and angle above the horizon are critical parameters for a good inspection. A suitable sun angle is between 30° and 45°. In fact, it minimizes the effect of long shadows as well as provides sufficient reflective light. Moreover, it guarantees the elimination of possible shadows and hot spots created by the aircraft. In this scenario, it is possible to define the so-called "windows of opportunity" in which the best external conditions can be achieved. During winter months, the acceptable light angle is available for few hours during midday while during the summer there are two different spots, in the morning and in the afternoon. More in general, the best period to perform such inspections is during early spring, that provides a suitable trade-off in terms of external conditions. Once the best external set-up has been found, the following step is the choice of the degree of overlap of the images. In fact, an aerial photography is never a single shot event. For adequate digital reconstruction, multiple photographs are taken along the flight path, to ensure complete photo coverage of an area. For reconstruction purposes, it is required a frontal overlap of at least 70% and lateral one of 60% in the visible spectrum. If the survey is carried out in the infrared spectrum, the overlap must be higher in order to compensate for the lower resolution of the cameras. An example of flight planning is shown in Figure 2.41.

Figure 2.41 Flight path planning

Once defined all the relevant parameters and tasks of the platform used, some time must be spent in the proper set-up of the acquisition system. Depending on the size of the UAV, different cameras' payloads can be used. The state of the art towards this direction is a gimbal support embedded in the aerial vehicle that enables the attachment of payloads in an easy way and allows to remotely control the orientation of the camera. This system allows to stabilize the payload regardless to the movements of the UAV. Most of the time, it is possible to pan, tilt and pitch the camera in order to guarantee a customization of the acquisitions. This can either be done manually or remotely by means of the same controller that is used to navigate the UAV. The next step is the calibration of the camera used. This is a fundamental task to guarantee accurate and reliable results therefore many different techniques can be used. Hence, the precise knowledge of camera's intrinsic and extrinsic parameters can play an important role for the digital reconstruction. More details about this step will be provided in the following section where computer vision and image processing techniques will be tackled. The last step after the acquisition is the surface reconstruction and feature extraction. By means of them and knowing the camera calibration parameters, it is possible to digitally reconstruct a scene by means of automated dense image matching techniques or interactive methods for features and vector information extraction. To do that, there are a wide variety of methods including multi-image matching [107], semi-global matching [108], bundle adjustment methods [109] and structure from motion approaches [110]. This part of photogrammetry is very wide and requires the knowledge of the basic principles of computer vision, therefore it will be better explained in the following section, after providing an overview of image processing techniques. For a more detailed analysis about photogrammetry interested readers can refer to [111], [112] that provide a wide explanation of the subject that is beyond the scope of the research. The following section will be dedicated to computer vision and structure from motion, trying to continue the path started with this section.

2.4 Computer Vision & Structure from Motion

This section is related to the topic of computer vision, going in details about structure from motion (SfM) and the most relevant image processing techniques. Computer vision is a scientific field which aims to enhance the understanding of a computer regarding images and videos. Basically, the goal is to make computers more aware about information and data extrapolated from digital images or footages. The final goal would be to make computers skills comparable to that of a human being in terms of understanding of external environments. To achieve that, a lot of different techniques can be exploited to acquire, process and analyze data coming from digital images. The state of the art in this direction is artificial intelligence, machine learning and deep learning as well as image processing techniques that enable a computer to make critical decisions, as well as a human being does. In general, this task is very difficult to achieve since it is an inverse problem in the sense that starting from a result, digital image, a computer has to recover unknowns' parameters with insufficient information. Most of the time, these parameters are not objective but rather subjective therefore the task of computer vision is very challenging. Hence, to find approximative and potential solutions, computer vision exploits probabilistic and physics-based models that are able to provide a solution that is acceptable even though it would never be close to the real-world complexity of the problem. Furthermore, there are cases in which even human beings are tricked by optical illusions. For instance, Figure 2.42 presents some of the most famous optical illusions.

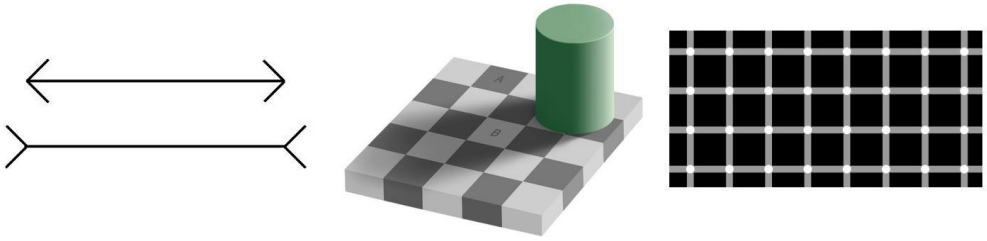

Figure 2.42 Common optical illusions.

The optical illusion on the left of Figure 2.42 is known as Muller-Lyer illusion, where the length of the horizontal lines appears different even though the segment length is the same. The central one is the Edward Adelson illusion for which the shadowed square B and the 'black' square A have the same intensity values, but they seem completely different. This is due to the so-called brightness constancy, for which the visual system attempts to discount illumination when interpreting different colors. Instead, the last one on the right is the Hermann grid illusion, whereby moving your eyes over the image, grey spots tend to appear at the intersections. This is to say that sometimes images' interpretation is difficult for humans but not for computer since they are not affected by impressions and illusion. Nowadays, this field of study is implemented in a variety of different applications such as medical imaging, automotive safety, motion capture, 3D rendering of building, surveillance, object recognition and biometrics, etc. First, it is worth to understand how an image is created and how a three-dimensional scene can be represented in a 2D plane. There are different ways to project a 3D point into a 2D plane. The most relevant ones are orthography, para-perspective and perspective transformations. Figure 2.43 shows a possible projection of a scene into a 2D image.

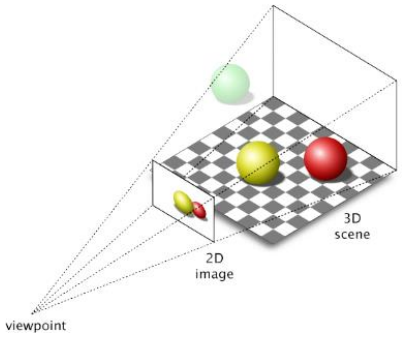

Figure 2.43 3D-2D transformations

Given a point $p = (x, y, z)$, an orthographic projection simply drops the z component of such point. It is possible to write that in matrix form as follows:

$$p_{2D} = [I_{2x2}|\mathbf{0}]p, \tag{2.30}$$

Where the matrix between squared brackets is a 2x3 matrix where I_{2x2} is a 2x2 identity matrix and $\mathbf{0}$ is a 2x1 vector of zeros. In homogeneous coordinates it would be:

$$\widetilde{p_{2D}} = \begin{bmatrix} 1 & 0 & 0 & 0 \\ 0 & 1 & 0 & 0 \\ 0 & 0 & 0 & 1 \end{bmatrix} \widetilde{p}, \tag{2.31}$$

Orthography represents an approximate model for long focal length objects and lenses where the object depth is shallow compared to the distance from the camera. A configuration often used is called scaled orthography where, world coordinates are scaled to fit into the image sensor. This is easily achieved by multiplying the identity matrix in Eq. 2.30 for a scaling factor s, that can map real dimensions to pixels. A similar projection model is called para-perspective, where the object points are first projected into a local reference frame parallel to the image plane and then scaled. The main difference between this technique and orthography is that in this case 3D points are not orthogonally projected, but they are projected parallel to the line of sight of the object center. The combination of parallel transformation and scaling defines an affine transformation that can be written as:

$$\widetilde{p_{2D}} = \begin{bmatrix} a_{00} & a_{01} & a_{02} & a_{03} \\ a_{10} & a_{11} & a_{12} & a_{13} \\ 0 & 0 & 0 & 1 \end{bmatrix} \widetilde{p}, \tag{2.32}$$

Where a_{ij} are the coordinates of the affine transformation. For sake of clarity, an affine transformation is a transformation that preserves lines and parallelism. Para-perspective is in general more accurate than scaled orthography. The most used projection technique is called perspective transformation. In this scenario, 3D points are mapped into the camera plane, dividing their coordinates by the z component. Therefore, it is possible to obtain the following formulation:

$$\widetilde{p_{2D}} = \begin{bmatrix} x/z \\ y/z \\ 1 \end{bmatrix}, \tag{2.33}$$

Hence, after the projection, it is no more possible to reconstruct the depth of the scene since the z component is no longer available. By means of this transformation, distant objects on the scene appear smaller than nearer objects. Figure 2.44 summarizes the projection techniques explained so far.

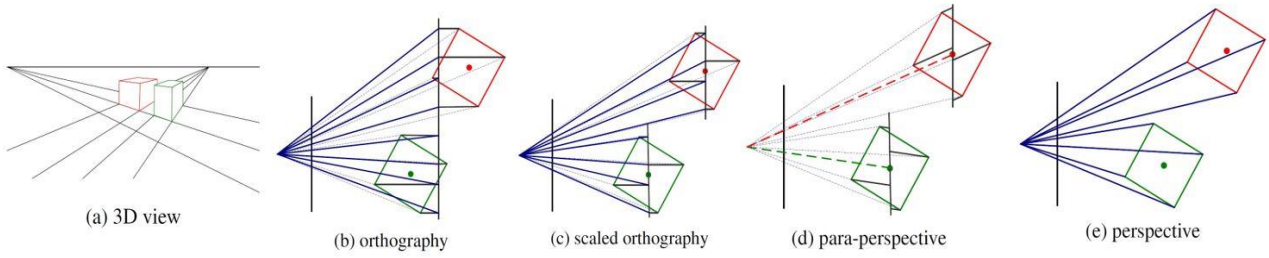

Figure 2.44 Projection techniques

Once the 3D point has been project in a 2D plane, the resulting coordinates must be transformed according to the image sensor. To do that, it is necessary to exploit camera intrinsic parameters. In fact, image sensors return pixel values indexed by pixel coordinates, integer values, often starting from the upper-left corner of the image. To map pixel centers to 3D coordinates, first it is required to scale the pixel coordinates values by the pixel spacings (s_x, s_y) and then characterize the sensor array relative to the camera projection center O_c with origin c_s and 3D rotation R_s. The combined transformation is the following:

$$p = [\, R_s \mid c_s \,] \begin{bmatrix} s_x & 0 & 0 \\ 0 & s_y & 0 \\ 0 & 0 & 0 \\ 0 & 0 & 1 \end{bmatrix} \begin{bmatrix} x_s \\ y_s \\ 1 \end{bmatrix} = M_s p_{2D}, \tag{2.34}$$

Where M_s is called homography and it is a 3x3 matrix in which the first two columns are 3D vectors corresponding to unit steps in the image pixel array along the x_s and y_s directions, whereas the third column is a 3D image translation with respect to the origin c_s. From a theoretical point of view, the matrix M_s is parametrized by eight unknowns: three parameters describing the rotation matrix R_s, three parameters describing the translation c_s and two scale factors (s_x, s_y). In practice, only seven of them are available since it is very difficult to have knowledge of the distance of the sensor from the origin just having the sensor spacing. Figure 2.45 tries to explain graphically the transformations performed so far.

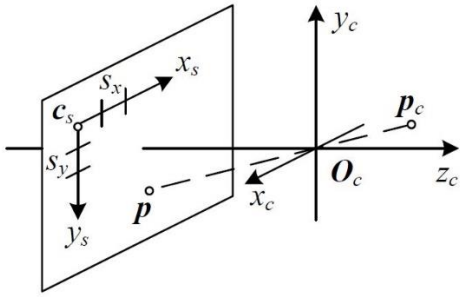

Figure 2.45 3D scene image plane transformation

Figure 2.43 represents the projection of a 3D camera-centered point p_c into the sensor plane at location p. O_c is the camera center and c_s is the origin of the sensor plane coordinate system. Therefore, the relationship between a 3D pixel center p and a 3D camera-centered point p_c is given by an unknown scaling factor s. The complete projection, starting from the 3D point up to the 2D coordinates of the point in the sensor plane is given by:

$$p_{2D} = \begin{bmatrix} x_{ps} \\ y_{ps} \end{bmatrix} = \alpha M_s^{-1} p_c = K p_c, \tag{2.35}$$

Where α is an unknown parameter and K is called calibration matrix and describes the camera intrinsics parameters. On the other hand, camera extrinsics parameters are those parameters referred to the orientation of the camera in the 3D space. In real life application, camera intrinsics and extrinsics parameters are estimated or computed simultaneously, by means of the following relationship:

$$p_{2D} = K\, [R \mid t]\, p = P p, \tag{2.36}$$

Where P is a 3x4 matrix, usually called camera matrix, summarizing intrinsic and extrinsic parameters of it. Several simplifications and assumptions can be done in this matrix depending on the type of application and the accuracy required in the results. Other two parameters important for a camera model are the focal length f and the aspect ratio a. The former is defined as the distance of the camera lenses to its focal point. In other words, it is the distance at which the camera is in focus. On the other hand, the aspect ratio is simply the ratio between the width and the height of an image. It is usually expressed by two numbers, divided by a colon (e.g. 16:9, 4:3, etc.). They are dependent to each other and are in general present in the calibration matrix K. In the camera models discussed so far, the hypothesis is that the projection model is linear but in real cases lens distortions must be considered. Depending on the type of lenses, it is possible to have a different amount of radial distortion that manifests itself as a curvature in the projection of straight lines. Fortunately, there are several models that can represent with adequate accuracy the distortion of the lenses. They are represented by functions of polynomials, often a quartic function, in which some radial distortion parameters are considered. Figure 2.46 shows the most relevant types of lenses distortions.

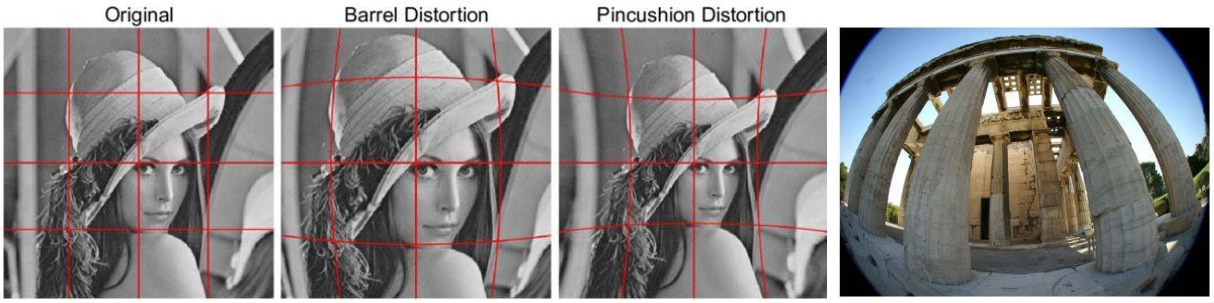

Figure 2.46 Different types of lens distortions

Once defined the geometrical properties to create an image, it is worth to mention also the process of image formation. In fact, an image is just a collection of intensity values grouped in a three-channels tensor, where each channel represents one fundamental color, i.e. red, green and blue. To create an image, the scene must be illuminated by a source of light. This can be either a point or an area source and it is characterized by an intensity and a color spectrum, i.e. a distribution of different electromagnetic waves. Figure 2.47 reports a schematic of the influence of a lighting source in the process of image formation.

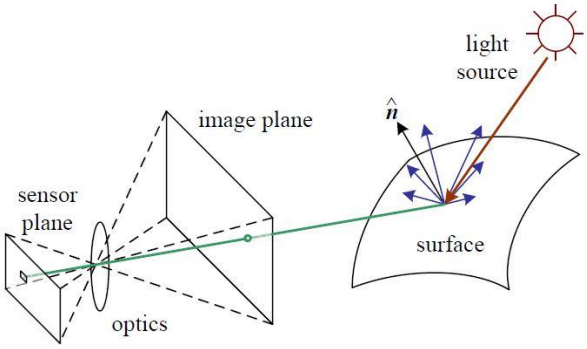

Figure 2.47 Process of image formation

In Figure 2.47 it is possible to see a simplified model of photometric image formation. Light is emitted by a source and reflected by the object in the scene. A portion of the reflections falls in the direction of the camera, that can reconstruct the scene in a digital image. Depending on the relative position of the camera with respect to the scene and considering multiple reflections and possible shading, it is possible to obtain very different representations of the same scene. The part of the light directed towards the camera has to pass towards the lens before reaching the sensing element. In most of the simplified cases, it is sufficient to treat the lens with the so-called pinhole model, considering that all the light rays pass into an ideal hole. In practice, very complex lens models can be applied, depending on how much accuracy is required for the analysis. The most basic lens model is the *thin lens* model in which the lens is a single piece of glass with very low curvature on both sides. Figure 2.48 shows a sketch of this simplified model, along with the perception of the scene in the image, an arrow in this case.

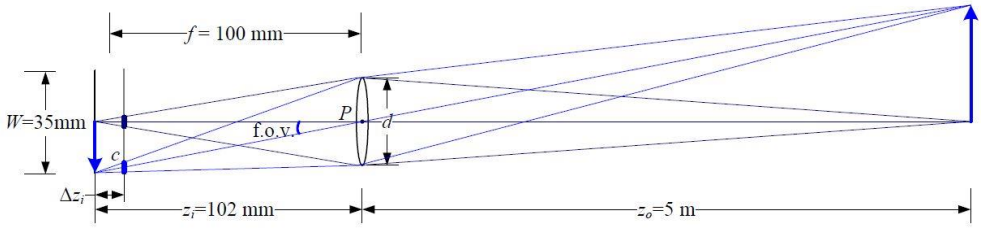

Figure 2.48 Thin lens model

The lens focuses the light from a plane at distance z_0 into a plane at distance z_1 behind the lens. If the lens is moved forward, the image is no more focused, and it is possible to experience blurring in the image. Another important parameter is the field of view (FOV) defined as the solid angle through which the sensing element of the camera is sensitive to electromagnetic radiations. In general, it is dependent on the ratio between the sensor width W and the focal length f. The relationship between the distance to an object and the distance among lens and sensing element at which the scene is focused is also called *lens law* and it is defined as:

$$\frac{1}{z_0}+\frac{1}{z_i}=\frac{1}{f}, \tag{2.37}$$

If $z_0 \to \infty$, and the lens is adjusted in a way that objects at infinite distance are in focus, $z_i = f$ and this is why it is possible to characterize a lens with focal length f as a pinhole at distance f from the sensing element of the camera. However, it is possible to vary the distance between sensing element and lens, within a certain limit, defining the so-called depth of field of the scene. Different other factors influence the formation of an image, but a detailed discussion is beyond the scope of this theoretical review. Figure 2.49 describes the usual pipeline of image sensing, starting from the absorption of radiant energy, up to the conversion in a digital file.

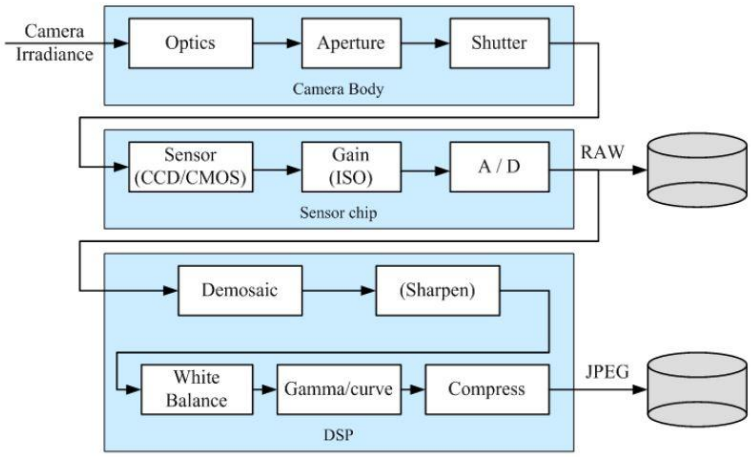

Figure 2.49 Image formation pipeline in a digital camera

Once the process of formation of an image has been tackled, the next step is to start looking at the first step in computer vision: image processing. In fact, most of the time this is a fundamental step to guarantee accurate results in different applications. The first category of image processing techniques is called point process. In this, each output pixel value only depends on the corresponding input pixel value. A generic image processing operator is a function that takes one or multiple input images and produces an output image. By denoting pixels locations as $x = (i, j)$, this operation can be represented by:

$$g(x) = h\big(f(x)\big), \tag{2.38}$$

Where the function $g(x)$ represents the output image, $f(x)$ the input image and $h(\cdot)$ is the operator. This operator can be of different kinds depending on the purpose of the processing. Two common operators are multiplication and addition with a constant, that can be represented as:

$$g(x) = af(x) + b, \tag{2.39}$$

Where $a > 0$ and b are often called gain and bias of the operation. They are basically placed to control contrast and brightness respectively. They can also be variable rather than constant, depending on the location within the image, i.e. being function of $x = (i, j)$. They are both linear operators and are the basics of image processing techniques. Another commonly used function is the linear blend operator, that is used to perform a temporal fade between images or videos. The final output is given by

$$g(x) = (1 - \alpha)f_0 + \alpha f_1(x), \tag{2.40}$$

Where α is a parameter spanning from 0 to 1 depending on how much cross-dissolve is needed. Rather than work with pixels, it is also possible to operate directly on colors, obtaining results that affect the entire image rather than just pixels. The first technique worth mentioning is called matting, where basically first a division of background and foreground is done, and then the background is cut off the scene and possibly replaced with another one. For the last process, the usual name is compositing. The intermediate stage in which the foreground is isolated is often called α-matted color image, that describes the relative amount of opacity at each pixel. This channel is in addition to the three color RGB channels already present. Pixels fully outside the foreground are transparent ($\alpha = 0$), whereas pixels within it are fully opaque (α =1), meaning that they are represented in white while the previous ones are black. Pixels on the edges of the foreground have different α values depending on the location and the shape of the object represented. Figure 2.50 highlights the process of matting starting from a normal image.

Figure 2.50 Matting example where the image in the center is used to facilitate the algorithm

As you can see from Figure 2.50, the overall result is just an image containing the foreground highlighted. The next step is to compose the obtained foreground with a background. The operator used for this operation is called "over" operator and the final image C is given by

$$C = (1 - \alpha)B + \alpha F, \tag{2.41}$$

Where B and F are the background and foreground images respectively. Basically, the operator attenuates the influence of the background by a factor $(1 - \alpha)$ while adding the foreground in a quantity proportional to α. An example of the overall result of the procedure is represented in Figure 2.51.

Figure 2.51 Matting and compositing result

In some situations, it is convenient to work directly with the αF image rather than multiplying pixels values in the over operation. In fact, it is easier to do basic operations such as blurring or rotate the image directly having the final representation of the foreground. The over operator is not the only one used for compositing, but its fastness and reliability made it one of the most common used. Another important operation rather than operator often used to characterize the image is the histogram equalization. First, it is possible to extract important values such as maximum, minimum and average intensity of the image, and then have an intensity distribution to manipulate to obtain a better-looking output image. The first step is to compute a cumulative distribution function (CDF) starting from image intensity values. Given a random variable x, the CDF of x in a generic point y, is the probability that x will take a value less or equal to y. In continuous

distribution, the CDF of x gives the area under the probability density function from -∞ to y. Therefore, in the case of images, the CDF represents the discrete integral of the original histogram $h(i)$ of the image, defined as

$$c(j) = \frac{1}{N}\sum_{i=0}^{j} h(i) = c(j-1) + \frac{1}{N}h(j), \tag{2.42}$$

Where N is the number of pixels in the image. The CDF for one-pixel j is also called percentile. For any intensity value, by looking at the value of $c(j)$ it is possible to determine the final value that the pixel should take to properly equalize the histogram. Sometimes, it is preferable to apply different types of equalization in different regions of the image. In this case, it is possible to talk about local adaptive histogram equalization. Instead of computing a unique probability distribution function for the whole image, it is possible to perform locally the equalization by dividing the image in blocks of pixels. To avoid discontinuities between blocks, often a moving window is used in order to smooth the effect of equalizing each block per se. The drawback of using this approach is the computational time since the blocks are partially overlapped and the calculous for one pixel might be done more than once. There is another way that can potentially reduce the computational time and it is to use non-overlapped blocks and then interpolate the functions of each block when moving in between blocks. There are several different types of equalization of an image and all of them are based on the computation of the CDF and the probability density function (PDF). Figure 2.52 shows an example of equalization of an image.

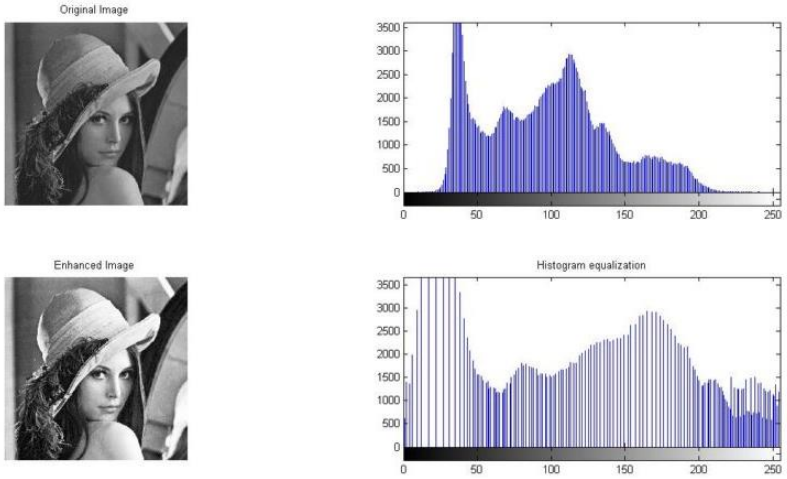

Figure 2.52 Histogram equalization

As it is possible to notice, the output image after equalization has enhanced details and it is less affected by shadows and contrast problems. The case of locally adaptive histogram equalization is a case of neighborhood operator in the sense that the final value of intensity of a pixel depends not only on its initial value but also on its neighbors. This is also the case of another category of operators, the so-called filtering operators. Sometimes, it is important to filter an image in order to sharpen, blur, enhance edges or remove noise from an image. This can be done by linear or non-linear operators and the process is based on the combination of different weights attributed to each pixel within a certain block, often called kernel. The linear filter is an operator for which the output pixel's value is given by a weighted sum of input pixels values. The intensity is given by

$$g(i,j) = \sum_{k.l} f(i+k, j+l)h(k,l) \tag{2.43}$$

Where k and l are the size of the kernel used and i,j the location of the pixel involved. Instead, $h(k,l)$ is the filter mask. The entries in this mask are often called filter coefficients, and a compact form of Eq. 2.43 is

$$g = f * h, \tag{2.44}$$

Where * is the convolution operator. The convolution of two images is basically a superimposition of the values of the kernel involved and therefore it represents as output how much the filter is changing the original

image. Often, the filtering operator can cause boundary effects in the sense that the effect is to darken the corner pixels of the kernel. To avoid this behavior, padding effects can be included in the filtering process. Different types of padding modes are available in literature, the most important are:

- zero: set all pixels outside the input image to 0;
- constant: the corner pixels are set to a specific border intensity value;
- wrap: loop around the image in a toroidal configuration;
- clamp: repeat edge pixels indefinitely;
- mirror: reflect pixels across the image edge;

Figure 2.53 shows some results of padding modes.

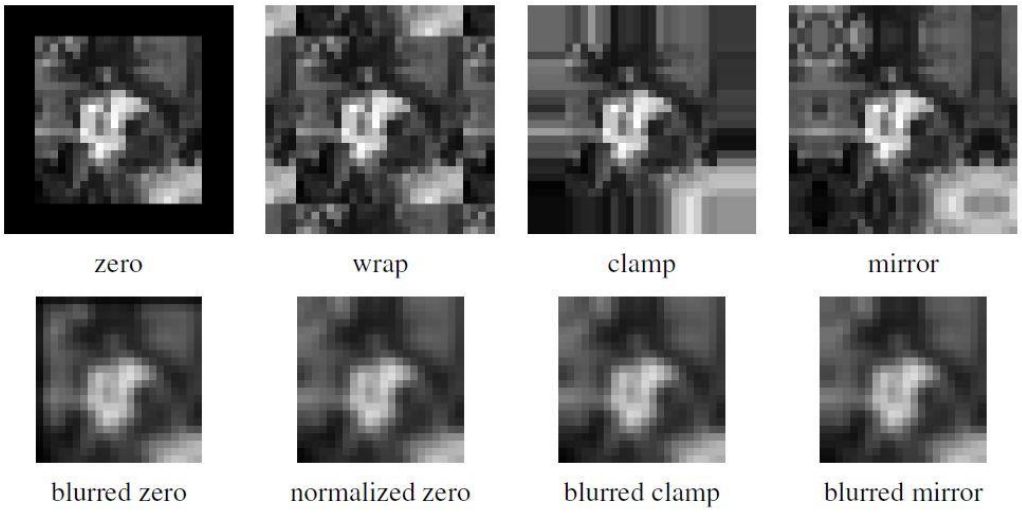

Figure 2.53 Different padding modes

Given that, it is worth to mention band-pass filters that can filter out both low and high frequencies content. One example of this type of filters is the Gaussian filter that is used to smooth the noise of the image but has some blurring as drawback. First, a Gaussian kernel is applied to the region of interest according to the following PDF:

$$G(x,y;\sigma) = \frac{1}{2\pi\sigma^2} e^{-\frac{x^2+y^2}{2\sigma^2}}, \tag{2.45}$$

And then the first or second derivative of the filtered image is used to carry out an analysis about the properties of the image. In fact, the gradient of an image tells us information about local maximum or minimum intensity values within the image whereas the second derivative, or better, the Laplacian operator is used to understand the direction of intensity of each pixel. The combination of a Gaussian filter and the application of the Laplacian operator is also known as Laplacian of Gaussian (LoG) filter, expressed by Eq. 2.46.

$$\nabla^2 G(x,y;\sigma) = \left(\frac{x^2+y^2}{\sigma^4} - \frac{2}{\sigma^2}\right) G(x,y;\sigma), \tag{2.46}$$

The results of applying this type of filter are visible in Figure 2.54.

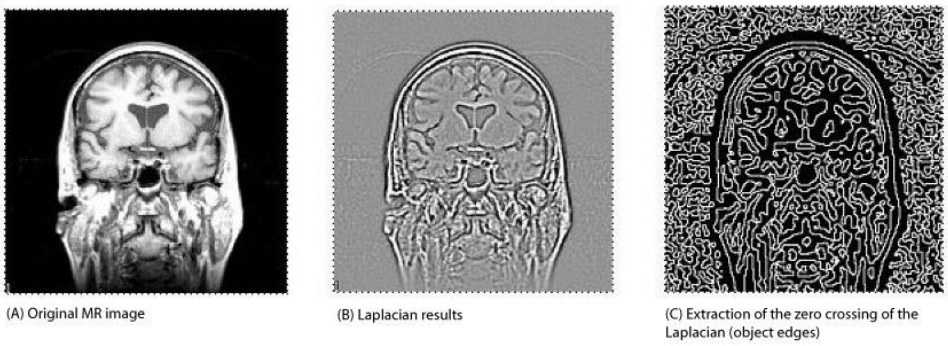

Figure 2.54 Laplacian of Gaussian filter application

As you can see, the final aim of applying a LoG filter is to enhance details giving a characterization of the edges and contours of the image. To this end, LoG is often used for edge detection and object detection. On the other hand, a Sobel operator is given by the application of a Gaussian filter at first and then applying the gradient operator in a prescribed direction. The latter is obtained by taking the dot product between a unit direction $\hat{u} = (cos\theta, sin\theta)$ and the gradient field ∇ of the image

$$\hat{u} \cdot \nabla (G * f) = \nabla_{\hat{u}} (G * f) = (\nabla_{\hat{u}} G) * f, \tag{2.47}$$

Since this filter is directional, it is common to apply it in the relevant directions of the image, namely horizontal (x) and vertical (y). An example of that is presented in Figure 2.55.

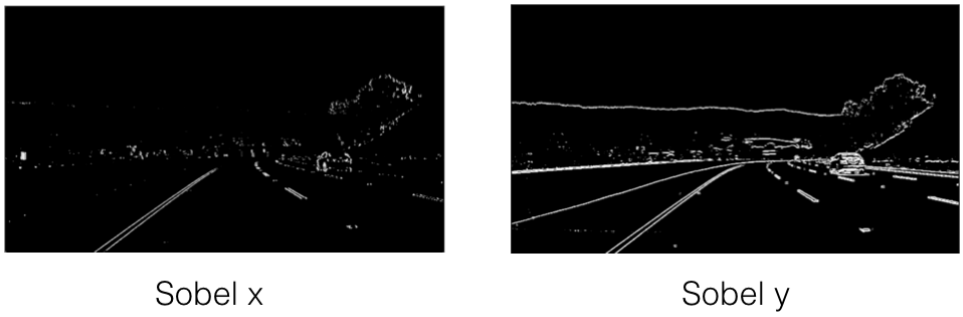

Figure 2.55 Sobel operator

It is worth to say that also the Sobel operator can be used for edge detection and contours detection as it is possible to see in Figure 2.55. Moreover, all the kind of filters presented so far are linear filters, meaning that the response to a sum of two signals is the same as the sum of the individual responses. Although this class of filters is easy to apply, not always the results obtained are good enough for the purpose of the application. Therefore, it is worth to mention at least an example of non-linear filter. Among all, one of the most used is the median filter, which replaces the intensity value of a pixel with the median intensity value of a suitable neighborhood centered in it. It is very useful to remove or at least attenuate noise, preserving edges. One downside of median filtering is that it selects only one input pixel value to replace one output pixel value, therefore it carries moderate computational cost and is not as efficient at averaging away gaussian distributed noise. A variation of this technique is called weighted median, where each pixel is used several times depending on its distance from the kernel center. Basically, this is equivalent to minimizing a weighted objective function given by

$$\sum_{k,l} \omega(k,l) |f(i+k, j+l) - g(i,j)|^p, \tag{2.48}$$

Where $g(i,j)$ is the desired output value, $\omega(k,l)$ are the weights and p is usually equal to 1 but it can also be 2 if the filtering is done considering a weighted squared mean. Figure 2.56 presents an application of median filtering.

Figure 2.56 Median filter application

At this point, an overall description of the basic image processing techniques has been provided but often for computer vision applications, this is not enough to complete a certain task. In fact, a wide branch of computer vision includes also the definition of features and descriptors of an image to compare images for instance or to reconstruct the 3D scene starting from a suitable set of images. In general, an image has an infinite number of features that can be detected but not all of them are relevant. In fact, the aim of feature detectors is to find good characteristics that can be easily tracked in the entire set of images available so that it is possible to characterize images just considering a small set of features related to them. It is possible to notice that texture-less patches are almost impossible to localize whereas the ones with high gradient change, i.e. high contrast, are easy to detect. The outcome of this procedure is often to find maximum and/or minimum in the patch and report them as detected feature point locations. The simplest criterion to match features in different images is called weighted summed square difference, that is given by

$$E_{WSSD}(\boldsymbol{u}) = \sum_i \omega(\boldsymbol{x_i})[I_1(\boldsymbol{x_i} + \boldsymbol{u}) - I_0(\boldsymbol{x_i})]^2, \tag{2.49}$$

Where I_0 and I_1 are the two images being compared, $\boldsymbol{u} = (u, v)$ is the displacement vector, $\omega(\boldsymbol{x})$ is a spatially varying weighting function and the index i identifies the summation over all the pixels of the patch considered. Features whose E_{WSSD} is below a certain threshold can be considered similar and therefore matched. There are a lot of similar criteria to match features such as using eigenvalues of the region considered or using gaussian weighting windows. Using this index measure of the similarity between two features in different images, it is possible to characterize the locations of the relevant features of an image. At this point it may happen that regions within the image that are characterized by high contrast are more populated in term of features, whereas low contrast areas have a sparse population of features. This can resolve in a wrong characterization of the image, having too much information in an area and not enough in another one. To mitigate the problem, non-maximal suppression techniques are often used; they make sure that the only detected features are the one that are local maxima or minima and whose value is significantly (10%) higher or lower respectively of a certain neighborhood around it. In general, there are a lot of different descriptors or features of an image that can be exploited to characterize an image, but sometimes the need is to have reliable and powerful descriptors. In this case, one of the most used image descriptors is the Scale Invariant Feature Transform (SIFT) descriptor, presented in 2004 by Prof. Lowe. As the name says, this descriptor is invariant to scaling constraints and rotation, being powerful for the characterization of features within an image. Moreover, they are also partially invariant to change in illumination and 3D camera viewpoint. The process of formation of the SIFT descriptor is as follows:

- **scale-space extrema detection:** The first stage searches over all scales and image locations. It is implemented using difference of Gaussian (DoG) functions;
- **keypoint localization:** At each candidate location, a suitable model is applied to determine location and scale. Only suitable candidates are selected;
- **orientation assignment:** Orientations are assigned based on the local image gradient directions. From this point on, all the operations are performed to points that are invariant to scale and orientation;

- **keypoint descriptor:** The local image gradients are measured in the selected scale in the region around each keypoint. These are transformed in a way that they are invariant also to local shape distortion and change in illumination.

The SIFT operator transforms image features data into scale-invariant coordinates linked to local characteristics of the image itself and allows common features of adjacent views of the object to be matched in an easy way. First, to characterize keypoints, candidate locations have to be found. In general, these must be invariant to scaling factors, therefore the task is achieved by looking for stable features that are not affected by scale constraints. In practice, this is performed by means of scale space functions that are continuous and able to deal with images at different scales. Among all, the most used is the Gaussian function, therefore in the case of SIFT it is possible to obtain

$$L(x, y, \sigma) = G(x, y, \sigma) * I(x, y), \tag{2.50}$$

Where $L(x, y, \sigma)$ is the scale space of the image, obtained by convoluting a variable-scale Gaussian $G(x, y, \sigma)$, with the input image $I(x, y)$. To increase the efficiency of the detection, instead of working with Gaussian functions, the operator works with Difference of Gaussian (DoG) function, convoluted with the input image. Provided that the scale factor k between two Gaussian functions is not so different, it is possible to obtain

$$D(x, y, \sigma) = \big(G(x, y, k\sigma) - G(x, y, \sigma)\big) * I(x, y) = L(x, y, k\sigma) - L(x, y, \sigma), \tag{2.51}$$

Considering the whole image, the scale space is divided in octave, each one representing a set of scale factors. For each octave a set of Gaussian function are convoluted and then subtracted to adjacent image to obtain the DoG. This means that the same image is convoluted with scale space functions with different scaling factors. This process is repeated for each octave. Figure 2.57 represents graphically the concept mentioned so far.

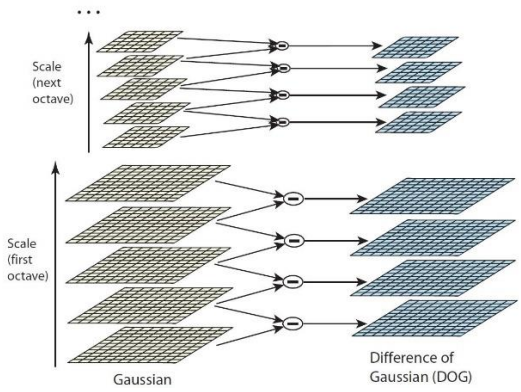

Figure 2.57 Difference of Gaussian functions in different octaves

The second step is the detection of local extrema of the images, starting from the filtered images obtained in the previous step. For each possible candidate, a 3x3 kernel is considered. Each candidate is compared with its eight neighbors in different scales within the octave. The selection is successful only if it is larger or smaller than all the neighbors in all the scales. This process may be computationally heavy since each candidate is tested within the entire octave but since the criterion of selection is very strict, each time the possible candidate is not greater or lower than the evaluated neighbor, it is automatically discarded, saving time and computational cost. There are other factors that influence the ability of detecting local maximum and minimum, such as sampling frequency and scale intervals. At the end, the choice of these factors is a trade-off between accuracy in the detection and efficiency of the algorithm.

Once a candidate keypoint has been detected, the next step is to understand if it is a strong point or a weak point, which basically means how much the point is stable and is affected by noise. Mathematically speaking, this is achieve by a 3D quadratic function, presented by Brown and Lowe in [113], that is used to determine the interpolated location of the candidate point. This function is the Taylor expansion of the DoG up to its quadratic terms, shifted so that the origin is the candidate point:

$$D(x) = D + \frac{\delta D^T}{\delta x} x + \frac{1}{2} x^T \frac{\delta^2 D}{\delta x^2} x, \tag{2.52}$$

Where $x = (x, y, \sigma)^T$ is the offset from the sample point in which D and its derivatives are evaluated. The location of the extremum $\hat{x}$, is calculate by taking the first derivative of $D(x)$ with respect to x and setting it to zero, obtaining

$$\hat{x} = \frac{\delta^2 D^{-1}}{\delta x^2} \frac{\delta D}{\delta x}, \tag{2.53}$$

If the offset $\hat{x}$ is larger than 0.5 in any dimension, this means that the location of the extremum is wrong, therefore the location of the point is changed, and the candidate point is discarded. This process allows to eliminate possible outliers in the results as well as increase the stability and robustness of the remained candidates. Figure 2.58 shows a graphical result of this approach.

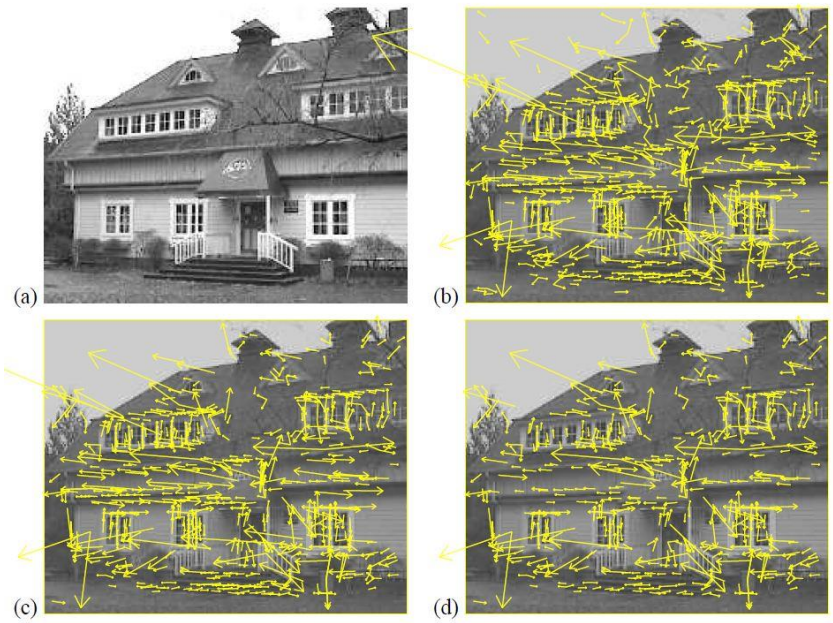

Figure 2.58 Stages of keypoints selection. (a) original image. (b) Initial keypoints location (832 candidates). (c) After applying a threshold on minimum contrast (729 candidates). (d) Final 536 keypoints, after an additional threshold.

The third step in the characterization of a SIFT descriptor is the assignment of an orientation. The aim is to define an orientation for each candidate, based on local properties, so that the point can be represented relative to its orientation, therefore achieving invariance with respect to this parameter. From the scale space functions $L(x, y, \sigma)$, it is possible to compute the magnitude and the orientation, according to

$$m(x, y) = \sqrt{\big(L(x+1, y) - L(x-1, y)\big)^2 + \big(L(x, y+1) - L(x, y-1)\big)^2}, \tag{2.54}$$

$$\theta(x, y) = tan^{-1} \frac{\big(L(x, y+1) - L(x, y-1)\big)}{\big(L(x+1, y) - L(x-1, y)\big)}, \tag{2.55}$$

From these values, an orientation histogram is created, containing 36 bins covering 360 degrees. Each candidate point is inserted in the histogram, weighted by its magnitude and by its neighbor's magnitude, considering a Gaussian-weighted function. As a result, peaks in the histogram corresponds to dominant orientations of local gradients. Each peak whose magnitude is above 80% of the highest peak's magnitude is considered to the definition of a keypoint, even if the concentration is close to the dominant peak. Figure 2.59 shows an example of keypoint descriptor creation.

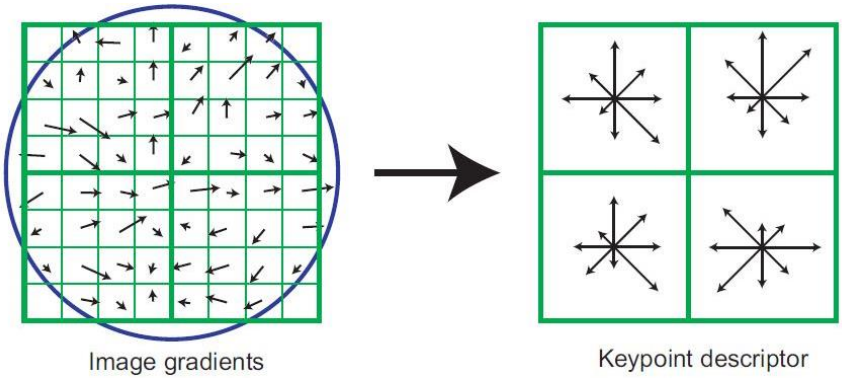

Figure 2.59 Image description characterization

As explained above, after computing the magnitude and the orientation, the set of samples around the keypoint location, in this case an 8x8 matrix, is weighted using a Gaussian window (blue circle) and the descriptor is created. The length of the arrows represents the sum of the gradient's magnitude towards the direction considered. So far, descriptors are invariant to scale and orientation change therefore the last step is to account for possible variation in the illumination or 3D viewpoint. The final descriptor is a vector containing relevant features coming from values taken from the magnitude-weighted orientation histogram. To decrease the effect of illumination and change in the point of view, the descriptor vector is first normalized to unit length. This guarantees invariance with respect to illumination changes and it can be proven considering two different scenarios. If the contrast of the image is changed, each pixel value of the image will be multiplied by a constant. In the case of gradients, each gradient is multiplied by the same amount therefore with normalization, the contrast effect is canceled. On the other hand, in case of brightness change, a constant is added to each pixel. Since, the gradients values are computed considering a difference between images, the effect of adding a constant disappears. For these two reasons, it is possible to say that the SIFT descriptor is invariant to change in illumination. The final descriptor obtained is highly stable and guarantees reliable results in the process of keypoints matching. For further details about this operator, interested readers can refer to the work of the developer of the SIFT descriptor, Prof. Lowe, in his work [114], published in 2004. After defining image descriptors, it is worth to briefly mention the possible strategies to match descriptors between different images. Often, feature descriptors are designed so that the Euclidean distance in the features space can be directly used in the matching process. Therefore, a possible strategy is to set a threshold in the maximum Euclidean distance between two descriptors in different images and take only those matches that are within the threshold value. In this case, the difficult thing to set is the value of the threshold since a large one creates false positives whereas a small one leads to false negatives, meaning that good matches are discarded. There are several methods to test the efficiency of the threshold used, but the explanation of them is beyond the scope of this research. Other possible matching strategies are fast nearest neighbors-based matcher or Brute-Force matcher. Once defined image descriptors and possible matching algorithms to find common features in different images, it is worth to mention some algorithms for edge detection. In fact, edge points carry a lot of information within the image and can be used to detect contours as well as qualitatively characterize objects in the image. An edge point is defined as a boundary between region of different texture, intensity or color; therefore, it enables to segment an image in different parts allowing to perform a large variety of operations onto it depending on the computer vision application. An easy way to define an edge is to look for sharp changes in intensity values, therefore the operator used is the jacobian, defined as the field of gradients in different directions. The formulation considering relevant directions within the image is as follows:

$$J(x) = \nabla I(x) = \left(\frac{\delta I}{\delta x}, \frac{\delta I}{\delta y}\right)(x), \tag{2.56}$$

This operator points towards the direction of steepest ascent intensity function. Unfortunately, this process tends to enhance noise presence in the image, therefore is common rule to apply a filter before computing the jacobian to smooth the noise content of the image. Due to its powerfulness, the Gaussian filter is one of the most used for these kinds of tasks. Without going into further detail, it is worth to mention at least one edge detection

method that summarize the properties discussed so far. Among all, the most used is the Canny method, presented by Prof. John F. Canny in 1986 [115]. It is one of the most reliable methods since it guarantees good detection, good localization and single response to an edge. A typical implementation is divided in the following steps:

- smoothing of the image with a proper Gaussian filter to reduce noise content;
- determine gradient magnitude and orientation for each pixel;
- detect the edge comparing magnitudes of a relevant neighborhood in a certain direction. The pixels that are not strong enough to define an edge are marked as background (non-maximum suppression).
- remove weak edges with double thresholding methods (hysteresis thresholding).

The first step has been defined before when characterizing different filtering techniques for image processing. The Gaussian kernel is moved within the input image in order to be applied to the entire image. The size of the kernel is very important for the detection. As a rule of thumb, the smaller the dimension, the higher the sensitivity of detection of the algorithm. The smallest kernel possible is a 3x3 matrix, but the computational cost is very high. A reasonable choice to guarantee a proper trade-off is a 5x5 kernel. The next step is self-explanatory since it is basically the computation of the gradient field of the image. Once this is achieved, each direction is considered, and the magnitudes of different possible edge candidates is compared with a suitable neighborhood centered on it. In this case, by defining a certain threshold, it is possible to characterize an edge point. The third step involves the definition of weak and strong edges, using an algorithm able to discern between them and discard the former set. First, it is important to compare a candidate edge strength with the strength of the pixels in the positive and negative orientation selected. If the value is the largest compared with the others, it will be preserved, otherwise it is suppressed. To further improve the stability of the algorithm, it is also possible to define two thresholds, one for low strength and one for high strength that can be used to further characterize strong and weak edges. In this way, only edge points in which there is a sharp change in intensity, color or texture will be kept. Figure 2.60 reports an example of the application of the Canny method.

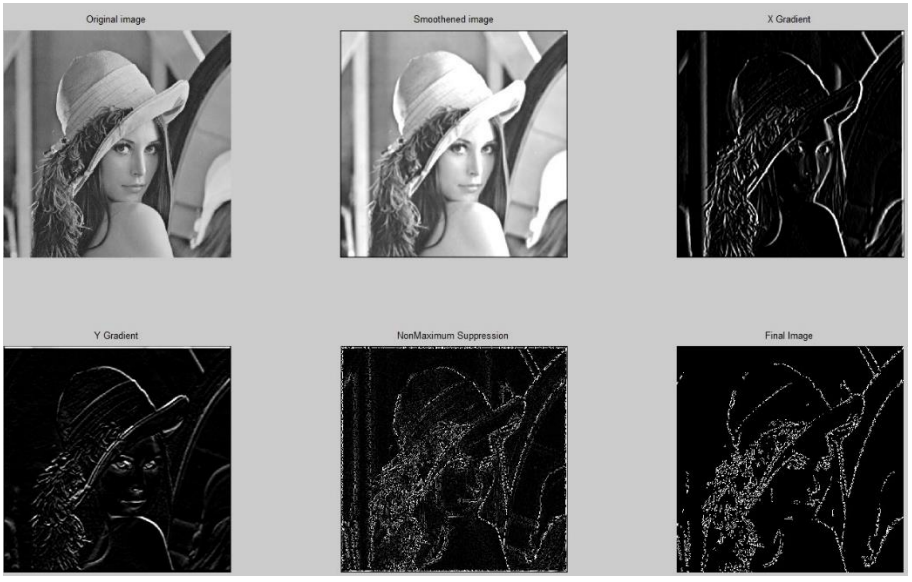

Figure 2.60 Canny method application

For further details about the Canny method, interested readers can refer to the work of Ding et al. in [116], which provides an accurate analysis of the method. The last part of this section is dedicated to a photogrammetric method within the field of computer vision known as Structure from Motion.

Structure from Motion (SfM) is a photogrammetric technique used to estimate the location of 3D points from multiple images, given a set of correspondences between image features. The result is the reconstruction of a 3D virtual model of the object included in the set of images provided as input. Roughly speaking, SfM can be divided in three fundamental steps: (i) extraction and matching of features in images, (ii) camera motion estimation, (iii) digital reconstruction of the 3D structure. The first topic to discuss is triangulation. This is the problem of reconstructing the depth coordinate of a point starting from images. The way to solve this problem is to find the 3D point $\boldsymbol{p}$ that is as close as possible to the 3D rays corresponding to the 2D matching feature location $\{\boldsymbol{x_j}\}$ observed by the cameras. The nearest point to $\boldsymbol{p}$, denoted as $\boldsymbol{q_j}$, is the one minimizing the distance

$$\left\|c_j + d_j \hat{v}_j - p\right\|^2, \tag{2.57}$$

Where $\boldsymbol{c_j}$ is the jth camera center, $\hat{v}_j$ is the direction of the ray and $\boldsymbol{d_j} = \hat{v}_j(p - c_j)$ is the relative distance. Figure 2.61 highlights the process discussed so far.

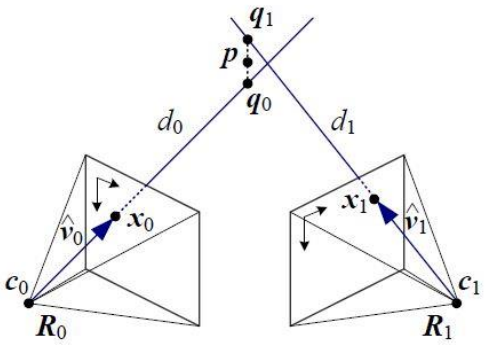

Figure 2.61 Triangulation schematic

Therefore, the best approximation of p is given by

$$q_j = c_j + \left(\hat{v}_j \hat{v}_j^T\right)(p - c_j) = c_j + (p - c_j), \tag{2.58}$$

The best point able to represent the actual point $\boldsymbol{p}$ can then be found using a regular least square problem. In this scenario, the location of the cameras was considered as a known parameter but in practice SfM aims to simultaneously estimate the position and reconstruct the 3D point. To do that, it is necessary to introduce the concept of epipolar constraint. Considering Figure 2.62, since the camera positions are unknown, it is possible to set the first camera origin $\boldsymbol{c_0} = \boldsymbol{0}$ and at a canonical orientation $R_0 = I$, without loss of generality. The observed location of point $\boldsymbol{p}$ in the first image, $\boldsymbol{p_0} = \boldsymbol{d_0}\widehat{x_0}$ is mapped into the second image by the transformation

$$d_1\widehat{x_1} = p_1 = \boldsymbol{R}p_0 + \boldsymbol{t} = \boldsymbol{R}(d_0\widehat{x_0}) + \boldsymbol{t}, \tag{2.59}$$

Taking the cross product of both sides of Eq. 2.61 with the translation vector t, yields to

$$d_1[\boldsymbol{t}] \times \widehat{x_1} = d_0[\boldsymbol{t}] \times \boldsymbol{R}\widehat{x_0}, \tag{2.60}$$

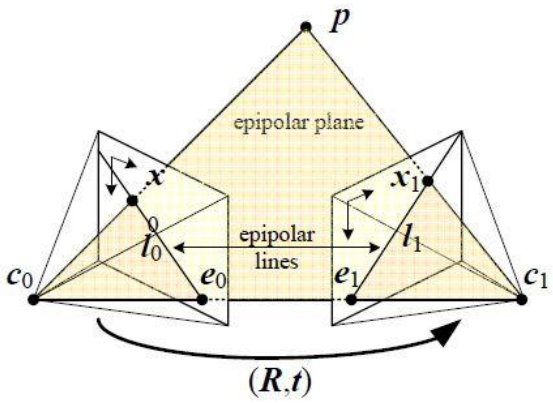

Figure 2.62 Epipolar constraints

since the cross product of the second element on the right side is zero. Moreover, taking the dot product in both sides with $\widehat{x_1}$, it is possible to obtain

$$d_0\widehat{x_1}([\boldsymbol{t}]\mathrm{x}\boldsymbol{R})\widehat{x_0} = d_1\widehat{x_1}[\boldsymbol{t}]\ \mathrm{x}\ \widehat{x_1} = 0 \tag{2.61}$$

Since the right side is a triple product with two identical entries. Provided that, Eq. 2.61 yields to the definition of epipolar constraint

$$\hat{x}_1^T \boldsymbol{E}\hat{x}_0 = 0, \tag{2.62}$$

Where E is called the essential matrix. It is worth to notice that the matrix E maps a point in the image 0 into a line in the image 1. The set of possible lines are called epipolar lines (Figure 2.60) and pass through the epipoles $\boldsymbol{e_0}$ and $\boldsymbol{e_1}$. Thanks to the matrix E it is possible to define the relative location of cameras, by solving Eq. 2.62, hence solve the system of equations related to the rows of the matrix E. If the order of the system is too high or images are very noisy, find a solution of the set of equations can be tricky therefore it is possible to solve the matrix E by using a Singular Value Decomposition (SVD) approach. Provided that, the relative location of the cameras is guaranteed, or at least an estimation of it, accurate within a certain threshold. At the same time, the algorithm must guarantee an adequate self-calibration of the cameras, enabling a proper reconstruction of the 3D scene. For instance, if there are parallel lines in the scene, it is possible to determine some vanishing points, i.e. images of points at infinity, which can be used to characterize the homography matrix $\boldsymbol{M}$ at infinity from which focal lengths and rotations can be recovered. Since it is not always possible to work in such conditions, most of the self-calibration methods consider some restricted forms of calibration matrix that simplify the reconstruction of the parameters of the camera. To this end, it is worth to mention a method used in several applications of photogrammetry and SfM that allows to perform a reliable non-linear minimization of the measurement reprojection errors called bundle adjustment. Basically, the feature location measurements $\boldsymbol{x_{ij}}$ depends not only on the point $\boldsymbol{i}$ but also on the camera pose $\boldsymbol{j}$

$$x_{ij} = \boldsymbol{f}\big(p_i, \boldsymbol{R}_j, c_j, \boldsymbol{K}_j\big), \tag{2.63}$$

Where $\boldsymbol{p_i}$ is the 3D point location, $\boldsymbol{R_j}, c_j, \boldsymbol{K_j}$ are the rotation, optical center and calibration matrix of the camera $\boldsymbol{j}$ respectively. This method provides initial camera intrinsic and extrinsic parameters and 3D structure estimates, as close as possible to real values. Each time a new image is considered, the method tends to update the parameters obtained in previous steps by computing non-linear least square algorithms with many points in the image added. To summarize what explained so far, it is possible to say that bundle adjustment method aims at predicting the locations of a set of points in a certain set of cameras, in parallel with the estimation of the 3D scene described by the images. This is achieved by providing an initial cameras' location estimation and minimizing the total reprojection error with respect to the 3D scene. From a mathematical point of view, it is possible to say that given $\boldsymbol{n}$ 3D points, viewed by a set $\boldsymbol{m}$ of cameras and being $\boldsymbol{x_{ij}}$ the projection of the $\boldsymbol{i}$th point

in the jth image; identifying as v_{ij} a binary variable that is 1 if point i is visible in image j and 0 otherwise, and also assuming that each 3D point is parameterized by a vector b_i and each camera by a vector a_j, the bundle adjustment method yields to the minimization of

$$\min_{a_j,b_j} \sum_{i=1}^{n} \sum_{j=1}^{m} v_{ij} d\left(Q\left(a_j, b_j\right), x_{ij}\right)^2, \tag{2.64}$$

Where $Q\left(a_j, b_j\right)$ is the predicted projection of point i into image j whereas $d(\cdot)$ represents the Euclidean distance between the actual position and the prediction. Bundle adjustment is basically the core of Structure from Motion. In fact, the usual pipeline is as follows:

- detection of keypoints in each image (often SIFT descriptors);
- matching of keypoints within the set of images;
- random sampling and consensus (RANSAC) algorithm applied to discard possible outliers and estimate essential matrices between pair of images;
- adding further images and repeatedly compute the bundle adjustment method;
- create a 3D points cloud with all the keypoints matched;
- reconstruct the three-dimensional digital model of the structure considering cloud's points as vertices of mesh polygons.

Figure 2.63 tries to graphically explains the pipeline of Structure from Motion.

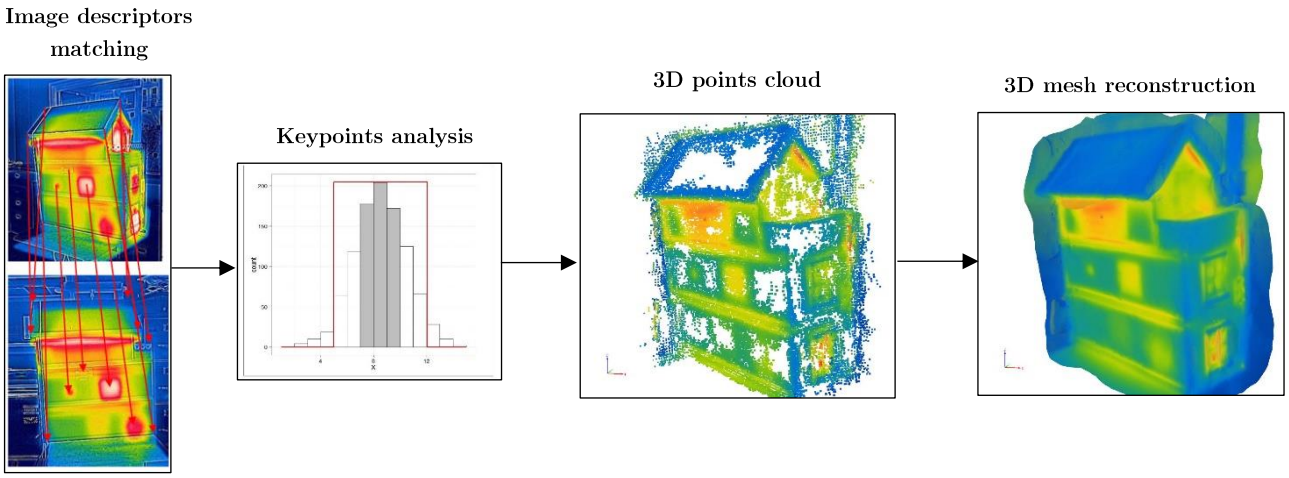

Figure 2.63 Simplified workflow of Structure from Motion

For a more detailed analysis of structure from motion and all the algorithms used within it, interested readers should refer to [109], [110], [117], [118]. Often, if not enough metadata about the set of images are provided, the reconstructed 3D model may be characterized by strange dimensions that are useless for a quantitative analysis of the model. Therefore, to obtain the actual dimensions of the object, the 3D distorted reference frame in which keypoints are expressed is converted into the global reference system. To achieve this result, it is possible to use different approaches: i) a minimum of three non-aligned Ground Control Points (GCPs). GCPs are distinguishable points in the scene with known coordinates, often measured by using Ground Control Stations (GCSs), that are easy to pinpoint in the images and allow defining the transformation matrix

(i.e., three translations, three rotations, and a scaling factor) by comparing their coordinates in the two different coordinate systems. ii) Another possibility is to extract georeferenced data directly from images and identify the global coordinates in the 3D virtual reference frame. iii) A scaling constraint can be introduced. Knowing with a certain accuracy one dimension of the object, it is possible to compare the measure with the measure in the 3D virtual space and define a scaling factor to apply in the whole reconstruction. This allows to directly scale the entire model and obtain reliable results within a certain error. Structure from Motion has been applied to a variety of different scientific domains. Notable examples include geosciences [119], agriculture [120], heritage buildings surveying [121], and large-scale civil infrastructures inspection (e.g., dams [103], railroad tracks [122], bridges [123], and road pavement [124]). For further details about image processing techniques and Computer Vision applications, interested readers should refer to the following book [125] of professor Szeliski that provides a detailed analysis of all the topics treated in this section.

Part II

Second Part

Chapter III

3. Methodology

The following section is devoted to the explanation of the methodology used in the research conducted for this thesis work. First, a focus on the structure used as case study for the tests is provided, along with a brief explanation about the type of infrared thermography test performed. Then, the equipment used for testing is analyzed focusing on the specifications and the motivation behind the use of such instruments. Provided that, a focus on the technique used to obtain the results is provided, highlighting opportunities and challenges, along with the software used for the interpretation of data. Finally, a careful analysis of the algorithm developed for automatic damage detection is tackled, trying to understand the reasons behind each step and the parameters involved in the detection of damages.

3.1 Case study for experimental testing

The case study for the entire set of testing performed is a laboratory scaled three stories building, represented in Figure 3.1. The house is made of wooden-based materials, mostly plywood, which is intended to simulate common buildings in the United States. The inside of the house has been cleared to allow the proper installation of equipment and structural components.

Figure 3.1 House structure used for testing. a) Northern façade; b) Western façade; c) Southern façade.

As it is possible to see from Figure 3.1, there are three relevant façades of the house, namely Northern, Western and Southern ones. It is also possible to notice that both in Figure 3.1 a and c door and windows are present. The former was made with polyvinyl chloride (PVC) material to guarantee a different thermal behavior in correspondence of the element, whereas windows are composed by the same material used for the door and a thin layer of transparent plastic material to simulate glass presence. Finally, the southern façade can be distinguished from the northern one since a deck is present, as it is possible to notice from both Figure 3.1 b and c. The house, as it is, does not provide too much meaning in terms of thermal behavior since the only possible sources of heat losses are related to draught through windows and doors and possible presence of gaps beneath

the roof. Therefore, to adequately simulate a real case scenario, some adjustments were made. First, a layer of insulation material was installed in the roof and in the façades. For what concerns the roof, a 2,5 cm thick layer of expanded polystyrene (EPS) foam was installed, whereas for plywood walls, the thickness of the layer is 2 cm. The reason behind this choice is that in percentage, heat losses are higher in correspondence of roofs and ceilings when compared with walls, therefore the aim was to guarantee a homogeneous thermal behavior in sound areas of the building. EPS is a very lightweight material, generally composed by 98 % of air that is widely used in construction industry for insulation and packaging. It is characterized by a very low thermal conductivity or conversely a high thermal resistance, coming from the microstructure of the material. In fact, the air trapped within the closed structure of the cells is a poor heat conductor that results in a very efficient insulation material. Usually, the thermal conductivity of EPS foam of density 20 kg/m^3 is 0.035-0.037 W/mK at 10° C. In addition to that, it is characterized by low moisture absorption and cushioning properties, very important to avoid the presence or growth of defects in walls and roofs. Provided this information about the house, it is worth to mention the adjustment performed on it in order to simulate heat-related flaws in the envelope. As it is possible to notice in Figure 3.2, three different categories of defects are present. All of them are in the Western façade and are sub-superficial, justifying the usage of infrared thermography for the inspection. In the third story, a water infiltration defect is recreated. In fact, infiltrations within the envelope are a serious problem in buildings therefore a defect of this kind couldn't be avoided. Practically, the insulation material was cut, reducing its thickness to 1 cm, equally divided between internal and external sides of the façade. To simulate water content, a sealed bag of water was inserted in the gap created in the insulation material. The defect is 30 cm wide and 10 cm high, simulating a severe problem considering the dimensions of the house.

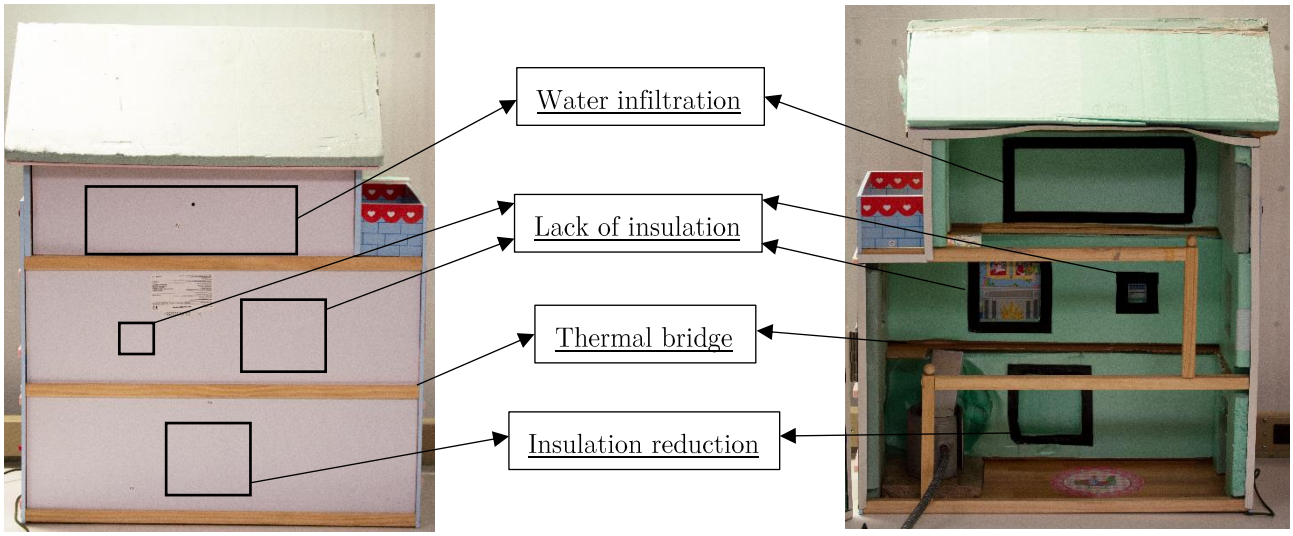

Figure 3.2 Fabricated defects in the case study house

The second category of fabricated defects is related to the second story. In fact, the insulation material in correspondence of the defects is completely missing, simulating a situation of severe damage of the structure. Without insulation material, heat can easily pass through the envelope and cause an increase of energy consumption. Two different squares where insulation material is missing are present, the area of the biggest one is 100 cm^2 whereas the small one is 9 cm^2. The third type of sub-surface defect is related to a reduction of insulation material. In fact, the thickness in correspondence of the damaged area is 1 cm, half the original value and the dimensions are 10 cm x 10 cm. It is possible to locate the defect in the first story. For what concerns flaws, it is also worth to mention two thermal bridges, installed in between stories as it can be seen in Figure 3.2, dividing the insulation material. A thermal bridge is a component characterized by a higher thermal conductivity than the materials surrounding it, therefore it creates a path of low resistance to heat transfer. In real cases, they can be present in different locations such as floor to wall junctions, like in the case presented; windows to wall junctions or door to wall junctions. Therefore, it is worth to investigate their presence in a building and their

consequences in the overall thermal resistance of the envelope and increase in energy consumption. Another fabricated anomaly of the structure is the presence of gaps both among roof and walls and on the sides of the northern and southern facades to simulate the presence of draughts in the envelope, commonly present in housings.

3.2 Equipment and NDT technique

Provided a good description of the objective of the tests, it is worth to describe the typology of testing performed in the related work. As discussed in section 2.2, nondestructive testing is a very wide field of applications for identifying and detecting anomalies in structures. Depending on the type of information needed, some methods may be better than others. In this scenario, infrared thermography is the type of testing chosen for inspecting the structure and identifying defects accountable for heat losses. In fact, by measuring the infrared radiation of objects, it is possible to detect regions within the structure characterized by different thermal conductivity than sound areas, that can be interpreted as areas of malfunctioning of the structure causing heat related losses. The first important decision to take is whether conducting an active or passive thermography test. As explained in section 2.2.8, each of the two carries drawbacks, therefore the choice is constrained to the type of application. In the case presented in this research, active thermography is the best way to go since the purpose of the test is to clearly identify fabricated defects. It doesn't make any sense to inspect the structure at its 'normal' temperature state since the purpose is not to find unknown defects but to identify the ones fabricated. In sight of this reasoning, four electrical heaters where placed inside the house, in strategic location to warm up the house in a homogeneous way. The objective is to create a relevant temperature gradient between sound and damaged areas to facilitate the detection. It is worth to mention that the test is performed in steady state, meaning that the temperature inside the house should be as constant as possible throughout the entire test. To guarantee that, two thermocouples where installed inside the house to carefully monitor the temperature in two relevant spots. Moreover, to achieve a proper temperature steadiness, the structure has been heated up for at least two hours for each test to guarantee that the temperature inside it remains as constant as possible during the test. The objective of the test is to recreate a real-world scenario of a building's condition in wintertime, where the principal source of heat loss comes from the HVAC system. To perform such tests, two different platforms were utilized, a hand-held thermal imager and an unmanned aerial vehicle (UAV) platform, equipped with an infrared camera. The first test was performed by means of a FLIR ONE Pro thermal camera [126], depicted in Figure 3.3. This thermal imager embeds both a visible and thermal camera to allow a comparison among them in order to interpret the obtainable results in a better way. It is a camera attachable to a smartphone that allows quick and reliable assessment of thermal conditions of a structure. It is characterized by a 160x120 pixel resolution for what concerns the thermal imager and a 1440x1080 pixel resolution for the visible camera.

Figure 3.3 FLIR ONE Pro thermal imager

It allows to measure temperatures up to 400°C, enabling spot measurements within the thermal image. The pixel size corresponds to 12 µm and it is able to detect electromagnetic waves in the range between 8 µm and 14 µm, almost the entire spectrum of near and mid infrared radiations. The frame rate is 8.7 Hz, the horizontal field of view (FOV) is 55° ±1° whereas the vertical one is 43° ±1°. The minimum resolvable

temperature difference (MRTD) of the camera is 150 mK, that explicitly defines the thermal sensitivity of the camera. The spot meter functionality has a resolution of 0.1°C and it has different emissivity settings depending on the surface of the object. The accuracy of the camera is ±5%, typical percentage of the difference between ambient and scene temperature. It is worth to mention a functionality of this camera that will be largely exploited in the contest of this work. The FLIR ONE Pro camera allows to merge visible and thermal images in the so-called Multi-Spectral Dynamic (MSX) Imaging, where visible light details are added to thermal images in order to enhance image clarity, embedding edges and outlining details onto the thermal readings. Unlike image fusing, MSX does not affect the thermal image or decrease thermal transparency. This improves the image definition and makes it easier to detect the shape of possible damages. Figure 3.4 clarifies the concept of MSX, presenting a thermal, a visible and an MSX image to understand the differences.

a) 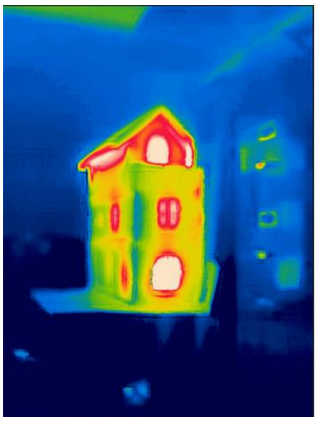 b)  c) 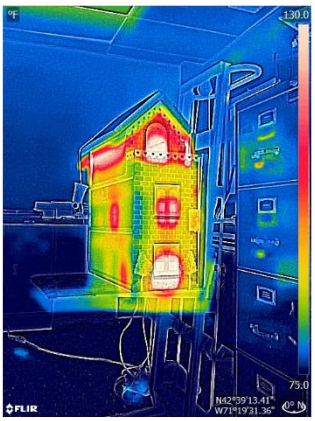

Figure 3.4 Different results obtainable from FLIR ONE Pro imager. a) thermal image; b) visible image; c) MSX image.

As it is possible to notice from Figure 3.4 c, the quality of the details of the image is quite enhanced when comparing it with the thermal image (Figure 3.4 a). This is very helpful when it comes to Structure from Motion since the quality and powerfulness of image descriptors is increased, allowing a better digital reconstruction of the structure. Even though this digital imager is not the state of the art in its sector, it allows an easy and sufficiently reliable outcome for what concerns defects characterization and verify the potentiality of the proposed approach in a controlled environment. To perform such test, the house was placed at approximatively 1 meter of height from the floor to guarantee adequate space around it to move with the camera. Moreover, to obtain an adequate field of view, the working distance has been set to 2 meters in order to capture the complete structure into each image. For Structure for Motion purposes, the camera was placed into a tripod to facilitate movements around the structure and the path followed was a semi-circle. Figure 3.5 tries to better explain the acquisition phase adopted for the test.

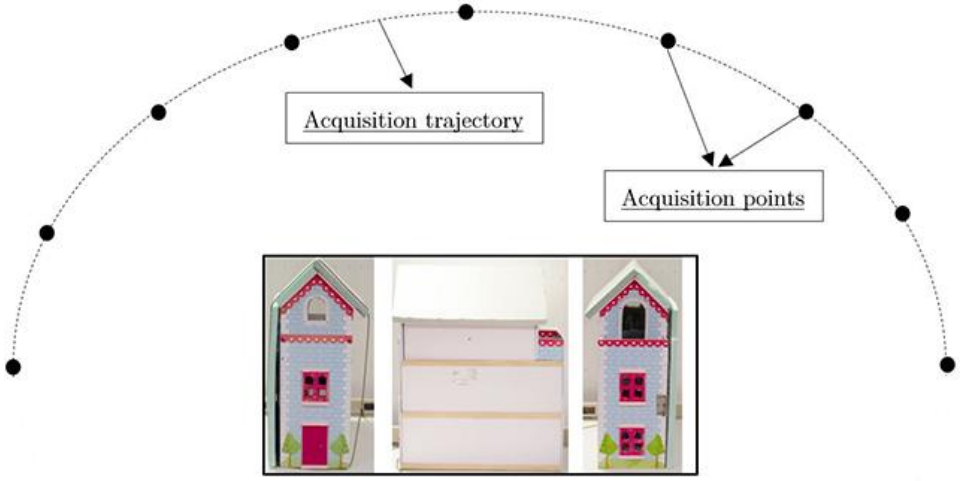

Figure 3.5 Photogrammetric acquisition trajectory

Moreover, to guarantee a sufficient overlap of images, a mark each 15 centimeters was placed on the semi-circular trajectory, to identify the acquisition point in order to guarantee sufficient lateral and frontal image overlap. In this way, each acquisition is made approximately each 10 degrees. Moreover, the acquisitions were made at two different height planes, 1 meter and 2 meters from the ground in order to guarantee sufficient information about the house under inspection. The second platform deployed in the IRT testing is composed by a DJI MATRICE 200 V2 [127] unmanned aerial vehicle with a DJI ZENMUSE XT2 [128] imager, integrated as a payload in the gimbal support. The specifications related to the former can be summarized in Table 3.1.

Table 3.1 Quadcopter technical specifications

Parameter	Value
Weight (without payload)	4.53 kg (10 lbs)
Aircraft diameter (motor-to-motor)	64.3 cm (25.3 in)
Aircraft height	37.8 cm (14.88 in)
Motor type	Brushless DC
Battery size and type	LiPo – 174.6 Wh
Maximum payload weight	1.61 kg (3.55 lbs)
Maximum hover time (Full payload)	24 minutes
Maximum speed	82.72 km/h (51.4 mph)
Maximum wind resistance	43.2 km/h (26.84 mph)
Temperature range	-20° to 45°C (-4° to 113°F)

This is a UAV quadcopter platform, whose airframe is made of carbon fiber to guarantee light weight and strength at the same time. It is designed to enhance robustness in all flighting conditions, mounting a gimbal for positional control and stability. Its structure allows a relatively large payload (approximatively 1.6 kg) to be fitted beneath the rotor-lifting plane. The gimbal structure is characterized by an angular vibration range of ±0.01°, a controllable range of +30° to -90° for what concerns the tilt angle and a ±320° when it comes to panning the camera. For what concerns the payload, the ZENMUSE XT2 camera is a detachable camera, produced in a collaboration between DJI and FLIR Systems, embedding both a thermal and a visible imager. The former is composed by an uncooled vanadium oxide microbolometer, enabling electromagnetic infrared acquisitions in the range between 7.5 and 13.5 µm of the electromagnetic spectrum. It is characterized by a focal length of 25 mm, a FOV of 45°x37° and a 640x512 pixel resolution. It has a frequency frame rate of 30 Hz and an NETD of 50mK. It can operate with high accuracy in a temperature range between -40° and 550° C and it allows both multiple spot and areas measurements. On the other hand, the visible camera is composed by a 1/1.7" CMOS sensor, with an effective resolution of 12 megapixels (3840x2160). It is characterized by a 57.12°x42.44° FOV, enabling 4K Ultra HD videos. Figure 3.6 shows the equipment mentioned so far.

Figure 3.6 DJI MATRICE 200 V2 with ZENMUSE XT 2 imager

The second test on the house was performed using this platform, in the inner courtyard of the university campus buildings. The house was heated up for almost 5 hours to guarantee adequate steadiness of the temperature. The test was performed around 7 pm to guarantee an adequate outcome and avoid possible external factors that would have altered the results (see section 2.3). The flight path was semi-circular, characterized by a radius of 2 meters from the house. Three different height planes were used for the acquisition. Starting from 1 meter of height up to 3, in order to acquire sufficient images to guarantee an adequate result. First, a manual flight was performed by means of a remote controller, then an attempt of automated flight path was investigated by means of an application of the manufacturer company called DJI Pilot. The results were not great since the distance covered was very short and the local position of the drone was highly affected by the limited accuracy of the georeferencing system of the UAV. As mentioned before, the scope of the research is to validate a theoretical novel technique for damage inspection. In fact, not much work has been done towards this direction and almost none in the way proposed in this thesis. Many studies found out that it is possible to accurately reconstruct models of structures and infrastructures starting from a visible set of images exploiting Structure from Motion approaches, since the images' resolution is in general sufficiently high and several details can be extrapolated from them, allowing to have meaningful image descriptors. When it comes to thermal inspections, the common way of doing inspection is to first reconstruct the visible model and then overlap to it thermal images to locate damages or critical areas under analysis. The novelty introduced in this work is to directly reconstruct the model starting from thermal images, so that the reconstruction is a thermal map of the structure under analysis that can be investigated remotely and that allows to identify both qualitatively and quantitatively anomalies related to heat losses. Hence, the advantage is to have directly a model in which it is possible to perform an investigation, without compromising or harassing the structure involved. The combination of IRT and SfM for structural health monitoring carries also some drawbacks. In fact, the resolution of thermal images is generally lower than the one in the visible spectrum therefore the overall reconstruction could be less accurate and the image descriptors not representative of the main characteristics of the image. In this work, the feasibility of implementing this new approach was investigated using a laboratory-scaled three-story house in order to validate the theoretical analysis and evaluate the accuracy of the results. The usage of the UAV may seem useless for the type of investigation, but the purpose was also to demonstrate that the same inspection can be carried out in any structure, independently from dimensions. In fact, the implementation of a drone has been useful to demonstrate that large areas can be inspected in the same way as the experiments conducted in the house. Moreover, the powerfulness of the approach relies on the fact that inspections can be performed in harsh environmental conditions or in locations that are hardly accessible for human beings, obtaining a virtual model that can be used to perform energetic audit and assess structural conditions without harming the safety of the inspectors. For what concerns Structure from Motion, the software Pix4DMapper was used to perform the digital reconstruction starting from thermal images. In the latter, several parameters can be interrogated, allowing an adequate level of customization of the results. In fact, it is possible to obtain also intermediate results, such as keypoints matching, 3D points cloud and categorization of each single point depending on its nature (e.g. nature, construction, sky, car, etc.). Figure 3.7 represents a general summary of the tests performed.

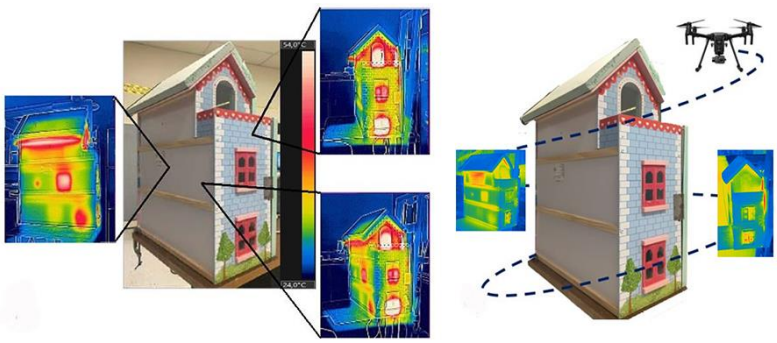

Figure 3.7 IRT testing. a) Hand-held FLIR ONE Pro camera; b) DJI MATRICE 200 V2 equipped with ZENMUSE XT2 camera

From the software it is also possible to extrapolate quantitative results, allowing to measure segments, surfaces, areas and volumes, provided a reliable virtual reference frame. Said that, it is important to understand how thermal images are post-processed prior to be fed to the software. First, the histogram of each image is equalized to spread the intensity levels of the image and have a more detailed and enhance image as output. Then, the maximum and minimum values of temperature are set to be the same in each image since the purpose is to not only detect defects but also perform a quantitative analysis on them. Finally, a suitable set of colors' palette has to be chosen to guarantee the best results possible.

3.3 Algorithm for automated damage detection

The last part of the work is related to the development of an algorithm for automatic damage detection, starting from thermal images. The aim is to characterize defects, their shape and contours and overlap them to visible images to have a clear idea about the location of the anomaly. The algorithm has been tested both in a controlled laboratory experiment, i.e. laboratory-scaled building, and in a real-world application, using a set of thermal images of concrete bridges' infrastructures in Lowell (MA). The latter are characterized by several damages such as cracks, delamination, spalling and water infiltrations. In this case, the analysis was carried out using a FLIR E60bx [129] thermal imager. The challenge in this scenario is to find a powerful criterion to define a defect and find the best algorithm that fits for different typologies of damages and different temperature's ranges. In fact, the possibility to have outliers is significant since working with temperature differences, it is easy to confuse a defect with a region with different thermal conductivity in the structure. For instance, in the case of concrete bridges, the presence of a steel railing can mislead the algorithm since the thermal behavior of steel is different than that of concrete, therefore it will appear as a region of different temperature that can be interpret as a defect. Provided this example, it is obvious that the task of the algorithm proposed is very difficult compared with other applications where the detection is done in the visible spectrum or where the temperature difference is relatively high. In fact, Hiasa et al. in [130] found out that the temperature difference between damaged and sound area could be as low as ~1.5° C. On the other hand, for other tasks such as people detection [131], the task is easier since the temperature difference between background and person/people could be more than 20°C. Automatic object detection from IR images has been deeply investigated by means of energy minimization [132], fractal algorithms [133], wavelet transforms [134] and deep learning approaches [135] but only few endeavors towards damage detection in concrete structures have been made [136].

For a better understanding of the algorithm, it is worth to go through the steps to achieve the result. First, it is worth to understand what are the input images of the algorithm. In fact, different temperature levels in a thermogram are converted in a color's palette, where different colors correspond to different temperature ranges. Most of the time, blue colors identify low temperature values, while red colors are related to high temperature values. The same reasoning can be done considering grey-scaled images, where black is low, and white is high temperature. Provided that, the thermogram acquired with an infrared imager is simply a digital image, characterized by a matrix of pixels with intensity levels and three channels corresponding to fundamental colors, red, green and blue (RGB image). This is not useful for the algorithm since the aim is to work with temperature differences and images with different color's palettes can't be compared for the detection. Therefore, the first step is to transform pixels intensity values in temperature intensity values. This can be done automatically using several different software, usually provided by the manufacturer of the thermal camera. In the case of this work, FLIR Systems released a Python script that given the RGB image as input, outcomes a matrix whose dimensions are the same as the input image (height and width) and the intensity of the pixels corresponds to the temperature values. It is worth to mention that this step cannot be done individually since each camera has different settings and a different thermal sensor, therefore only the company is able to properly convert the measure of radiant flux into temperature measurements. Once obtained the temperature values, it is possible to transform them in a grey scale image, suitably scaling all the data between 0 and 255 where the former

corresponds to the lower temperature value in the matrix and 255 to the highest temperature value. At this point, the image is suitable to be an input for the algorithm. Figure 3.8 summarizes the concepts explained so far.

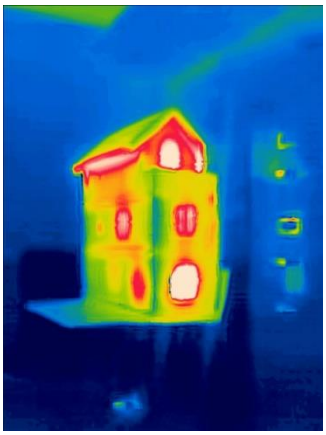

	1	··	··	240	··	W
1	22.3	22.2	21.9	21.8	22.1	22.5
:	25.1	··	··	23.7	··	24.7
:	24.6	··	··	32.1	··	24.1
:	26.2	··	··	30.8	··	26.5
:	28.9	··	··	35.4	··	32.5
320	32.1	32.5	37.5	39.1	40.9	38.5
:	31.7	··	··	34.6	··	36.4
:	30.6	··	··	32.8	··	35.2
:	28.5	··	··	28.9	··	32.9
H	27.2	··	··	25.7	··	30.1

Figure 3.8 Graphical process of temperature values extraction

Provided the grey scale image, the next step is to eliminate the background of the image. This is useful for two different reasons; first, it is possible to discard part of the image that could lead to outliers in the results that compromise the overall accuracy of the method, then the computational time is significantly decreased since the algorithm does not operate on background pixels. In practice, the elimination of the background can be achieved with different image processing techniques that work with thresholds that essentially divide the image in two classes, background and foreground. Although, for a better outcome of the thresholding method it is worth to apply a local neighborhood operator in order to enhance the quality of the results. The operator utilized in this case is called local intensities weighting (LIW) operator and it is presented in [137]. This technique will brighten bright areas, likely related to defects and darken dark areas, usually related either to background or sound areas. In this way, the application of the thresholding method will be more effective. Practically, defected areas will be set to an intensity value of 255, i.e. white, whereas sound or background areas will be characterized by a 0-intensity value, i.e. black. The output image is given by the convolution of the original image with a 3x3 kernel where the LIW operator is applied. Mathematically speaking, if the intensity of a pixel is given by $f(i,j)$, the intensity after the application of the operator, $g(i,j)$, will be the result of the multiplication of the intensities of the pixels within the kernel divided by the maximum intensity value within the kernel. Therefore, it is possible to describe the operation by means of the following equation:

$$g(i,j) = \frac{\prod_{k=i-1}^{i+1} f(k,j) \prod_{h=j-1}^{j+1} f(k,h)}{\max\left(f(k,h)\right)}, \tag{3.1}$$

Where the two products refer to rows and columns of the kernel matrix. By means of a convolutional process, it is possible to apply the operator to the entire image. Figure 3.9 represents a graphical explanation of Eq. 3.1.

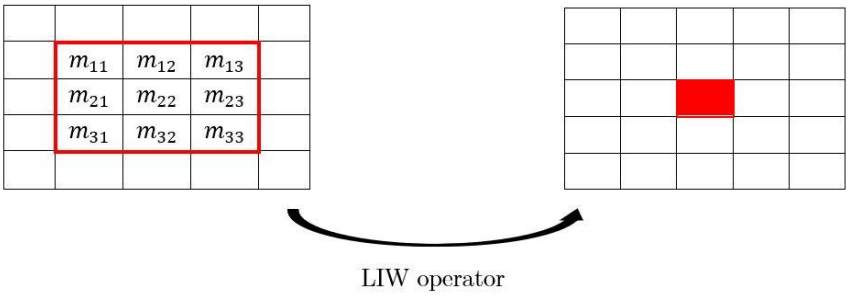

Figure 3.9 LIW operator

In the case presented in this algorithm, the Otsu thresholding method [138] is employed for dividing background and foreground since it is one of the most reliable methods to identify pixels classes within grey-scaled images. Before applying the method, a histogram of each image is recreated to understand which is the average temperature value and quantify the effect of the background on the image. The output of the Otsu technique is a single intensity threshold that separates pixels in two classes, foreground and background. To achieve such result, the method aims at minimizing the intra-class intensity variance or equivalently, maximize the inter-class variance. The former is the sum of the variances of the classes whereas the latter is the variance between two candidate classes. Therefore, it is an iterative process that starting from a suitable value of initial threshold (average temperature in the case proposed) aims at minimizing or maximizing a weight function. From a mathematical point of view, considering a histogram with L bins and an initial threshold t, the probabilities of the two classes are defined as

$$\omega_1(t) = \sum_{i=0}^{t-1} p(i), \tag{3.2}$$

$$\omega_2(t) = \sum_{i=t}^{L-1} p(i), \tag{3.3}$$

Where ω_1, ω_2 are the probabilities of the classes and $p(i)$ is the pixel intensity in the i-th location. The intra-class variance is defined as the weighted sum of the variances of the classes, expresses as

$$\sigma_\omega^2(t) = \omega_1(t)\sigma_1^2(t) + \omega_2(t)\sigma_2^2(t), \tag{3.4}$$

Where $\sigma_1^2(t)$ and $\sigma_2^2(t)$ are the variances of the two classes, weighted by the probabilities of the two. Minimizing Eq. 3.4 is the same as maximizing the following equation

$$\sigma_b^2(t) = \sigma^2 - \sigma_\omega^2(t) = \omega_1(\mu_1 - \mu_T)^2 + \omega_2(\mu_2 - \mu_T)^2 = \omega_1(t)\omega_2(t)[\mu_1(t) - \mu_2(t)]^2, \tag{3.5}$$

Which is expressed considering the class probabilities ω and the class means μ, defined as

$$\mu_1(t) = \frac{\sum_{i=0}^{t-1} ip(i)}{\omega_1(t)}, \tag{3.6}$$

$$\mu_2(t) = \frac{\sum_{i=t}^{L-1} ip(i)}{\omega_2(t)}, \tag{3.7}$$

$$\mu_T = \sum_{i=0}^{L-1} ip(i), \tag{3.8}$$

This process is computed iteratively until the optimal value of the threshold is achieved. The method can be broken down in four fundamental steps:

1. Histogram and probability distribution functions for each intensity level;

2. Select initial $\mu_i(0)$ and $\omega_i(0)$;

3. Iterative loop varying threshold value t. Two sub-step operations:
   - Update μ_i and ω_i;
   - Compute $\sigma_b^2(t)$;

4. Maximum $\sigma_b^2(t)$ leads to the threshold value t.

Once applied the Otsu method, it is possible to differentiate between background and foreground. In the case presented in the algorithm the background pixels values are set to 0, i.e. black, in order to avoid any computation on them. Therefore, an intermediate result after this stage will look like the example presented in Figure 3.10.

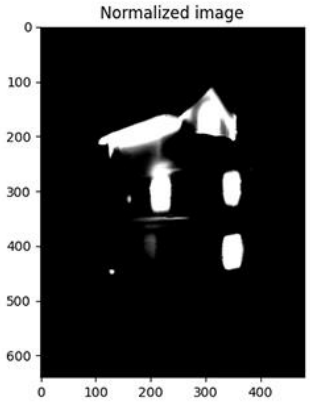

Figure 3.10 Intermediate result after Otsu's thresholding method

Given that, the image is characterized by foreground only and it is possible to proceed into the next step. To properly identify all kinds of defects, a sliding temperature window is generated, so that the algorithm can look for anomalies in different temperature ranges. In fact, each anomaly can be different in terms of thermal conductivity so once may be identified in a temperature range where another disappears. This make the algorithm iterative, proceeding to the following steps for each temperature range considered. The clue here is how to define the step size of each range and the initial and final temperature values of the detection. For what concerns the choice of maximum and minimum temperature values there are two different approaches: their values can either be chosen as the actual maximum and minimum of the grey scaled image or the choice can be guided considering a proper probabilistic distribution of the temperature. In this scenario, the second option was considered since it is not worth to investigate the entire temperature range. To set the boundaries of the algorithm, the concept of percentile must be introduced. In mathematics, it is defined as a point on a curve which corresponds to a certain percentage of the total number of observations under inspection. Provided that, a gaussian probability density function is defined considering the discrete values of temperature; then, some attempts are performed in order to understand which is a suitable percentiles' choice in order to define the best boundary values of temperature. Empirically, it was found that taking the 10^{th} percentile as minimum and the 80^{th} as maximum, the algorithm behaves in its best possibility. In fact, it is not worth to consider temperatures below and above these percentiles respectively, since the probability of founding a defect is almost none. Pixels excluded from the computation are mainly spots in sound areas that are not relevant for the algorithm.

On the other hand, the temperature step size is the only parameter decided by the final user. In fact, a narrow step increases the computational time, but it does not necessarily carry better identification since a

damage is not identified in general by a single value of temperature. On the other hand, a wide step decreases the overall computational cost of the algorithm, but the resolution of the detection is inevitably decreased. After some attempts, it was empirically found that the best temperature step ΔT for the algorithm is 2,5°C. Defined the sliding temperature window, the last computational step is to detect the contours of the defects. There are many algorithms available for edge and contour detection (see section 2.), and in the case presented the Canny method has been chosen since it is a powerful and reliable technique. The method has been already discussed in section 2.4, therefore it is only worth to recall the fundamental steps that the technique exploits to detect contours and edges:

- smoothing of the image with a proper Gaussian filter to reduce noise content;
- determine gradient magnitude and orientation for each pixel;
- detect the edge comparing magnitudes of a relevant neighborhood in a certain direction. The pixels that are not strong enough to define an edge are marked as background (non-maximum suppression operator).
- remove weak edges with double thresholding methods (hysteresis thresholding).

At this point, the contours of the remained objects on the image are characterized. An example of result using the Canny method is provided in Figure 3.11.

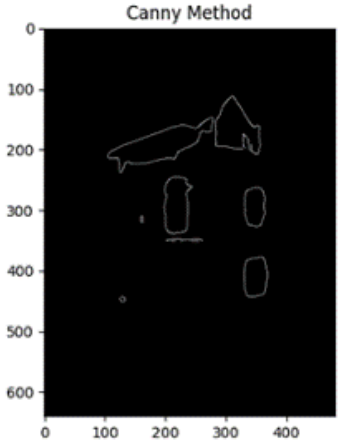

Figure 3.11 Canny method result

The last step is the definition of a criterion to define defects. In the case presented in the algorithm, a defect is defined in the image if the contours of it are closed. This means that, if the contours define a closed area, then that set of contours defines a defect. Following this criterion and avoiding multiple detection of the same defect during the detection steps, most of the defects in the images are identified. To properly visualize the results of identification, the identified contours are overlapped to the correspondent visible image in a way that the shape of the defect is highlighted even though it is not visible. In this way, the user can have a direct look about location and shape of defects in the visible image and target the inspection and maintenance in those areas that are highlighted. Table 3.2 shows a summary of the algorithm presented in this subsection, highlighting the most important steps in a pseudo-code fashion.

Table 3.2 Algorithm pseudo-code

1. Temperature values extraction from RGB image (FLIR System script);
2. Transformation of temperature matrix into a grey scaled image;
3. Characterization of the temperature histogram;
4. Local intensity weighting operator (LIW);

$$i_{out}(i,j) = \frac{\prod_{k=i-1}^{i+1} i_{in}(k,j) \prod_{h=j-1}^{j+1} i_{in}(k,h)}{\max\left(i_{in}(k,h)\right)};$$

5. Otsu thresholding method:

for i in class 1:
  for j in class 2:
    $\sigma_\omega^2(t) = \omega_i(t)\sigma_i^2(t) + \omega_j(t)\sigma_j^2(t)$;
    $t_{opt} = t : \sigma_\omega^2(t_{opt}) > \sigma_\omega^2(t), \forall$ t;
  end
end

6. Sliding temperature window definition (max, min, step size);
7. Canny method for edge detection:

for each ΔT in [min, max]:
  Gaussian filtering;
    Gradient operator;
      Non-max suppression;
        Double Thresholding;
          Final edge detection;
end

8. Defects identification;

for i in sliding window:
  for j in contours(i):
    if area_cont(j) >= area_cont(i):
      max_area = area_cont(i);
    end
  end
end

9. Superimposition of visible image and damages' contours.

Chapter IV

4. Results

The following chapter presents different results obtained in the two tests performed, along with a discussion related to the quality of the results. The first section relates to the results obtained in the first test, focusing on the reconstructions obtained using the hand-held thermal camera. The second section concerns the results of the second test, in which a UAV platform has been utilized to achieve better results in terms of both defects' detection and digital reconstruction. Finally, the last part is dedicated to the algorithm developed in Python for automatic damage detection of heat-related defects starting from thermal images, applying a cascade of image processing techniques.

4.1 Experimental results using hand-held thermal imager

The main goal of this first experimental analysis is the validation of the novel method introduced in this work. In fact, the combination of infrared thermography (IRT) and structure from motion (SfM) is something relatively new in the field of structural health monitoring since the main problem has always been the low resolution of thermal imager that most of the time made infeasible the reconstruction of a 3D model. In sight of this, thermal images fed to the SfM must be carefully pre-processed in order to guarantee an adequate reconstruction. The measure of the accuracy of the result is given by the possibility of identification of heat-related defects directly through the model. Then, also a quantitative analysis of the results obtained could be useful to practically understand the precision in the thermal reconstruction highlighting errors and significant parameters that might be useful to understand how to move forward. In this scenario, the usage of MSX images (see section 3.2) is fundamental since the thermal sensor of the FLIR ONE Pro camera has a thermal resolution of 160x120 pixels. In terms of reconstruction, this format enables to have a large number of image descriptors since the details and edges of the objects in the image are enhanced, guaranteeing a higher accuracy in the creation of 3D points starting from matches of the descriptors in different images. Provided that, the pre-processing phase follows a precise path. First, the maximum and minimum temperature's values of each image are set to the same value in order to guarantee that same defects are represented by the same set of colors. There is no precise way to decide which is the best pair of max-min that guarantees the best results, therefore it is a trial and error procedure, trying to see in which situation defects are best highlighted. In the case under analysis, their values are 54°C and 24°C respectively. The distribution of color along this 30°C of ΔT can be seen in the example of Figure 4.1.

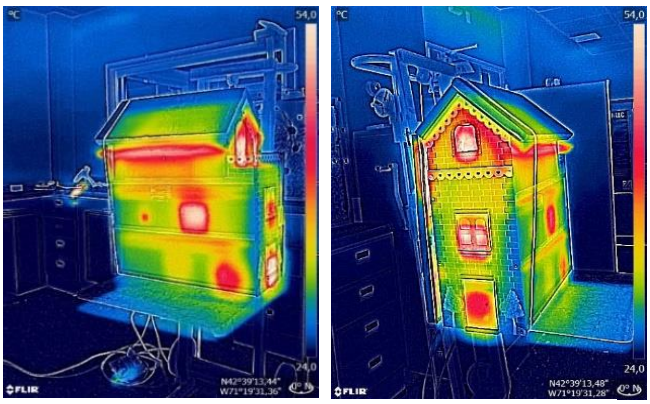

Figure 4.1 Examples of MSX images

As it is possible to notice from Figure 4.1, relevant defects are highlighted in a reasonable way, therefore it is likely possible that the reconstruction will guarantee good results. It is worth to mention that the temperature distribution, expressed by a colors' distribution can be changed but also in this case there is no best solution therefore different trials of different color's distributions (also called palettes) has been performed but for sake of brevity, only the relevant ones are presented in this section. Another important thing to notice is that in the bottom right corner of the image, the coordinates of the cameras are present, meaning that georeferencing data about the image are provided. This is for sure an advantage for the reconstruction since the knowledge of cameras' location allows to achieve better results in the estimation of the latter performed by the SfM algorithm. On the other hand, from a pure photogrammetric point of view, this is a drawback since the presence of them directly onto the image can create confusion in the definition of image descriptors. In this contest, also temperature scale and other symbols attached on top of the image such as the temperature unit or the cameras' logo, can create the same problem. To avoid this type of problem, each image has been cropped in a way that the aspect ratio of the image is the same even though the resolution is lower. In this scenario, the original image is presented as 640x480 image pixels, characterized by an aspect ratio of 1.33. Instead, the cropped images have been diminished of one fourth of the original images, both in height and width in order to maintain the same aspect ratio but eliminating the unwanted outer areas of the image that are anyway irrelevant for the reconstruction. A result of what explained so far is presented in Figure 4.2.

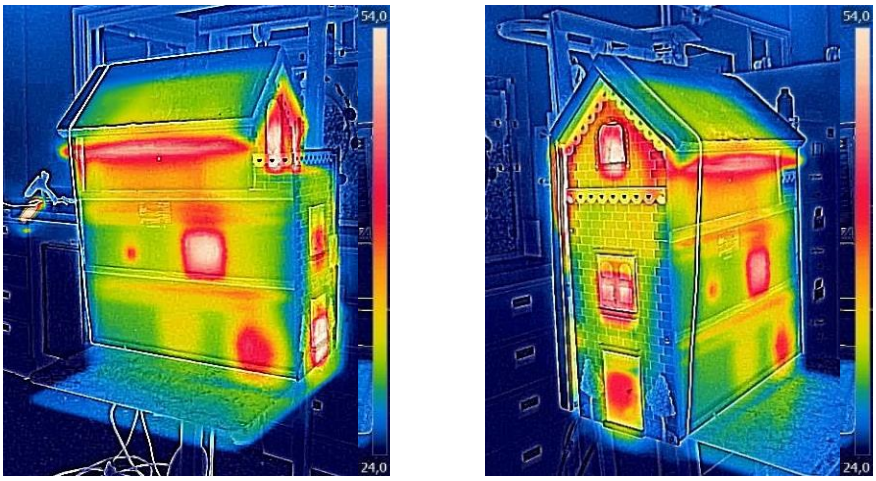

Figure 4.2 Cropped MSX image

As it is possible to notice, the possible causes of misinterpretation have been discarded, therefore Figure 4.2 shows an example of MSX image used as input for the Structure from Motion algorithm. However, this process carries an important drawback, georeferencing data are no longer available. In fact, in the process of cropping, a "new" image is created, and all the metadata related to the original one are inevitably lost. Depending on the application, this might become a relevant disadvantage. In case of large structures, the presence of locations data about the cameras can strongly increase the accuracy of the reconstruction, as well as drastically reduce the computational time. As explained in section 2.4, the bundle adjustment method is able to simultaneously estimate camera pose in the 3D virtual space and reconstruct the model. If georeferencing data about cameras' location are present, they are set to be the initial value of the estimation, therefore this phase is strongly advantaged and takes less time to be achieved. However, in the case presented in this work, the structure under inspection is relatively small compared with large infrastructures therefore georeferencing data are not so accurate since the distance between two different cameras locations is in the range of 10 cm to 20 cm. Provided that, most of the data are discarded anyway since the location appears the same. This reasoning justifies the choice of cropping the original images at the cost of losing georeferencing data. Then, real-world coordinates will be resumed using a scaling constraint in the virtual 3D model, but this will be better explained later. Moreover, a comparison between the reconstruction in the visible and thermal spectra will be provided.

It is worth to start considering the results obtained in the thermal domain. Before presenting the actual reconstruction, some intermediate achievements are worth mentioning. First, the reconstruction has been divided in two different reconstructions, one for northern and western façades (NW) and another for southern and western façades (SW). The reason behind this decision is that two of the three relevant façades are particularly similar therefore an overall reconstruction would have affected the reconstruction, confusing one with the other. Considering the northern façade reconstruction, it is possible to say that 81 thermal images where used, and that the reconstruction was able to calibrate all of them. As highlighted in Figure 4.3, the locations of the cameras with respect to the object being tested are placed in the virtual space by backtracking their locations from the extracted features. Even though images' metadata were missing due to the cropping phase, the camera locations are still adequately estimated.

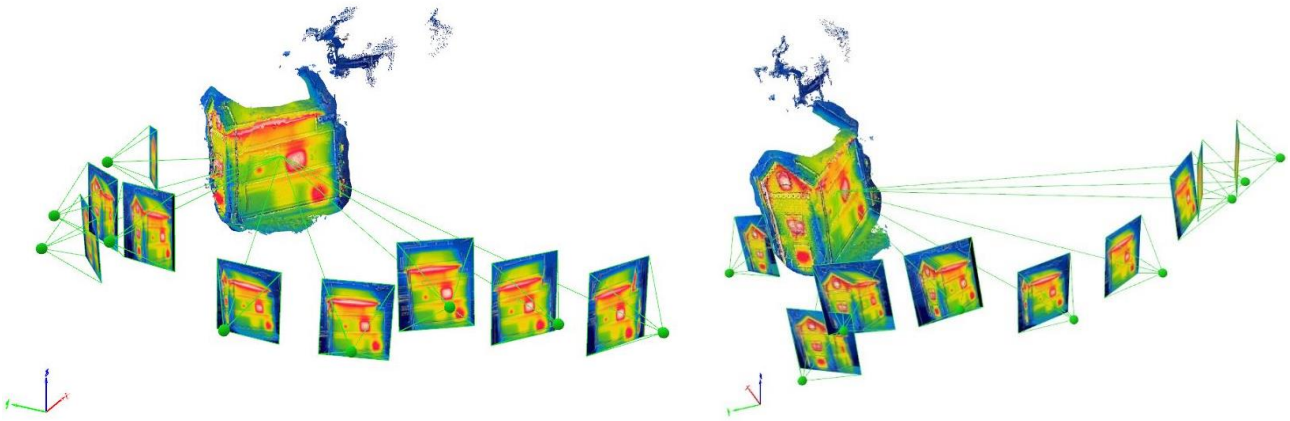

Figure 4.3 Estimated cameras' locations and 3D point reconstruction

It is also possible to notice the correspondence between 3D point and image points throughout green rays, better shown in Figure 4.4. In this example, the Figure highlights the process of formation of a 3D point in the western façade, by highlighting the corresponding point in the set of 2D images. Each matching point in the 3D space corresponds to a keypoint in an image. To avoid possible outliers in the results, the matching of at least three keypoints is necessary to create a 3D point. The presence of georeferenced data would decrease the computational time needed to generate the 3D digital reconstruction by correctly placing the set of images in the right locations and improve the camera calibration accuracy, but it is not a requirement for a successful model reconstruction. Drawbacks related to lack of georeferenced images are compensated by the MSX format that ensures details of edges and contours together with sub-surface defects characterization to be recognizable in the IR photos. To better visualize the reconstruction process, Figure 4.4 shows an example.

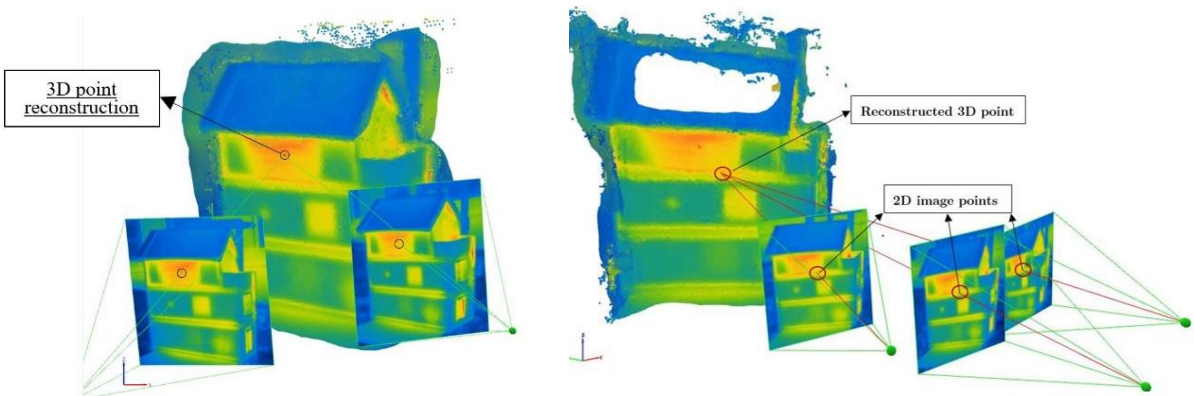

Figure 4.4 3D point reconstruction

As you can see, the rays pass through the same point both in the three images and in the 3D reconstruction, meaning that a matching has happened and that the 3D point quite represents the actual point, accepting a certain error due to computation. Once, keypoints are generated and matches are identified, tie points are created. A tie point is a point in the real scene that can be identified in two different images and that can be used as reference point in the reconstruction. In the case presented, there's a difference between tie point and 3D point since it was chosen to define a 3D point as the matching of at least three keypoints in the set of images, therefore there is a slight difference between the two categories. The choice was mainly made to guarantee a robust reconstruction of the structure being tested. To better clarify the concept, Figure 4.5 presents an example considering only tie points and one considering only 3D points forming a points cloud.

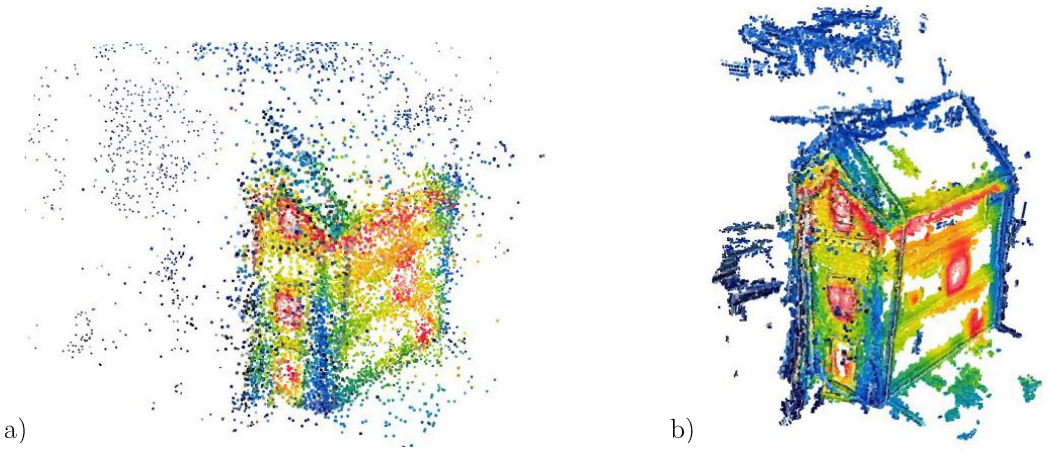

a) b)

Figure 4.5 Difference between tie points and 3D points. a) Tie points cloud; b) 3D points cloud

As it is possible to notice, the image on the left of Figure 4.5 represents the sparse distribution of tie points whereas the one on the right is the 3D points cloud obtained. The difference is quite remarkable therefore justifies the decision made in the definition of 3D point. Provided that, it is worth to highlight the most relevant parameters related to the reconstruction, in order to understand the accuracy achieved using thermal images as input set for the structure for motion algorithm. The most relevant parameters obtained from the reconstruction are presented in Table 4.1.

Table 4.1 NW reconstruction's parameters

	Keypoints per image [-]	Matches per image [-]	Keypoints for bundle adjustment [-]	3D points for bundle adjustment [-]	Mean reprojection error [pixels]
NW	4748	593.88	49915	18167	0.662

As it is possible to see, the number of matches on average is not so high considering the resolution of the image but overall, the accuracy obtained is quite acceptable, achieving a sub-pixel mean reprojection error. That is to say that the reconstruction is quite representative of the real object's shape. Along with these results, it is possible to highlight also the camera parameters that have been estimated throughout the reconstruction. The camera intrinsics parameters were provided prior to the reconstruction, therefore it is worth to mention only the extrinsic parameters uncertainties in terms of probabilistic values. After applying a scale constraint to the entire structure, it is possible to say that the estimation of the camera's parameters is quite satisfactory. This data will be further validated in the quantitative analysis, explained later in the thesis.

Being said that, it is possible to show the reconstruction obtained in this reconstruction. Figure 4.6 through 4.8 represent the reconstructed 3D model along with the triangular meshes and the 3D points cloud used for reconstruction.

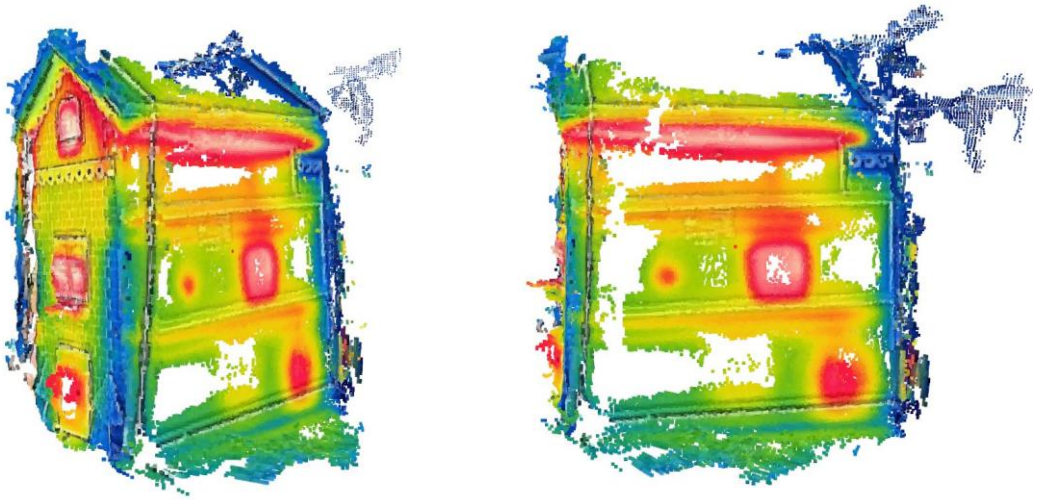

Figure 4.6 3D points cloud generation

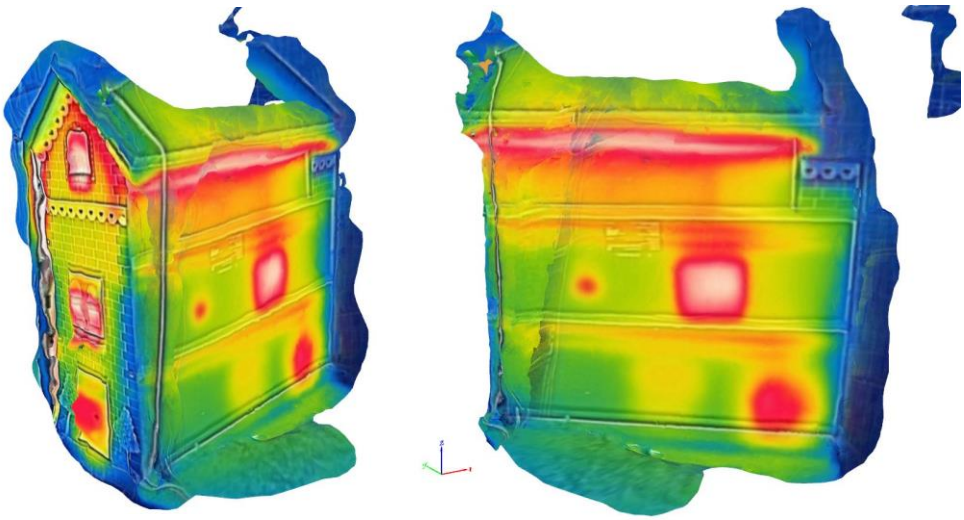

Figure 4.7 Three-dimensional model reconstruction

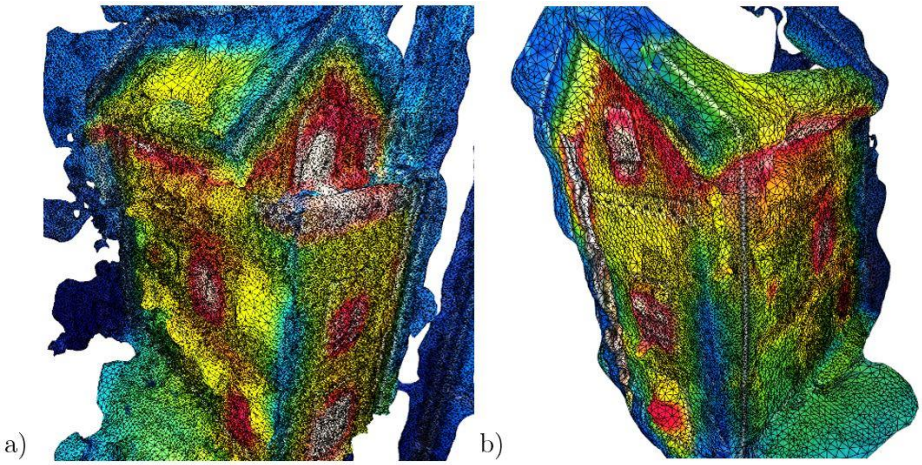

Figure 4.8 3D model triangular meshes

As it is possible to notice in Figure 4.6, once the passage between tie points and 3D points has been performed, the result is a cloud of 3D points, quite representative of the real scene. Although these are just a collection of sparse 3D points in the virtual coordinate system, it is necessary to transform them in a 3D model. To do that, different ways can be considered, depending on the type of polygon that defines the mesh used. In

the case of Pix4DMapper, the polygon used is a triangle, therefore each 3D point becomes a vertex of the aforementioned polygon, as it is possible to see in Figure 4.7, where vertexes and triangles are highlighted. In the case of the NW reconstruction, a texture of 16384x16384 pixels was generated, allowing a maximum of 5 million of triangles. By looking at the reconstructed 3D model obtained from MSX images, it is possible to identify those areas characterized by sub-surface defects and heat losses. The sources of heat loss through the envelope are highlighted by a color difference, related to the difference in temperature. In the first story, two different defects are clearly visible: the yellow rectangle in the middle representing the region with reduced-thickness insulation material and the right spot corresponding to thermal shadow of the electrical heater. On the second story, both defects related to the absence of insulation material can be identified, while on the third story, the presence of water infiltration is characterized by an orange rectangular shaped spot. Even though water infiltration is a significant defect, heat loss coming from the gap underneath the roof tends to overshadow the former due to its higher temperature. Moreover, thermal bridges between stories (i.e., distinguishable edges and yellow strips) as well as heat loss through doors and windows are clearly visible. The same reasoning can be done when considering the SW reconstruction, therefore the results are presented below. In this case 86 MSX images where used for the reconstruction and the reconstruction's parameters are presented in Table 4.2.

Table 4.2 SW reconstruction's parameters

	Keypoints per image [-]	Matches per image [-]	Keypoints for bundle adjustment [-]	3D points for bundle adjustment [-]	Mean reprojection error [pixels]
SW	5467	1433.55	119776	46163	0.799

As it is possible to see, the number of matches on average is quite high considering the resolution of the image but overall, the accuracy obtained is quite acceptable, achieving a sub-pixel mean reprojection error also in this case. That is to say that the reconstruction is representative of the real object's shape. Along with these results, it is possible to highlight also the camera extrinsic parameters. As in the first reconstruction, after the scaling of the entire model, it is possible to say that the estimation of the camera's locations is quite satisfactory. This will be further validated with the qualitative analysis. Provided that, it is worth to show the reconstruction obtained in this reconstruction. Figure 4.10 and 4.11 represents the 3D points cloud and the 3D reconstruction.

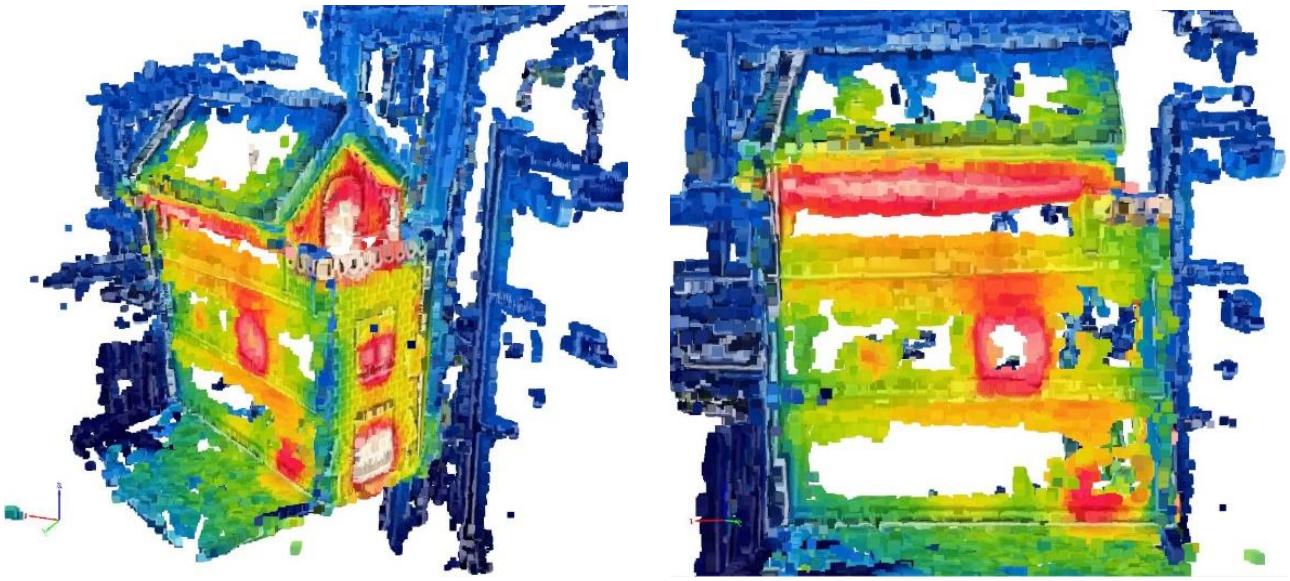

Figure 4.10 3D points cloud generation

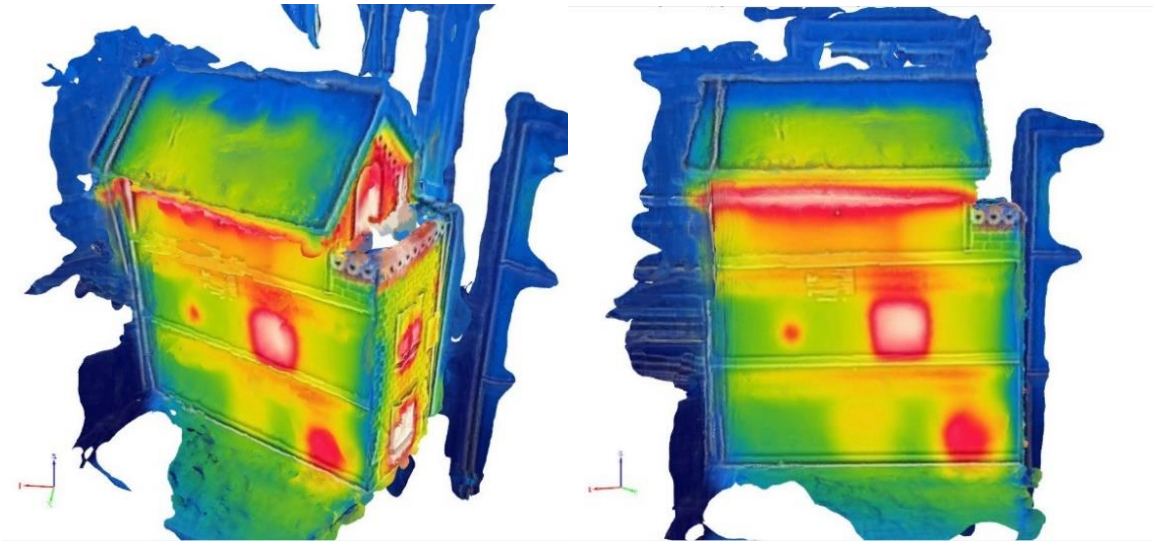

Figure 4.11 Three-dimensional model reconstruction

As it is possible to notice, the relevant heat-related defects are distinguishable, at least from a qualitative point of view. It is worth to remark that the red spot in the bottom-right part of the reconstruction is related to the presence of the electrical heaters inside the structure and therefore might be also not considered. For sake of clarity, it is worth to highlight that in this case the reconstruction of the roof has been successful even though the reprojection error is higher if compared with the NW reconstruction. The reason behind this behavior might be the usage of more images than in the previous case or the height of the camera when acquiring the set of thermal images. Finally, it must be remarked that the MSX format plays a fundamental role in the reconstruction, allowing to adequately achieve the expected results. Due to low thermal resolution of the thermal sensor being used, the reconstructions considering just thermal images are not represented in this research since the results obtained are not satisfactory. Provided a qualitative evaluation of the three-dimensional model, it is convenient to perform a quantitative analysis to understand if the reconstruction can be used to substitute the real structure.

The proposed SfM-IRT approach can be used to quantitatively assess the severity of damages relying on the possibility to measure distances, areas, surfaces, and volumes in the reconstructed 3D models. To guarantee reliable measurements it is possible to: (i) use georeferenced data of the cameras to ensure that the digital reconstruction has proper dimensions, (ii) use GCPs to scale the model to a proper coordinate system, (iii) rely on one known dimension of the structure to create a scaling constraint for the entire model. Because all the images' metadata are lost during the pre-processing steps and the use of GCPs is not useful in a closed environment like a laboratory nor relevant for small system, the third method was utilized in the case described in this research. To guarantee redundancy in scaling, two different dimensions where used to identify a proper scaling constraint. First, the width of the northern façade was used as reference, then its height was utilized as second reference to guarantee proper results. In practice, by drawing a segment in the needed direction, it is possible to set the proper distance and further increase the accuracy by checking and possibly change the locations of the segment's ends by locating them in each image. Once all the ends are in the proper position, the scaling constraint can be applied and in an automatic way the model is scaled considering the dimension used as reference. Figure 4.12 tries to explain better the concept explained so far.

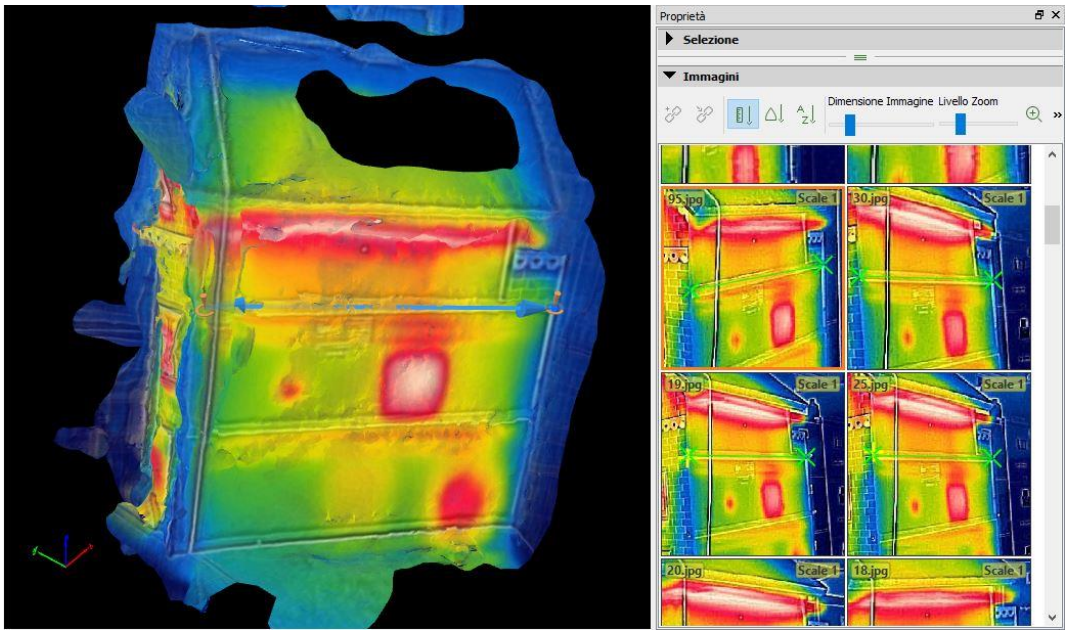

Figure 4.12 Scaling constraint application

Once defined the criterion to scale the entire model, it is possible to perform a quantitative analysis by measuring the dimensions of the defects identifiable in the model. Clearly, the shape of them is not as sharp as in a model in the visible spectrum but the results obtained are still satisfactory. Table 4.3 shows the comparison between the size of defects measured on the laboratory-scale building and those computed using the generated 3D digital model.

Table 4.3 Comparison between physical and measured dimensions of defects

Defect type	Defect area (cm^2)	Measured area (cm^2)	Error (%)
Water infiltration	300.00	278.10	-7.3
Lack of insulation (Large)	100.00	101.10	+1.1
Lack of insulation (Small)	9.00	10.16	+12.89
Reduced-thickness insulation	100.00	112.05	+12.05

As observed, the average error in the measurements is 8.33 %. Errors in measuring the surface of the defects are mainly due to low resolution of the IR camera used in the test and to misplacement of the boundaries of the polygons used to measure areas in the 3D model. Finally, it is worth to point out that the water infiltration defect is the measure characterized by the biggest error, since the presence of a gap underneath the roof creates a substantial heat loss that tends to over shade the flaw in the last story. On the other hand, defects with regular shapes can be detected with better accuracy. Overall, the obtained accuracy is good and function of the size of the defects. Nonetheless, the proposed SfM-IR approach provide a way to quantify the size of damages and sub-surface defects that result in energy loss. The final part for what concerns the first test is the reconstruction in the visible spectrum, highlighting differences with respect to the one obtained in the thermal spectrum. As discussed before, the accuracy in the visible spectrum is expected to be higher since the resolution is higher and the presence of more details in the images makes the descriptors and the keypoints powerful and higher in number. First, it is worth to give a look at the estimated cameras locations in order to understand if the reconstruction

would be satisfactory or affected by reprojections and distortions. Figure 4.13 shows the cameras location in the virtual 3D space.

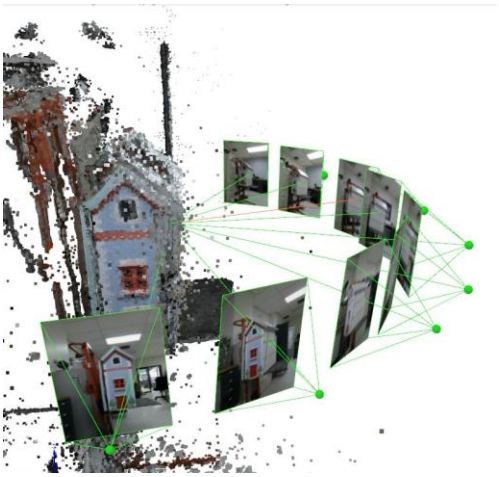

Figure 4.13 Estimated camera's locations

As it is possible to see from Figure 4.13, the estimation is quite satisfactory since the locations are representative of the ideal semi-circular path followed using the tripod and the camera. Therefore, both the reconstruction of 3D points and the camera's extrinsics parameters will be acceptable. Then, it is worth to notice that the reconstruction was carried out considering both façades together since the higher resolution of the images allows to define reliable descriptors that will not fail the reconstruction as in the thermal spectrum. For this analysis, 134 images were utilized, and the set of images still preserve all the metadata able to improve the computation. To differentiate the reconstructions, no intrinsic cameras' parameters were provided prior to computation so that it was possible to test the structure from motion algorithm accuracy achievements. In fact, there is only a 27.18 % of difference between initial and optimized internal camera parameters, a median of 19218 keypoints per image and a median of 3131.05 matches for each image considered. Comparing the results with the previous reconstruction, it is possible to say that the number of keypoint observations for bundle block adjustment is higher than the thermal reconstruction, achieving 402794 identifications, guaranteeing 161723 3D points generated. Although, the reprojection error is 0.635, slightly lower than in thermal reconstructions, meaning that even though the reconstruction is quite satisfactory, better results can be observed in the visible spectrum. Provided this overview about the numerical results of the reconstruction, a presentation of the 3D points cloud and model reconstructions is shown in Figures 4.14 and 4.15.

Figure 4.14 3D points cloud in the visible spectrum

Figure 4.15 Three-dimensional reconstruction in the visible spectrum

It is possible to notice that the 3D points cloud is dense in correspondence of the northern and southern façades, whereas the western one is not much populated. In fact, only regions near or on top of thermal bridges are highlighted. The reason behind this behavior is that there are no relevant features in between stories, being the plywood material all the same color. Although, the reconstruction is quite satisfactory since all the relevant parts are highlighted, apart for lack of points in the roof. As it is possible to see from Figure 4.15, this reconstruction has no meaning in terms of heat-related defects detection since it is not possible to detect any problem by just looking at this reconstruction. Therefore, this justifies the usage of infrared thermography in combination with structure from motion for envelope inspections of the structure. Overall, the first experiment has been satisfactory and accomplished the goal of experimentally verify the theoretical reasoning behind the usage of the new approach and provided some insights on how to improve the reconstruction phase of the method.

4.2 Experimental results using UAV platform and thermal imager

The purpose of the second set of tests was to further validate the method proposed, simulating the application of the method in a real-world scenario using an UAV platform able to scan and acquire images in larger areas. Unfortunately, due to unexpected conditions, it wasn't possible to perform the test in a real structure due to delays in the testing phase. In fact, energy audit or integrity inspections of structure or infrastructures are usually carried out in the winter season or anyway when the ambient temperature is not a factor affecting too much the results. In our case, the testing phase was shifted by two months therefore not allowing to perform an adequate passive thermography test. As explained in section 3.2, and in chapter II, the influence of external factors can alter in a consistent way the experiment, and all the attempts of investigating a real structure failed due to excessive sun radiation and high external temperature as well as unusual behavior of the building under analysis. In fact, the university building that was supposed to be examined was shut down three months before the tests, therefore neither the HVAC system nor the electrical system were functioning. Due to this combination of reasons, the decision was to reroute the experiments towards the laboratory scaled building, placing it in the middle of one of the University of Massachusetts Lowell's courtyards in order to perform a proper inspection by using a UAV platform embedded with a dual-spectrum imager. In sight of this, an active thermography test was carried out to simulate the normal behavior of a real structure. Anyway, the purpose of the test remained the same, trying to perform a better reconstruction of the structure and perform both a quantitative and qualitative analysis of fabricated defects. As for the previous section, it is worth to start considering the thermal reconstructions. In this case, an important difference is introduced with respect to the previous test. In fact, it was discovered that the MSX image format is not in general available in all thermal imagers therefore it seemed useful to carry out an analysis considering thermal images only. Even though the thermal resolution of the camera

used is higher than before, features and textures related to visible details are no longer available, creating a harsh environment for reconstructions. Being said that, the first reconstruction presented is related to the NW façades. Also in this case, the pre-processing procedure is the same applied in the previous section, losing metadata in the cropping phase, in order to perform lighter reconstructions and guarantee acceptable results. An important thing to mention is that the temperature values in this case are different from the previous one. In fact, external conditions lower the temperature values of the building, not considered in the previous case since the test was performed in a controlled environment with constant temperature and moisture content and wind absence. All this is reversed in the representation of different temperature regions, that appears with colors different from the previous experiment. Moreover, to compensate the absence of MSX images, 126 thermal images were used, almost 50% more than before. The camera intrinsic parameters were provided prior to reconstruction while the extrinsics ones were estimated. This can be further verified by looking at the estimation of camera's locations in the virtual space, as highlighted in Figure 4.16.

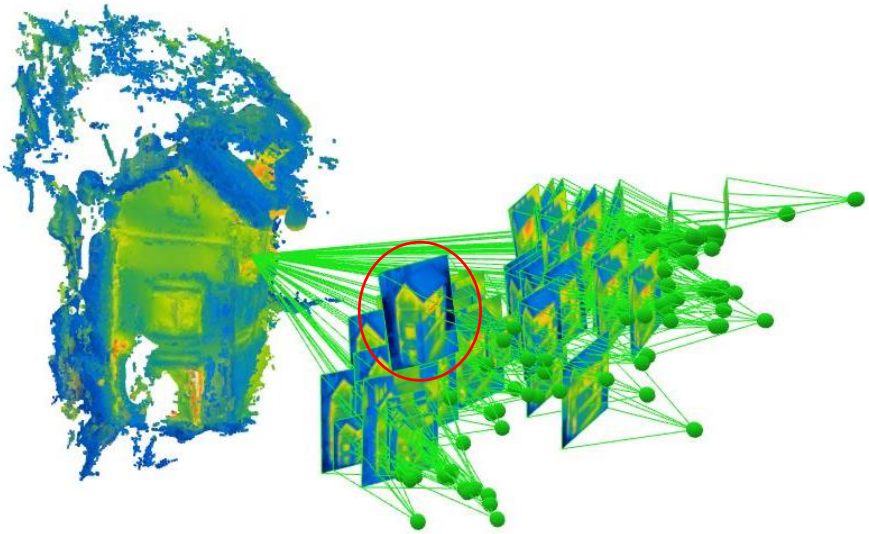

Figure 4.16 Estimated camera's locations

As it is possible to notice, the different positions of the camera seem to be placed in the right locations as it is possible to understand by looking at the image circled in red. Provided that, it is worth to look at the actual results of the reconstructions. Figures 4.17 and 4.18 present the 3D points cloud and 3D reconstruction respectively of the NW façades.

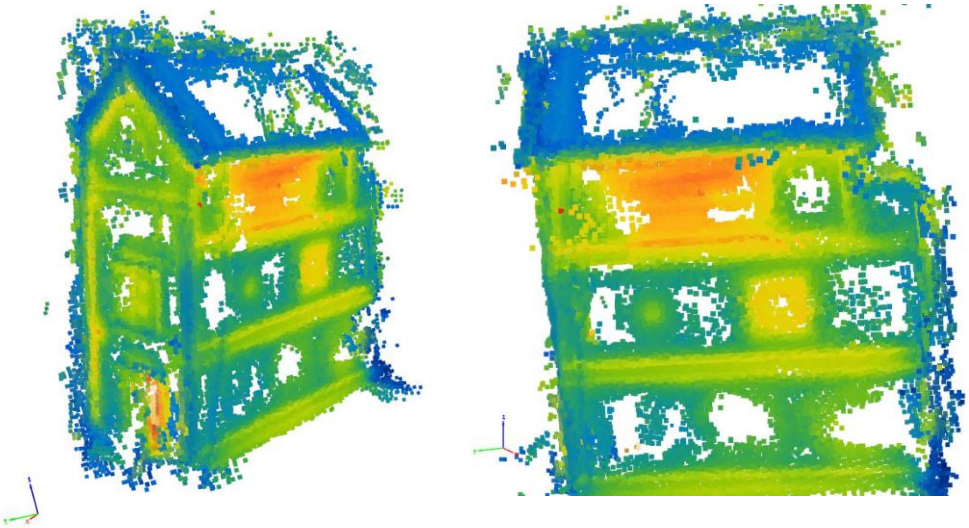

Figure 4.17 3D points cloud

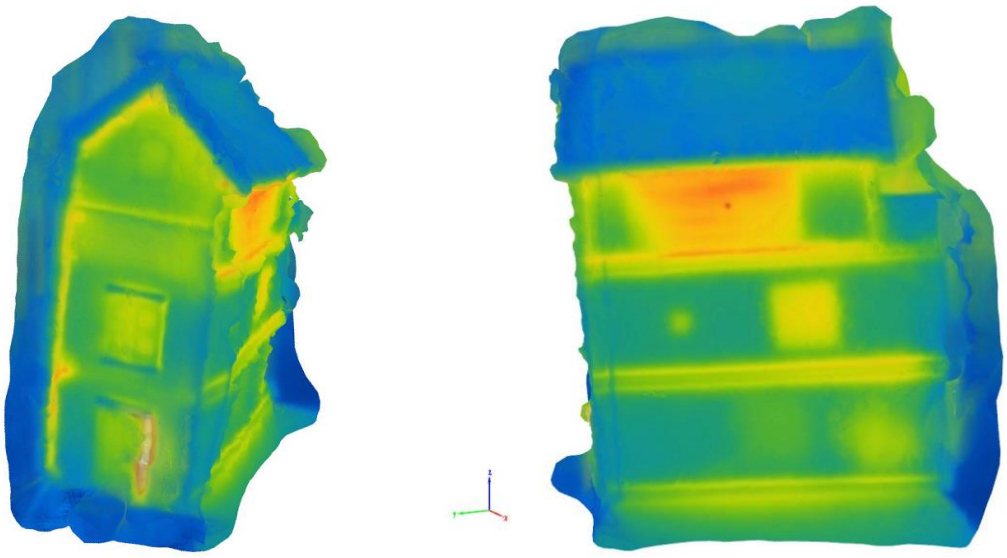

Figure 4.18 3D reconstruction

The first thing to notice in Figures 4.17 and 4.18 is the difference in color's palette with respect to the previous test. In fact, performing an outside test carries more temperature dissipations, therefore the color and consequently the temperature of damaged areas is lower than before. In any case, also in this case relevant defects are identifiable, enabling the possibility of doing a remote inspection. Namely, in the third story it is possible to highlight the presence of water dissipation as well as heat losses related to the gap underneath the roof highlighted with a yellow strip. In the same way, thermal bridges are clearly distinguishable as well as spots with lack of insulation material. In the bottom story, the presence of reduction in the insulation material is not so visible but anyways, the difference between sound areas in blue and damaged areas in green is detectable, at least from a qualitative point of view. Nonetheless, the presence of gaps both on the left side and below the roof in the northern façade are highlighted with yellow strips as well as windows and doors. Moreover, it is worth to mention that the reconstruction is done considering only thermal images therefore the result obtained can be considered acceptable. The reprojection error obtained in this reconstruction is 0.856 pixels, higher than that on the previous test but anyway achieving sub-pixel accuracy. The reason behind the increase of this value are related to the usage of thermal images rather than MSX images. Another way to achieve similar results is to change the color's palette used to represent different temperature values but the results are not uniquely better. Figure 4.19 represents a different digital reconstruction of the structure under analysis.

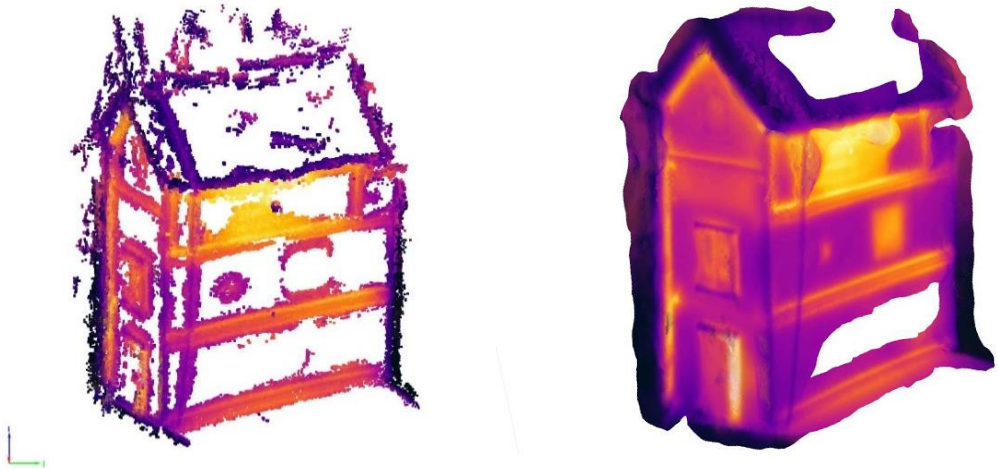

Figure 4.19 Digital reconstruction using a different color's palette

As it is possible to notice, the reconstruction seems better than the previous one even though the first story is not completely reconstructed. Therefore, on one side, some of the defects are better represented but as a drawback one of them is completely missing, due to lack of triangular meshes in the region. That is to say that the pre-processing phase in structure from motion is a fundamental step to guarantee a proper reconstruction, as well as the acquisition phase. It is also worth to mention that the results seem better than before since the thermal resolution of the infrared camera are higher than the hand-held camera used before. The exact same reasoning can be done for the SW reconstruction, where 140 thermal images were used, and two different color's palettes were utilized for the 3D model. The camera intrinsic parameters were provided prior to reconstruction while the extrinsics ones were estimated. Table 4.4 shows the relevant reconstruction's parameters obtained.

Table 4.4 SW reconstruction's relevant parameters

	Keypoints per image [-]	Matches per image [-]	Keypoints for bundle adjustment [-]	3D points for bundle adjustment [-]	Mean reprojection error [pixels]
SW	3328	742.41	93326	36507	0.88

As it is possible to notice, a sub-pixel accuracy is obtained. Figure 4.20 through 4.22 highlight the 3D points cloud, the triangular meshes and the digital reconstruction obtained in the reconstruction respectively.

Figure 4.20 3D points cloud

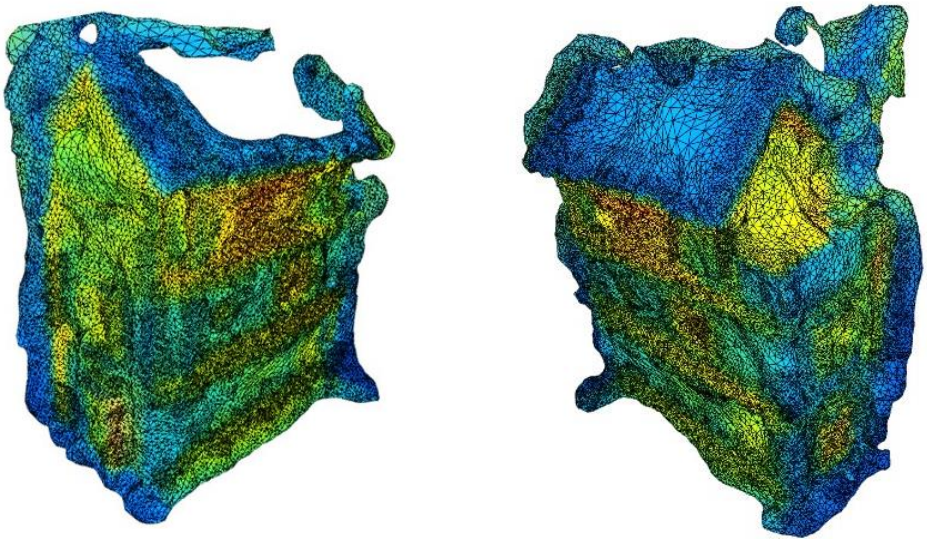

Figure 4.21 Triangular meshes

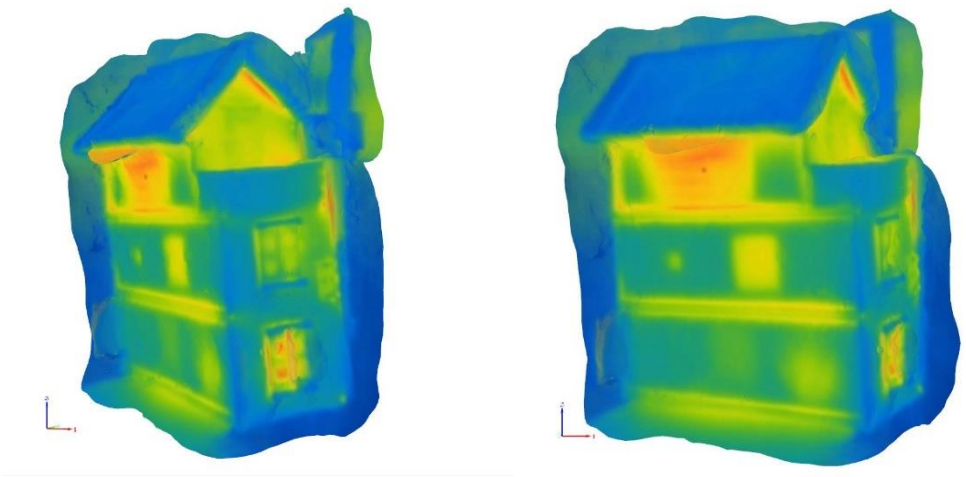

Figure 4.22 Digital 3D reconstruction

By looking at the Figures above, it is possible to detect all the relevant fabricated defects present in the structure, as well as structural components such as thermal bridges. Overall, the results obtained are satisfactory in terms of validation of the method proposed. In fact, in all the cases it was possible to identify the presence of defects in the structure in a clear way, meaning that the digital 3D reconstruction could be used as substitution of the original construction under inspection, enabling a remote inspection that clearly is a benefit in a different variety of applications. Provided that, the qualitative detection phase of the second test is terminated. The last part related to the infrared inspection is a quantitative analysis of heat-related defects, trying to understand the accuracy of the model reconstructed. The scaling method utilized is the same as in the previous case therefore it will be omitted in this section. After scaling the entire structure, it is possible to measure dimensions and areas of the defects present in the structure. Table 4.5 summarized the outcome of this phase.

Table 4.5 Comparison between measured and physical defect's dimensions

Defect type	Defect area (cm^2)	Measured area (cm^2)	Error (%)
Water infiltration	300.00	310.08	+ 3.36
Lack of insulation (Large)	100.00	95.68	- 4.32
Lack of insulation (Small)	9.00	9.54	+ 6
Reduced-thickness insulation	100.00	100.82	+ 0.82

As it is possible to notice, the dimensions measured in the digital model do not differ to much from real ones, achieving an average error of 3.625%. The anomaly with the higher error is the small lack of insulation in the second story, meaning that small areas are more affected by the accumulation of errors in the reconstruction. This analysis explains that a good accuracy in the digital reconstruction can be obtained and that the model is a reliable substitute of the real structure. Nonetheless, it is true that the dimensions of the structure analyzed are small compared to real-world structure, therefore the influence of thermal resolution is not so disadvantageous. In real-world scenarios, the situation is different since the effect of spatial resolution of the thermal sensor plays a crucial role and therefore a careful and accurate planning of the inspection from a photogrammetric point of view must be performed in order to obtain better results. Not so much work has been done towards this direction, therefore this could be a possible future goal to continue this research. The last part of this section is related to the reconstruction in the visible spectrum, used as comparison with the thermal analysis. In this case, it is possible to expect a very accurate digital reconstruction since the camera used has a high resolution (12 Megapixels), and

the path followed is the same as the thermal acquisition, providing more than adequate overlap, both in lateral and frontal directions. First, it is worth to start considering the estimation of the camera's locations. As for the previous visible test, no data about camera's intrinsic and extrinsic parameters is provided, allowing to understand the accuracy of the reconstruction. Figure 4.23 presents the estimated cameras locations along with the rays between matched images.

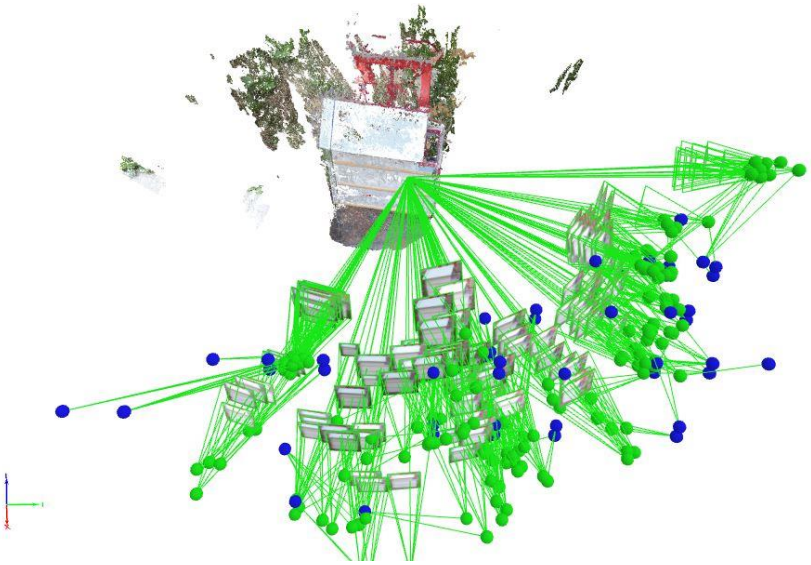

Figure 4.23 Estimated camera's locations and links between matched images

As it is possible to notice, the locations are well estimated, and the path followed in the acquisition is adequately represented. Figure 4.23 represents the estimated camera's locations computed by the bundle adjustment method. As it is possible to notice, the latter set is quite representative of the actual acquisition plane used in the test. On the other hand, the relevant parameters of the reconstruction are represented in Table 4.6.

Table 4.6 Visible reconstruction relevant parameters

	Keypoints per image [-]	Matches per image [-]	Keypoints for bundle adjustment [-]	3D points for bundle adjustment [-]	Mean reproj. error [pixels]
Visible sim.	20886	11162.7	1306096	310671	0.226

As it is possible to notice, the estimation is accurate in the visible spectrum when compared with the previous thermal reconstructions. This is to stress the fact that the reconstruction in the visible spectrum is always going to be better than the one in the infrared field since the set of images are more detailed and the resolution of the sensors used is consistently high. Moreover, in visible images, all the metadata of the image are available for the computation, such as georeferencing data, strongly increasing the accuracy of the digital reconstruction. Provided all these numerical data, Figures 4.24 and 4.25 show the 3D points cloud and the digital reconstruction in the visible domain.

Figure 4.24 3D points cloud

Figure 4.25 Digital three-dimensional reconstruction

It is clearly possible to notice the high accuracy of the reconstruction, able to reconstruct an almost identical digital model of the structure under inspection. On the other hand, no defects are identifiable since they are only related to heat dissipation or moisture problems.

4.3 Automatic damage detection of defected areas

The last section of the proposed work concerns an algorithm for automatic detection of defects starting from thermal images. The latter was developed in Python language and it is divided in three main scripts. First, the script for extracting metadata information about thermal images. In fact, it is useful to have an image representative of temperature values rather than an equivalent RGB image where colors substitute temperature values. Therefore, the first script is related to the pre-processing of the set of images. Then, there is the defect detector script where a cascade of different image processing techniques is utilized, as explained in section 3.3. The most important one is the last one, also called "main" script in computer science language, that is the script in which the classes and methods created in the other two are recalled and the actual detection is performed. The outcome of the algorithm is the superimposition of the original RGB image in the visible spectrum with the defect's contours, in order to directly visualize damaged regions in the structure. Apart from that, there are also

intermediate results that it is worth to mention. Therefore, the current section is dedicated to the results related to the developed algorithm, presenting few representative examples, along with a brief discussion of the achievements and improvements of the algorithm. As mentioned in section 3.3 the proposed algorithm has been tested both in laboratory experiments and in real case scenarios. For the lab experiments the damages are segmented, and the contours detected, while for images related to the real case scenario, no segmentation is performed since the shape of the defects is irregular. It is important to notice that the result can be very influenced by the choice of few parameters. First, after modelling the temperature histogram in the image as a combination of gaussian probability functions, two percentiles must be set, and damages will be sought in the range selected. This stage of the algorithm helps discarding possible outlier values that hold in the tails of the gaussian distribution. There is no literature about this process, therefore the technique used to achieve the best results is a trial and error procedure. Empirically, the best results are achieved considering temperature values in between the 10th percentile and the 80th percentile. To better understand the concept explained so far, Figure 4.26 presents an example of temperature histogram, highlighting the boundaries of the computation, along with a thermal image where the difference between damaged and sound areas is numerically highlighted.

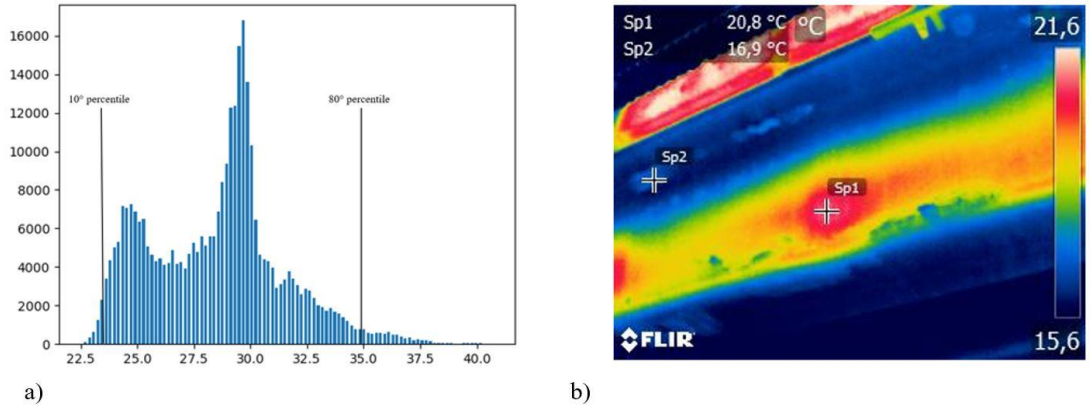

Figure 4.26 Temperature results. a) Temperature histogram distribution. The 10th and the 80th percentiles are marked; b) temperatures of two defects in a bridge. The first at 16.9° C the latter at 20.8° C.

As it is possible to notice from Figure 4.26 b, the analysis of very low temperature values is not worth it since it is unlikely to find a defect in that region. On the other hand, too high temperature values are useless too for the algorithm since defects will be found at a relatively lower temperature. Considering the maximum temperature value as upper boundary for the algorithm will only increase the computational time needed for the detection. Another important parameter to set is the range of the sliding window. In fact, different anomalies can be detected considering different temperature ranges. This means that each time the algorithm will look for flaws among those pixels in the given temperature range, then the window slides and the process is repeated. According to the tests performed in this research, most of the defects can be isolated considering a window's size of 2,5°÷3° Celsius. Provided that, the first intermediate result is the conversion of RGB images into grey-scaled images where the pixels' intensity is equal to the actual temperature. Figure 4.27 presents some examples of grey-scaled images converted.

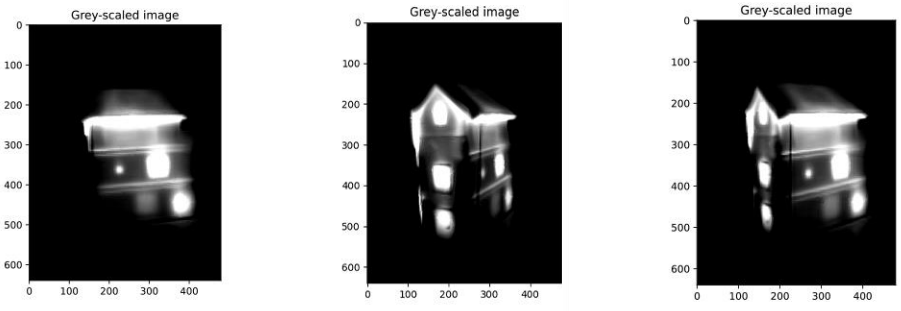

Figure 4.27 Outcome after grey-scaling temperature values

As it is possible to notice, relevant details of the structure are highlighted, allowing a better detection of possible anomalies. In this contest, the background appears darker than the rest of the image simply because the structure is heated and there is an important temperature difference with respect to its surroundings. Once obtained this result, the next step is the computation of the LIW operator, as explained in section 3.3, in which a local neighborhood operator is applied in order to better visualize those areas that are bright in the image. Figure 4.28 presents some examples of the application of such operator.

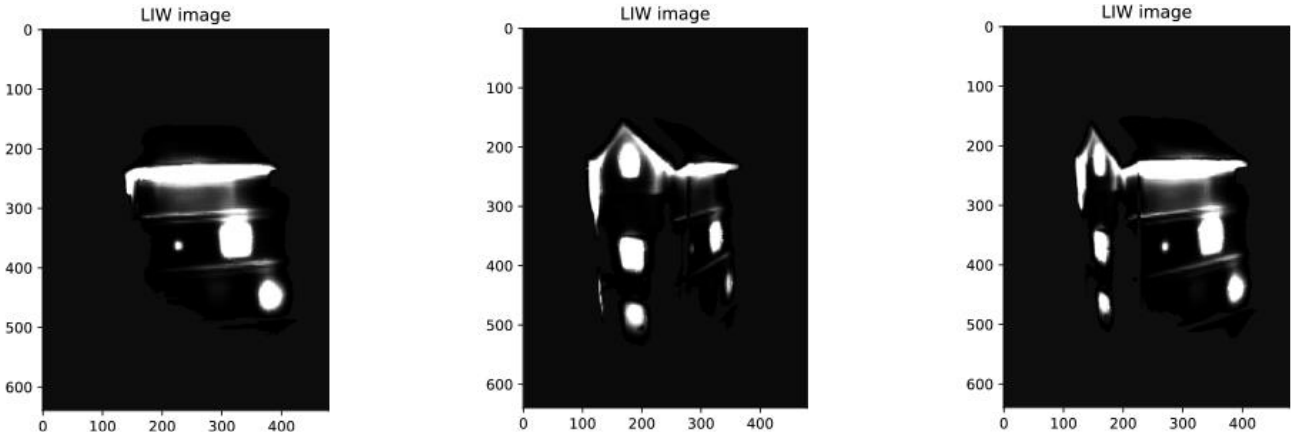

Figure 4.28 Examples of LIW operator applications

As it is possible to highlight, comparing Figure 4.28 and 4.27, no change in the background is achieved since the neighbor operator has no effect in regions in which there is no sharp temperature's gradient. Instead, by looking at the structure, it is possible to notice that the actual defects or source of heat loss such as windows and doors are better highlighted whereas grey regions that are not relevant for the analysis are discarded. In general, this is advantageous for computation and detection, but it is likely possible to discard those areas that are not characterized by strong temperature's gradients, thus discarding some possible moderate flaws. The following step is the application of the Otsu thresholding method, in order to separate background and foreground. The whole point is to discard the background so that the computation is lighter and the possibility of having outliers in the results is lower. Figure 4.29 presents some examples of the Otsu method application.

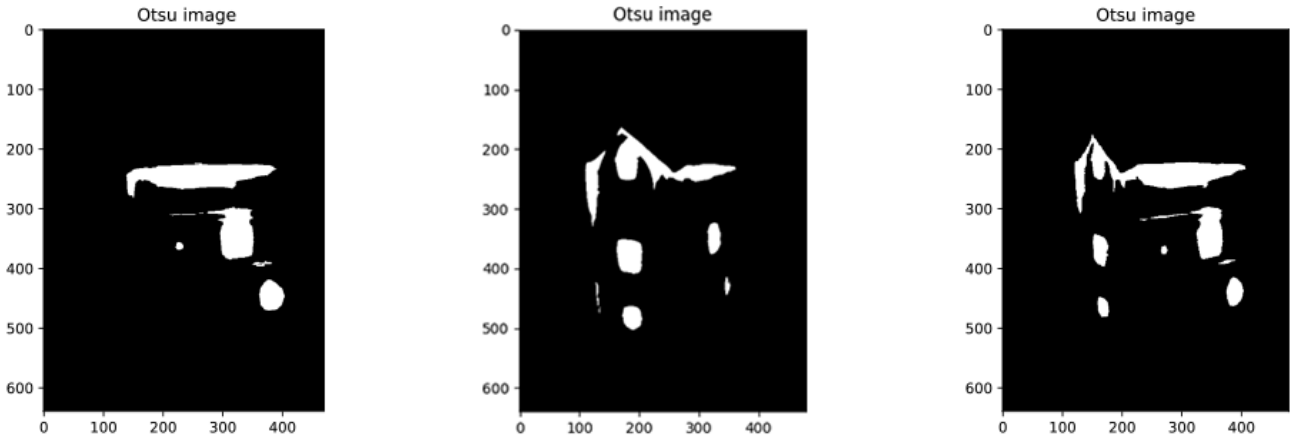

Figure 4.29 Examples of Otsu method applications

As it is possible to notice from Figure 4.29, the principal sources of heat losses are well highlighted, and the following step of detection should be easier than before. The relevant part of the algorithm is the Canny edge detector method in which all the contours of the image given in input are detected. Although this is a powerful method, it does not provide a criterion to identify defects. In fact, it only relates to contours, regardless from the nature of the objects in the images. Figure 4.30 presents some examples of the result of the application of the Canny method.

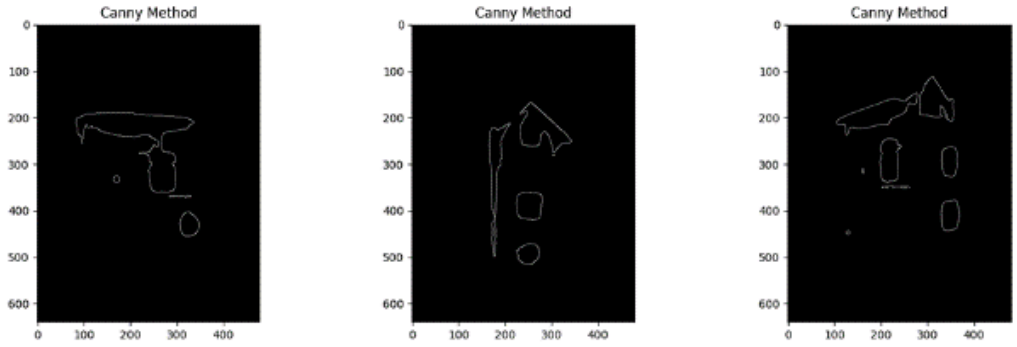

Figure 4.30 Canny method application

As it is possible to see in Figure 4.30, the most relevant contours are detected, guaranteeing reliable results in the final detection. The last part of the algorithm is probably the most important one. In fact, once defined the contours of the image, a criterion to classify defects must be provided. This is not so easy having just geometrical properties or temperature values since heat-related defects can be of any shape and can be characterized by different temperature values. Moreover, the algorithm is computed each step size of the temperature window therefore in each step a set of contours will be provided. No literature is present towards this direction since the task is very difficult, given the variety of possible defects. Therefore, the presence or absence of defects is distinguished considering areas values. First, only those contours that describe a closed area are kept and then for each temperature window, only the contours that define the maximum area are considered. In this way, for each step, the larger contours will be kept, and the outcome is a combination of defects identified in all the different temperature windows. Figure 4.31 through 4.33 present examples of possible outcome of the algorithm.

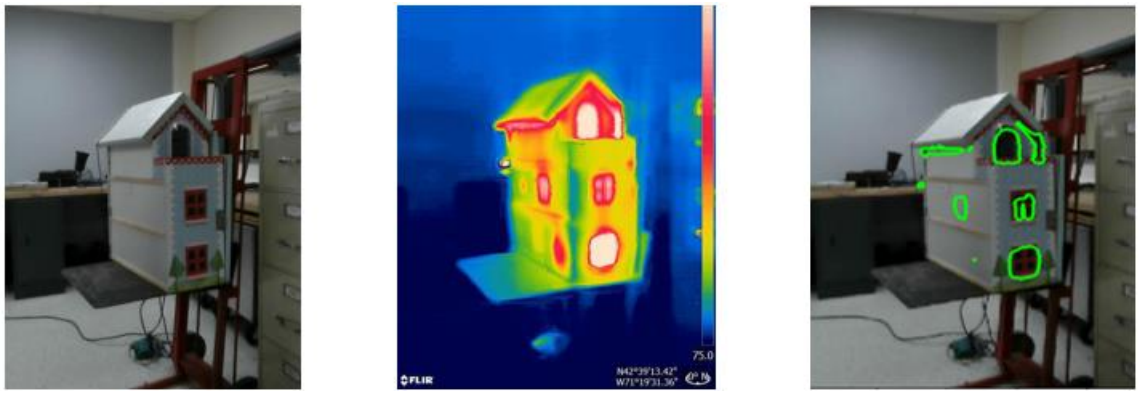

Figure 4.31 Algorithm results from thermal images of the first test

Figure 4.32 Algorithm results from thermal images of the second test

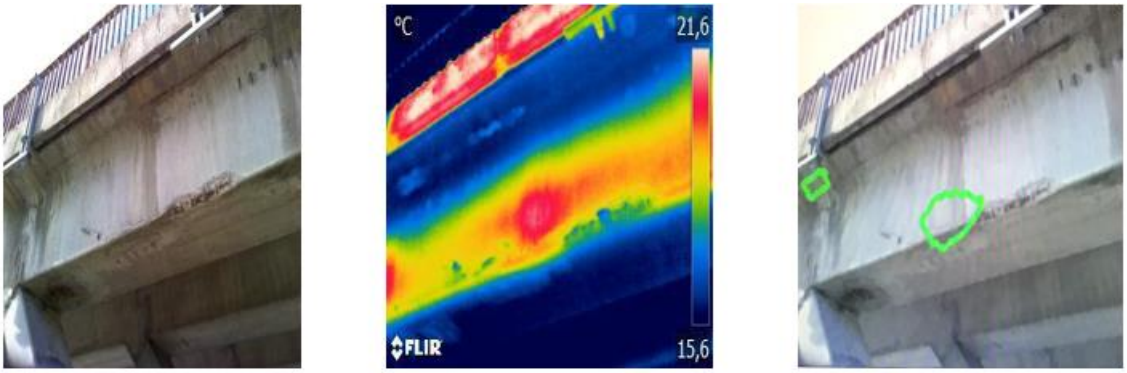

Figure 4.33 Algorithm results from thermal images of a real bridge

As it's possible to observe in the Figures, the best results in term of accuracy, are obtained with the FLIR ONE PRO camera, Figure 4.31, where the algorithm has been trained the most, but the detection works well also with other camera's models. The algorithm can easily identify all the damages in the laboratory-scaled structure, such as lack of isolation and heat losses. Instead for the real cases only the bigger damages can be spotted. This is mainly because in the laboratory experiment the thermal difference between sound and damaged parts is much higher than in real cases. This result further motivates the choice of active thermography for conducting experiments on the structure. In general, heat losses in buildings, especially during wintertime, produce higher thermal gaps which makes the damage easier to detect. Instead, water infiltrations and delaminations create a smaller thermal gap that leads to a more difficult detection. In this regard, it's extremely important to choose the best time for an infrared inspection. Usually, thermal gaps are highly detectable one hour after sunrise and one hour after sunset, so this should be the most appropriate moment for performing an infrared thermography audit.

Chapter V

5. Conclusions

The work presented in this research aimed at developing a novel method to virtually assess heat losses and sub-surface defects in structures and infrastructures. The final goal was to obtain an automated, reliable system to evaluate heat-related defects, that most of the times are sub-superficial, thus not detectable with visual inspection techniques or tools in the visible spectrum. The novel method relies on two different methodologies, often used alone. Infrared thermography (IRT) is a well-known nondestructive methodology that allows to identify possible structural damages related to heat loss, whereas Structure from Motion (SfM) aims at reconstructing a three-dimensional (3D) digital model starting from a suitable set of camera's images. This research combines the two methodologies, directly reconstructing a model of the structure being tested, starting from a set of IR images. This new method guarantees a nondestructive evaluation and structural inspection, applicable in all those fields where heat loss constitutes a major issue. The feasibility of the proposed IR-SfM method has been validated through two tests performed on a laboratory-scale model of a three-story building where different types of defects where fabricated and identified. Both tests simulated an energy audit inspection where the structure was heated up from inside and IR images are captured to detect thermal fluxes characteristics of structural discontinuities. By acquiring a suitable set of thermal images, it is possible to exploit the SfM methodology to reconstruct a high-resolution, 3D thermal model of the structure being tested that can be remotely inspected to assess sub-surface defects that may lead to heat loss. During the first test, a hand-held camera was used to validate the proposed approach and quantifying the size of fabricated defects, obtaining a reprojection error of 8.33%. On the other hand, in the second test, the inspection was repeated using an unmanned aerial vehicle (UAV) equipped with a high-resolution IR camera. The results of the tests showed that the proposed SfM-IR-UAV system is capable of identifying the presence of sub-surface defects and quantify their dimensions with an error below 4%.

Finally, this research investigated the possibility to automate the detection of anomalies with an algorithm capable of identifying defects from IR images. The algorithm can work with different infrared cameras and can isolate damages also in real case scenarios. The overall result of the detection strongly depends on the goodness of IR measurements. However, some flaws are detected with more accuracy than others, such as water infiltrations. If further developed, this approach can really start a path in the way thermal losses in structures and infrastructures are assessed and quantified. The involvement of an aerial platform allows to set up an inspection in any possible environmental condition, guaranteeing a 3D virtual model to remotely inspect the conditions of the targeted construction. The 3D thermal model can illustrate the locations of significant thermal loss along with the detection of sub-surface defects. An important thing to say is that the approach has been tested only in a laboratory-scaled structure therefore further tests in real-case scenarios must be done to fully verify this new methodology. The relevant disadvantage of testing large structures is that the spatial resolution of the thermal cameras is low, therefore the possibility of having worse results is high. To avoid such behavior, future tests would have to be carefully planned from a photogrammetric point of view, allowing to reach similar results as the one obtained in this work, considering larger structures. For further analysis in this scenario, it could be also possible to use the locations about the cameras both in the infrared and visible spectrum in order to guarantee a much reliable and denser 3D points cloud and then perform the digital reconstruction in the visible spectrum, overlaying to it the texture of the infrared spectrum so that the accuracy of the model is high and the infrared information are still available.

On the other hand, the automated detection of damages by means of image-based algorithms can be improved and further developed by using machine learning or deep learning techniques such as convolutional neural networks (CNNs) to automatically evaluate the state of target objects directly by processing information from the set of images acquired with the thermal camera. Another improvement of the aforementioned algorithm could be to use directly the reconstructed 3D model to automatically detect the presence of defects. For instance, this could be done by acquiring a video of the three-dimensional digital reconstruction while moving around it and isolating relevant frames. These frames can then be used as the new set to input in the image-based algorithm, allowing to completely work with the digital reconstruction of the model rather than with the actual structure.

Overall, the results obtained in this preliminary work are quite satisfactory, therefore further research towards this direction will follow, trying to improve all the steps that lead to the final outcome of this proposed new methodology.

References

[1] EIA, “International Energy Outlook 2016-Buildings sector energy consumption - Energy Information Administration,” 2016. [Online]. Available: https://www.eia.gov/forecasts/ieo/buildings.cfm.

[2] P. H. Shaikh, N. B. M. Nor, P. Nallagownden, I. Elamvazuthi, and T. Ibrahim, “A review on optimized control systems for building energy and comfort management of smart sustainable buildings,” *Renew. Sustain. Energy Rev.*, vol. 34, pp. 409–429, 2014, doi: 10.1016/j.rser.2014.03.027.

[3] E. Commission, “Energy use in buildigns,” 2016. [Online]. Available: https://ec.europa.eu/energy/eu-buildings-factsheets-topics-tree/energy-use-buildings_en.

[4] E. Pujadas-Gispert, C. C. Korevaar, M. Alsailani, and S. P. G. Moonen, “Linking constructive and energy innovations for a net zero-energy building,” *J. Green Build.* , vol. 15, no. 1, pp. 153–184, 2020, doi: https://doi.org/10.3992/1943-4618.15.1.153.

[5] L. De Boeck, S. Verbeke, A. Audenaert, and L. De Mesmaeker, “Improving the energy performance of residential buildings : A literature review,” vol. 52, pp. 960–975, 2015, doi: 10.1016/j.rser.2015.07.037.

[6] T. Schuetze, “Zero Emission Buildings in Korea—History, Status Quo, and Future Prospects,” pp. 2745–2767, 2015, doi: 10.3390/su7032745.

[7] D. Zanni, A. Righi, T. Dalla Mora, F. Peron, and P. Romagnoni, “The Energy improvement of school buildings: Analysis and proposals for action,” *Energy Procedia*, vol. 82, no. February 2016, pp. 526–532, 2015, doi: 10.1016/j.egypro.2015.11.865.

[8] L. Yang, H. Yan, and J. C. Lam, “Thermal comfort and building energy consumption implications â{\texteuro}{\textquotedblleft} A review,” *Appl. Energy*, vol. 115, no. C, pp. 164–173, 2014.

[9] M. Babenko *et al.*, “the Main Insulation Parameters for the Design of Nzeb From Biosourced Materials,” no. July, 2017.

[10] J. Lojda, “Building defects as a result of non-conceptual design,” *MATEC Web Conf.*, vol. 279, p. 01007, 2019, doi: 10.1051/matecconf/201927901007.

[11] S. Yacob, A. S. Ali, and C. P. Au-Yong, “Establishing Relationship Between Factors Affecting Building Defects and Building Condition,” *J. Surv. Constr. Prop.*, vol. 10, no. 1, pp. 31–41, 2019, doi: 10.22452/jscp.vol10no1.3.

[12] N. L. Othman, M. Jaafar, W. M. W. Harun, and F. Ibrahim, “A Case Study on Moisture Problems and Building Defects,” *Procedia - Soc. Behav. Sci.*, vol. 170, no. January, pp. 27–36, 2015, doi: 10.1016/j.sbspro.2015.01.011.

[13] N. N. O. Bakri and M. A. O. Mydin, “General Building Defects: Causes, Symptoms and Remedial Work,” *Eur. J. Technol. Des.*, vol. 3, no. 1, pp. 4–17, 2014, doi: 10.13187/ejtd.2014.3.4.

[14] M. Jolly *et al.*, “Review of Non-destructive Testing (NDT) Techniques and their Applicability to Thick Walled Composites,” *Procedia CIRP*, vol. 38, pp. 129–136, 2015, doi: 10.1016/j.procir.2015.07.043.

[15] D. M. McCann and M. C. Forde, “Review of NDT methods in the assessment of concrete and masonry structures,” *NDT E Int.*, vol. 34, no. 2, pp. 71–84, 2001, doi: 10.1016/S0963-8695(00)00032-3.

[16] A. Kroworz and A. Katunin, “Non-destructive testing of structures using optical and other methods: A review,” *SDHM Struct. Durab. Heal. Monit.*, vol. 12, no. 1, pp. 1–17, 2018, doi: 10.3970/sdhm.2018.012.001.

[17] S. Gholizadeh, “A review of non-destructive testing methods of composite materials,” *Procedia Struct. Integr.*, vol. 1, no. October, pp. 50–57, 2016, doi: 10.1016/j.prostr.2016.02.008.

[18] A. Lewis, G. E. Hilley, and J. L. Lewicki, “Integrated thermal infrared imaging and structure-from-motion photogrammetry to map apparent temperature and radiant hydrothermal heat flux at Mammoth Mountain, CA, USA,” *J. Volcanol. Geotherm. Res.*, vol. 303, pp. 16–24, 2015, doi: 10.1016/j.jvolgeores.2015.07.025.

[19] W. H. Maes, A. R. Huete, and K. Steppe, "Optimizing the Processing of UAV-Based Thermal Imagery," 2017, doi: 10.3390/rs9050476.

[20] S. Sensors, M. Yang, T. Su, and H. Lin, "Fusion of Infrared Thermal Image and Visible Image for 3D Thermal Model Reconstruction Using," 2018, doi: 10.3390/s18072003.

[21] A. Sabato, M. Puliti, and C. Niezrecki, "Combined infrared imaging and structure from motion approach for building thermal energy efficiency and damage assessment," vol. 1138125, no. April, p. 86, 2020, doi: 10.1117/12.2558796.

[22] T. Rakha and A. Gorodetsky, "Automation in Construction Review of Unmanned Aerial System (UAS) applications in the built environment : Towards automated building inspection procedures using drones," *Autom. Constr.*, vol. 93, no. January, pp. 252–264, 2018, doi: 10.1016/j.autcon.2018.05.002.

[23] K. Willis, H.H., and Loa, "Measuring the Resilience of Energy Distribution Systems, RAND Corporation: May 2015," 2020.

[24] Y. Y. Haimes, "On the definition of resilience in systems," *Risk Analysis*. 2009, doi: 10.1111/j.1539-6924.2009.01216.x.

[25] R. Talib, A. G. Ahmad, N. Zakaria, and M. Z. Sulieman, "Assessment of Factors Affecting Building Maintenance and Defects of Public Buildings in Penang , Malaysia," vol. 4, no. 2, pp. 48–53, 2014, doi: 10.5923/j.arch.20140402.03.

[26] N. Ahzahar, N. A. Karim, S. H. Hassan, and J. Eman, "Procedia Engineering The 2 nd International Building Control Conference 2011 A Study of Contribution Factors to Building Failures and Defects in Construction Industry," *Procedia Eng.*, vol. 20, pp. 249–255, 2011, doi: 10.1016/j.proeng.2011.11.162.

[27] J. Hinks and G. Cook, *The technology of building defects*. 2002.

[28] Z. Zhou, G. Sun, and B. I. Science, "Application of Laser Ultrasonic Technology for Nondestructive Testing of Application of Laser Ultrasonic Technology for Nondestructive Testing of Aerospace Composites," no. April, 2016.

[29] E. R. Fotsing, A. Ross, and E. Ruiz, "NDT & E International Characterization of surface defects on composite sandwich materials based on de fl ectrometry," *NDT E Int.*, vol. 62, pp. 29–39, 2014, doi: 10.1016/j.ndteint.2013.11.004.

[30] C. Meola, "applied sciences Nondestructive Testing in Composite Materials," 2020.

[31] V. P. Vavilov, O. N. Budadin, and A. A. Kulkov, "Infrared thermographic evaluation of large composite grid parts subjected to axial loading," *Polym. Test.*, vol. 41, pp. 55–62, 2015, doi: 10.1016/j.polymertesting.2014.10.010.

[32] "First European-American Workshop of Reliability," 1997. [Online]. Available: https://www.ndt.net/publicat/bibliog/euam97.htm.

[33] AGARD Lecture Series 190, "A recommended methodology to quantify NDE/NDI based on aircraft engine experience," 1993.

[34] A. P. Berens, "NDE reliability data analysis," *ASM Handbook.*, 1989.

[35] G. A. Georgiou, "Probability of Detection (PoD) curves: Derivation, applications and limitations," *Insight - Non-Destructive Testing and Condition Monitoring*, 2007.

[36] L. Goglio and M. Rossetto, "Ultrasonic testing of adhesive bonds of thin metal sheets," *NDT E Int.*, vol. 32, no. 6, pp. 323–331, 1999, doi: 10.1016/S0963-8695(98)00076-0.

[37] N. Athi, S. R. Wylie, J. D. Cullen, A. I. Al-Shamma'a, and T. Sun, "Ultrasonic non-destructive evaluation for spot welding in the automotive industry," *Proc. IEEE Sensors*, pp. 1518–1523, 2009, doi: 10.1109/ICSENS.2009.5398469.

[38] D. E. W. Stone and B. Clarke, "Ultrasonic attenuation as a measure of void content in carbon-fibre reinforced plastics," *Non-Destructive Test.*, 1975, doi: 10.1016/0029-1021(75)90023-7.

[39] H. J. Shin, J. Y. Park, S. C. Hong, and J. R. Lee, "In situ non-destructive evaluation of an aircraft UHF antenna radome based on pulse-echo ultrasonic propagation imaging," *Compos. Struct.*, vol. 160, pp. 16–22, 2017, doi: 10.1016/j.compstruct.2016.10.058.

[40] R. J. Ditchburn, S. K. Burke, and C. M. Scala, "NDT of welds : state of the art," vol. 29, no. 2, pp. 111–117, 1996.

[41] P. Cawley and D. Alleyne, "The use of Lamb waves for the long range inspection of large structures," vol. 34, pp. 287–290, 1996.

[42] A. Katunin, "Diagnostics of composite structures using wavelets," no. May, 2015.

[43] H. Schomberg, W. Beil, G. C. McKinnon, R. Proksa, and O. Tschendel, "Ultrasound Computerized Tomography.," *Acta Electron. Paris*, vol. 26, no. 1–2, pp. 121–128, 1984.

[44] C. Cunliffe, A. Joshi, Y. Mehta, and D. Cleary, "A study to determine the impact of cracking on load transfer efficiency of rigid airfield pavements," *J. Test. Eval.*, 2014, doi: 10.1520/JTE20130042.

[45] S. H. Kee, T. Oh, J. S. Popovics, R. W. Arndt, and J. Zhu, "Nondestructive bridge deck testing with air-coupled impact-echo and infrared thermography," *J. Bridg. Eng.*, 2012, doi: 10.1061/(ASCE)BE.1943-5592.0000350.

[46] M. T. A. Chaudhary, "Effectiveness of Impact Echo testing in detecting flaws in prestressed concrete slabs," *Constr. Build. Mater.*, 2013, doi: 10.1016/j.conbuildmat.2013.05.021.

[47] K. Il Song and G. C. Cho, "Numerical study on the evaluation of tunnel shotcrete using the Impact-Echo method coupled with Fourier transform and short-time Fourier transform," *Int. J. Rock Mech. Min. Sci.*, 2010, doi: 10.1016/j.ijrmms.2010.09.005.

[48] J. Martin, M. S. A. Hardy, A. S. Usmani, and M. C. Forde, "Accuracy of NDE in bridge assessment," vol. 20, no. 11, pp. 979–984, 1998.

[49] B. Raj, T. Jaykumar, and M. Thavasiumuthu, "Practical non-destructive testing - Ultrasonic testing," in *Practical non-destructive testing*, 2002.

[50] N. McCormick and J. Lord, "Digital image correlation," *Mater. Today*, vol. 13, no. 12, pp. 52–54, 2010, doi: 10.1016/S1369-7021(10)70235-2.

[51] R. S. Piascik and S. a. Willard, "The Characteristics of Fatigue Damage in the Fuselage Riveted Lap Splice Joint," no. November 1997, 1997.

[52] L. Topolář, L. Pazdera, B. Kucharczyková, J. Smutnỳ, and K. Mikulášek, "Using acoustic emission methods to monitor cement composites during setting and hardening," *Appl. Sci.*, vol. 7, no. 5, 2017, doi: 10.3390/app7050451.

[53] L. Alfayez, D. Mba, and G. Dyson, "The application of acoustic emission for detecting incipient cavitation and the best efficiency point of a 60 kW centrifugal pump: Case study," *NDT E Int.*, 2005, doi: 10.1016/j.ndteint.2004.10.002.

[54] K. Yoneda and J. Ye, "Crack propagation and acoustic emission behavior of silver-added Dy123 bulk superconductor," *Phys. C Supercond. its Appl.*, 2006, doi: 10.1016/j.physc.2006.06.032.

[55] I. Silversides, A. Maslouhi, and G. LaPlante, "Acoustic emission monitoring of interlaminar delamination onset in carbon fibre composites," *Struct. Heal. Monit.*, 2013, doi: 10.1177/1475921712469994.

[56] S. Shahidan, R. Pulin, N. Muhamad Bunnori, and K. M. Holford, "Damage classification in reinforced concrete beam by acoustic emission signal analysis," *Constr. Build. Mater.*, 2013, doi: 10.1016/j.conbuildmat.2013.03.095.

[57] T. Vetterlein and S. Georgi, "Application of Magnetic Particle Inspection in the Field of the Automotive Industry," pp. 1–11, 2006.

[58] E. Siores, A. S. Lamb, and L. M. Swallow, "Bacterial Magnetic Particles for Applications in NDT & E , Detection of Flaws and Cracks in Sample Materials," pp. 25–28, 2008.

[59] M. Carlstedt and B. Sciences, "Comparative Investigation on Lorentz Force Eddy Current Testing and Eddy Current Testing," no. September, pp. 3–8, 2013.

[60] P. Gao, C. Wang, Y. Li, and Z. Cong, "Electromagnetic and eddy current NDT in weld inspection: A review," *Insight Non-Destructive Test. Cond. Monit.*, 2015, doi: 10.1784/insi.2015.57.6.337.

[61] D. Vasić, V. Bilas, and D. Ambruš, "Pulsed eddy-current nondestructive testing of ferromagnetic tubes," *IEEE Trans. Instrum. Meas.*, 2004, doi: 10.1109/TIM.2004.830594.

[62] H. Shaikh *et al.*, "Use of eddy current testing method in detection and evaluation of sensitisation and intergranular corrosion in austenitic stainless steels," *Corros. Sci.*, 2006, doi: 10.1016/j.corsci.2005.05.017.

[63] A. Sophian, G. Y. Tian, and S. Zairi, "Pulsed magnetic flux leakage techniques for crack detection and characterisation," *Sensors Actuators, A Phys.*, 2006, doi: 10.1016/j.sna.2005.07.013.

[64] G. Katragadda, W. Lord, Y. S. Sun, S. Udpa, and L. Udpa, "Alternative magnetic flux leakage modalities for pipeline inspection," *IEEE Trans. Magn.*, 1996, doi: 10.1109/20.497554.

[65] D. Francis, R. P. Tatam, and R. M. Groves, "Shearography technology and applications: A review," *Meas. Sci. Technol.*, vol. 21, no. 10, 2010, doi: 10.1088/0957-0233/21/10/102001.

[66] R. Pezzoni and R. Krupka, "Laser-shearography for non-destructive testing of large-area composite helicopter structures," *Insight Non-Destructive Test. Cond. Monit.*, 2001.

[67] J. W. Newman and J. Lindberg, "Laser shearography of wind turbine blades," *Mater. Eval.*, 2010.

[68] H. Liu *et al.*, "Shearography using wave-defect interactions for crack detection in metallic structures," in *IEEE International Ultrasonics Symposium, IUS*, 2017, doi: 10.1109/ULTSYM.2017.8092815.

[69] F. Zastavnik, L. Pyl, J. Gu, H. Sol, M. Kersemans, and W. Van Paepegem, "Comparison of shearography to scanning laser vibrometry as methods for local stiffness identification of beams," *Strain*, 2014, doi: 10.1111/str.12069.

[70] A. R. Ganesan, "on Non-Destructive Evaluation Holographic and Laser Speckle Methods in Non-Destructive Testing," pp. 126–130, 2009.

[71] Q. Zhao, X. Dan, F. Sun, Y. Wang, S. Wu, and L. Yang, "applied sciences Digital Shearography for NDT : Phase Measurement Technique and Recent Developments," doi: 10.3390/app8122662.

[72] T. Giesko, A. Zbrowski, and P. Czajka, "LASER PROFILOMETERS FOR SURFACE INSPECTION," pp. 97–108, 2007.

[73] P. J. Diaci, "Laser Profilometry for the Characterization of Craters Produced in Hard Dental Tissues by Er : YAG and Er , Cr : YSGG Lasers," vol. 2008, no. 2, pp. 1–10, 2008.

[74] D. Grigg, E. Felkel, J. Roth, X. Colonna de Lega, L. Deck, and P. J. de Groot, "Static and dynamic characterization of MEMS and MOEMS devices using optical interference microscopy," in *MEMS, MOEMS, and Micromachining*, 2004, doi: 10.1117/12.546211.

[75] A. Garbacz, L. Courard, and K. Kostana, "Characterization of concrete surface roughness and its relation to adhesion in repair systems," *Mater. Charact.*, 2006, doi: 10.1016/j.matchar.2005.10.014.

[76] J. L. DAVIS and A. P. ANNAN, "GROUND-PENETRATING RADAR FOR HIGH-RESOLUTION MAPPING OF SOIL AND ROCK STRATIGRAPHY," *Geophys. Prospect.*, 1989, doi: 10.1111/j.1365-2478.1989.tb02221.x.

[77] J. A. Huisman, S. S. Hubbard, J. D. Redman, and A. P. Annan, "Measuring Soil Water Content with Ground Penetrating Radar: A Review," *Vadose Zo. J.*, 2003, doi: 10.2136/vzj2003.4760.

[78] R. J. Yelfm, "Application of Ground Penetrating Radar to Civil and Geotechnical Engineering," *V.7, №1 (18), 2007*, 2007.

[79] J. J. Daniels, "Ground Penetrating Radar Fundamentals," *USEPA Publ.*, 2000.

[80] L. B. Conyers, *Ground-penetrating Radar for Geoarchaeology*. 2016.

[81] J. A. Huisman, S. S. Hubbard, J. D. Redman, and A. P. Annan, "Measuring Soil Water Content with Ground

Penetrating Radar: A Review," *Vadose Zo. J.*, 2003, doi: 10.2113/2.4.476.

[82] O. Hunaidi and P. Giamou, "Ground-penetrating radar for detection of leaks in buried plastic water distribution pipes," *Proc. 7th Int. Conf. Gr. Penetrating Radar*, 1998.

[83] C. Maierhofer, "Nondestructive evaluation of concrete infrastructure with ground penetrating radar," *J. Mater. Civ. Eng.*, 2003, doi: 10.1061/(ASCE)0899-1561(2003)15:3(287).

[84] J. R. Jensen, *Remote sensing of the environment: an earth resource perspective second edition*. 2014.

[85] D. Xu, Y. Wang, B. Xiong, and T. Li, "MEMS-based thermoelectric infrared sensors: A review," *Front. Mech. Eng.*, vol. 12, no. 4, pp. 557–566, 2017, doi: 10.1007/s11465-017-0441-2.

[86] T. D. Dao *et al.*, "MEMS-based wavelength-selective bolometers," *Micromachines*, vol. 10, no. 6, pp. 1–12, 2019, doi: 10.3390/mi10060416.

[87] S. Verspeek, J. Peeters, B. Ribbens, and G. Steenackers, "Excitation Source Optimisation for Active Thermography," *Proceedings*, vol. 2, no. 8, p. 439, 2018, doi: 10.3390/icem18-05325.

[88] S. Bagavathiappan, B. B. Lahiri, T. Saravanan, J. Philip, and T. Jayakumar, "Infrared thermography for condition monitoring - A review," *Infrared Physics and Technology*. 2013, doi: 10.1016/j.infrared.2013.03.006.

[89] A. Di Carlo, "Thermography and the possibilities for its applications in clinical and experimental dermatology," *Clin. Dermatol.*, 1995, doi: 10.1016/0738-081X(95)00073-O.

[90] R. Vadivambal and D. S. Jayas, "Applications of Thermal Imaging in Agriculture and Food Industry-A Review," *Food and Bioprocess Technology*. 2011, doi: 10.1007/s11947-010-0333-5.

[91] Y. C. Chou and L. Yao, "Automatic diagnosis system of electrical equipment using infrared thermography," in *SoCPaR 2009 - Soft Computing and Pattern Recognition*, 2009, doi: 10.1109/SoCPaR.2009.41.

[92] C. A. Balaras and A. A. Argiriou, "Infrared thermography for building diagnostics," *Energy Build.*, vol. 34, no. 2, pp. 171–183, 2002, doi: 10.1016/S0378-7788(01)00105-0.

[93] A. Kylili, P. A. Fokaides, P. Christou, and S. A. Kalogirou, "Infrared thermography (IRT) applications for building diagnostics: A review," *Applied Energy*. 2014, doi: 10.1016/j.apenergy.2014.08.005.

[94] M. Clark, M. Gordon, and M. C. Forde, "Issues over high-speed non-invasive monitoring of railway trackbed," in *NDT and E International*, 2004, doi: 10.1016/j.ndteint.2003.05.002.

[95] T. Omar and M. L. Nehdi, "Automation in Construction Remote sensing of concrete bridge decks using unmanned aerial vehicle infrared thermography," *Autom. Constr.*, vol. 83, no. February, pp. 360–371, 2017, doi: 10.1016/j.autcon.2017.06.024.

[96] A. Ellenberg, A. Kontsos, F. Moon, and I. Bartoli, "Bridge deck delamination identification from unmanned aerial vehicle infrared imagery," *Autom. Constr.*, 2016, doi: 10.1016/j.autcon.2016.08.024.

[97] I. Colomina, M. Blázquez, P. Molina, M. E. Parés, and M. Wis, "Towards a new paradigm for high-resolution low-cost photogrammetryand remote sensing," in *International Archives of the Photogrammetry, Remote Sensing and Spatial Information Sciences - ISPRS Archives*, 2008.

[98] H. Eisenbeiss, "The autonomous mini helicopter: a powerful platform for mobile mapping," *Int. Arch. Photogramm. Remote Sens. Spat. Inf. Sci.*, 2008.

[99] F. Remondino, L. Barazzetti, F. Nex, M. Scaioni, and D. Sarazzi, "UAV PHOTOGRAMMETRY FOR MAPPING AND 3D MODELING – CURRENT STATUS AND FUTURE PERSPECTIVES," *ISPRS - Int. Arch. Photogramm. Remote Sens. Spat. Inf. Sci.*, 2012, doi: 10.5194/isprsarchives-xxxviii-1-c22-25-2011.

[100] Á. Restás, "The regulation Unmanned Aerial Vehicle of the Szendro Fire Department supporting fighting against forest fires," *For. Ecol. Manage.*, 2006, doi: 10.1016/j.foreco.2006.08.260.

[101] G. Grenzdörffer, A. Engel, and B. Teichert, "The photogrammetric potential of low-cost UAVs in forestry and agriculture," *Int. Arch. Photogramm. Remote Sens. Spat. Inf. Sci.*, 2008.

[102] L. Design *et al.*, "Unmanned aerial vehicle inspection of the Placer River Trail Bridge through image-based 3D modelling Unmanned aerial vehicle inspection of the Placer River Trail Bridge through image-," *Struct. Infrastruct. Eng.*, vol. 2479, no. June, pp. 1–13, 2017, doi: 10.1080/15732479.2017.1330891.

[103] A. Khaloo, D. Lattanzi, A. Jachimowicz, and C. Devaney, "Utilizing UAV and 3D computer vision for visual inspection of a large gravity dam," *Front. Built Environ.*, vol. 4, no. July, pp. 1–16, 2018, doi: 10.3389/fbuil.2018.00031.

[104] R. . Haarbrink and E. Koers, "Helicopter UAV For Photogrammetry And Rapid Response," *Int. Achives Photogramm. Remote Sens. Spat. Inf. Sci. Belgium. Vol XXXVI-I/W44*, 2006.

[105] A. Puri, K. P. Valavanis, and M. Kontitsis, "Statistical profile generation for traffic monitoring using real-time UAV based video data," in *2007 Mediterranean Conference on Control and Automation, MED*, 2007, doi: 10.1109/MED.2007.4433658.

[106] S. Vii, "Photogrammetric Surveys," pp. 1–28.

[107] S. M. Seitz, B. Curless, J. Diebel, D. Scharstein, and R. Szeliski, "A comparison and evaluation of multi-view stereo reconstruction algorithms," in *Proceedings of the IEEE Computer Society Conference on Computer Vision and Pattern Recognition*, 2006, doi: 10.1109/CVPR.2006.19.

[108] H. Hirschmüller, "Stereo processing by semiglobal matching and mutual information," *IEEE Trans. Pattern Anal. Mach. Intell.*, 2008, doi: 10.1109/TPAMI.2007.1166.

[109] B. Triggs *et al.*, *Bundle Adjustment – A Modern Synthesis To cite this version : HAL Id : inria-00548290 Bundle Adjustment — A Modern Synthesis*. 2010.

[110] M. J. Westoby, J. Brasington, N. F. Glasser, M. J. Hambrey, and J. M. Reynolds, "'Structure-from-Motion' photogrammetry: A low-cost, effective tool for geoscience applications," *Geomorphology*, vol. 179, pp. 300–314, 2012, doi: 10.1016/j.geomorph.2012.08.021.

[111] J. Chris McGlone, "Manual of photogrammetry," *Photogrammetric Engineering and Remote Sensing*. 2013, doi: 10.1111/j.1477-9730.2005.00343_1.x.

[112] N. Kochi, "Photogrammetry," in *Handbook of Optical Metrology: Principles and Applications, Second Edition*, 2015.

[113] M. Brown and D. Lowe, "Invariant Features from Interest Point Groups."

[114] D. G. Lowe, "Distinctive Image Features from Scale-Invariant Keypoints," vol. 60, no. 2, pp. 91–110, 2004.

[115] J. Canny, "A Computational Approach to Edge Detection," *IEEE Trans. Pattern Anal. Mach. Intell.*, 1986, doi: 10.1109/TPAMI.1986.4767851.

[116] L. Ding and A. Goshtasby, "On the Canny edge detector," vol. 34, no. January 2000, pp. 721–725, 2001.

[117] O. Özyeşil, V. Voroninski, R. Basri, and A. Singer, "A survey of structure from motion," *Acta Numer.*, vol. 26, pp. 305–364, 2017, doi: 10.1017/S096249291700006X.

[118] P. H. Nyimbili, H. Demirel, D. Z. Seker, and T. Erden, "Structure from Motion (SfM) - Approaches and Applications," no. September 2018, 2016.

[119] M. J. Westoby, J. Brasington, N. F. Glasser, M. J. Hambrey, and J. M. Reynolds, "Geomorphology ' Structure-from-Motion ' photogrammetry : A low-cost , effective tool for geoscience applications," *Geomorphology*, vol. 179, pp. 300–314, 2012, doi: 10.1016/j.geomorph.2012.08.021.

[120] D. Turner, A. Lucieer, and C. Watson, "Development of an unmanned aerial vehicle (UAV) for hyper resolution vineyard mapping based on visible, multispectral, and thermal imagery," *34th Int. Symp. Remote Sens. Environ. - GEOSS Era Towar. Oper. Environ. Monit.*, 2011.

[121] E. Ippoliti, A. Meschini, and F. Sicuranza, "Structure from motion systems for architectural heritage. A survey of the internal loggia courtyard of palazzo dei capitani, ascoli piceno, italy," *Int. Arch. Photogramm. Remote Sens.*

Spat. Inf. Sci. - ISPRS Arch., vol. 40, no. 5W4, pp. 53–60, 2015, doi: 10.5194/isprsarchives-XL-5-W4-53-2015.

[122] A. Sabato and C. Niezrecki, "Evaluation of using structure from motion optical techniques for structural health monitoring of railroad track," in *Structural Health Monitoring 2017: Real-Time Material State Awareness and Data-Driven Safety Assurance - Proceedings of the 11th International Workshop on Structural Health Monitoring, IWSHM 2017*, 2017, doi: 10.12783/shm2017/14228.

[123] G. Morgenthal *et al.*, "Framework for automated UAS-based structural condition assessment of bridges," *Autom. Constr.*, vol. 97, no. October 2018, pp. 77–95, 2019, doi: 10.1016/j.autcon.2018.10.006.

[124] L. Inzerillo, G. Di Mino, and R. Roberts, "Image-based 3D reconstruction using traditional and UAV datasets for analysis of road pavement distress," *Autom. Constr.*, 2018, doi: 10.1016/j.autcon.2018.10.010.

[125] R. Szeliski, "Computer Vision : Algorithms and Applications," 2010.

[126] FLIR, "FLIR ONE® Pro-Series PRO AND PRO LT MODELS."

[127] V. Matrice and Q. S. Guide, "Matrice 200 v2."

[128] DJI, "Zenmuse XT 2 - User manual V1.0," pp. 1–18, 2018.

[129] L. Ebx and E. Ebx, "FLIR Serie E bx."

[130] S. Hiasa, R. Birgul, M. Matsumoto, and F. Necati Catbas, "Experimental and numerical studies for suitable infrared thermography implementation on concrete bridge decks," *Meas. J. Int. Meas. Confed.*, 2018, doi: 10.1016/j.measurement.2018.02.019.

[131] X. Chen, P. J. Flynn, and K. W. Bowyer, "IR and visible light face recognition," *Comput. Vis. Image Underst.*, 2005, doi: 10.1016/j.cviu.2005.03.001.

[132] Z. Wenjing and W. Xueqiang, "Design of infrared small target detection software based on energy minimization constraints," in *Proceedings - 2014 5th International Conference on Intelligent Systems Design and Engineering Applications, ISDEA 2014*, 2014, doi: 10.1109/ISDEA.2014.88.

[133] Z. Tang and X. Wang, "An efficient algorithm for infrared small target detection," in *2009 2nd International Conference on Information and Computing Science, ICIC 2009*, 2009, doi: 10.1109/ICIC.2009.121.

[134] W. Ting and S. Yang, "Weak and small infrared target automatic detection based on wavelet transform," in *Proceedings - 2008 2nd International Symposium on Intelligent Information Technology Application, IITA 2008*, 2008, doi: 10.1109/IITA.2008.537.

[135] N. Sang and T. Zhang, "Segmentation of FLIR images by Hopfield neural network with edge constraint," *Pattern Recognit.*, 2001, doi: 10.1016/S0031-3203(00)00041-8.

[136] S. Teng, G. Chen, G. Liu, and J. Lv, "applied sciences Modal Strain Energy-Based Structural Damage Detection Using Convolutional Neural Networks," 2019.

[137] R. Heriansyah and S. A. R. Abu Bakar, "Defect Detection in Thermal Image using Thresholding Technique," *6th WSEAS Int. Conf. CIRCUITS, Syst. Electron. SIGNAL Process.*, no. January 2007, pp. 341–346, 2007.

[138] N. Otsu, "THRESHOLD SELECTION METHOD FROM GRAY-LEVEL HISTOGRAMS.," *IEEE Trans Syst Man Cybern*, 1979, doi: 10.1109/tsmc.1979.4310076.